ABSTRACT

Manipulation of single cells and particles is important to biology and nanotechnology. Our electrokinetic (EK) tweezers manipulate objects in simple microfluidic devices using gentle fluid and electric forces under vision-based feedback control. In this dissertation, I detail a user-friendly implementation of EK tweezers that allows users to select, position, and assemble cells and nanoparticles. This EK system was used to measure attachment forces between living breast cancer cells, trap single quantum dots with 45 nm accuracy, build nanophotonic circuits, and scan optical properties of nanowires. With a novel multi-layer microfluidic device, EK was also used to guide single microspheres along complex 3D trajectories. The schemes, software, and methods developed here can be used in many settings to precisely manipulate most visible objects, assemble objects into useful structures, and improve the function of lab-on-a-chip microfluidic systems.

Image-Guided Precision Manipulation of Cells and Nanoparticles in Microfluidics

By

Zachary Cummins

Dissertation submitted to the Faculty of the Graduate School of the
University of Maryland, College Park, in partial fulfillment
of the requirements for the degree of
Doctor of Philosophy
2016

Advisory Committee:
Professor Benjamin Shapiro, Chair
Associate Professor Yu Chen
Associate Professor Stuart Martin
Associate Professor Edo Waks
Associate Professor Ian White

Acknowledgements

This dissertation is a compilation of works in which many people had a hand. I am pleased to acknowledge... Benjamin Shapiro, my advisor, for countless opportunities, excellent advice, and much appreciated patience. Roland Probst, for laying the foundation of my graduate career, and for many discussions that shaped my approach to both work and life. Edo Waks, for his sharp advice and mastery of the science that led to the many important results discussed here. Chad Ropp, for his tireless effort in the lab and in writing. Stuart Martin, for inviting me and Roland into his lab and sharing so much of his own time and resources. Ian White and Yu Chen, for their excellent classes, and serving on my dissertation committee. My labmates, especially Bharath Ramaswamy, Alek Nacev, Azeem Sarwar, and Reza Basiri, for their time, enthusiasm, and input. You all made my time at the University of Maryland worthwhile.

Many others supported me away from work. I thank… My parents, Jean and Wally Cummins, and my sister, Laura Cummins, for all their love and support; none of this would be possible without my parents' planning and sacrifice. My friends, especially Robert Hellauer, Mark Finkelstein, Seth Napora, and Levi Devries, for much needed distraction and conversation. Thank you all for keeping me (kind of) sane over many years.

Finally, I dedicate this dissertation to Monica Cummins, my wonderful wife. She is brave and strong, and I would barely function without her love and understanding.

Table of Contents

Table of Contents

Table of Figures

Chapter 1

Introduction

1.1   Background

Precise manipulation of things at the nano and microscale is needed to advance important research areas like biology and nanotechnology. In biology, for example, direct manipulation of cells, DNA, and proteins can help to better understand complex cellular processes.[1] In nanotechnology, the ability to make and test structures at the nanoscale can help to make smaller, more powerful computers.[2]

Manipulation of single cells is needed to improve our understanding of complex biological processes. The ability to address and manipulate single cells is important for characterizing the heterogeneity of large populations of cells as well as focusing on their individual properties. Typically, *in vitro* biological studies are performed on large populations of cells of the same genotype. However, the stochastic nature of gene and protein expression leads to heterogeneity in these populations, and results in noisy data that does not accurately reflect all its members.[3] Other populations, as from blood, are known to be heterogeneous, but are difficult to sort through to identify markers of disease.[4–6] To fully characterize these populations, each cell must be addressed and processed with high precision.

Precise manipulation of single nanoparticles is essential for developing smaller, faster computers that use light instead of electricity. Light is an ideal candidate to replace electricity because it offers more bandwidth[7] than electronics while requiring less power.[8]

1

Introduction

As a natural distributor of quantum of information, light can be used for secure communications[9] and fast information processing.[10] Computing logic is implemented with optical switches that employ quantum mechanics[11] and plasmon resonance[12] to allow efficient interaction between light and matter at the nanoscale. To build the next generation of computer, circuits of optical switches must be assembled and tested with tools that select and position nanoparticles with nanometer precision.

Microfluidic devices make it possible to address and manipulate single nano and microscopic objects.[13,14] Microfluidic devices are made up of networks of channels with dimensions as small as 1 µm that handle small volumes of fluid appropriate for addressing single cells (1-100 µm) and nanoparticles (1-100 nm).[15] The physics of fluids in a microfluidic channel are simpler than at larger scales and can be exploited to miniaturize sample preparation steps. Integrating multiple sample preparation steps with microelectromechanical and optical elements forms robust "lab on a chip" systems that replace whole laboratory procedures. Microfluidic devices have been used in biology, for example, to mimic whole organs, detect disease, and filter biomolecules and cells out of unpurified samples.[16–20] Other systems carefully synthesize nanoparticles, test their biocompatibility against cells, or employ them for their electronic and optical properties.[21,22] However, microfluidic systems like these typically handle many objects as they pass through, or passively filter them for later analysis. Additional methods are needed to deterministically select and position single objects.

1.2   Methods that manipulate nano and microscopic objects

Many methods manipulate single nano and microscopic objects, but they all have drawbacks to consider when choosing the right one for an application. The following briefly summarizes the physics, applications, and disadvantages of methods that use mechanical, optical, electrical, magnetic, acoustic, and fluid forces.

Direct tactile contact is reliable method for directly handling objects at the nano and microscale. Tactile manipulators pick and place microscopic objects like cells with great accuracy or can transfer them between vessels for parallel assays and cataloging.[23,24] Objects are grabbed by a small gripper or pipette and moved by hand or a motorized translation stage. Micromanipulators have been used extensively to automate single cell analysis for fertility, genomics, and proteomics.[24–26] Nanoscopic objects can be manipulated with sophisticated systems that use piezoelectric cantilevers integrated with scanning probe or scanning electron microscopes. Due to their cost, size, and complexity, these nanomanipulators are primarily used for imaging nanoscale features and characterizing nanoscale forces, such as the material properties of carbon nanotubes.[27,28]

Laser tweezers manipulate objects that scatter light and are the gold standard for non-tactile manipulation of single microscopic objects.[29–35] Standard laser tweezer systems trap objects near the focal point of a tightly focused laser beam. When an object with an index of refraction less than the surrounding fluid moves away from the focal point, it refracts light away from the center of the beam, causing a change in momentum that is balanced by pushing the object back to the focal point.[29,31] Laser traps can be moved relative to a container by directing the laser beam using actuated optics, or by

moving the container itself. Holographic laser tweezers can trap as many as 400 objects at the same time in three dimensions by quickly moving the one laser beam between different points or using many beams in parallel.[36–39]

Laser tweezers have several drawbacks. While impressive in terms of accuracy and throughput, laser tweezers are sophisticated desktop systems that require significant investment of lab space and funds, and have important limitations when working with nanoparticles and biological samples. Entry level systems that only create one trap cost ~US\$15,000,[40] and more sophisticated systems cost significantly more. Laser traps are less effective at trapping single nanoparticles than single microparticles, and are nonselective. Optical trapping forces scale with the volume of the object being controlled $(\sim r^3)$[29,32,33,36,41] and can be easily overcome by Brownian motion, which scale inversely with radius $(\sim r)$,[42,43] and fluid disturbances, which scale with radius.[44,45,42] Stable traps attract all objects in the vicinity, so objects must be sufficiently dilute to only trap one. Biological samples must also be purified to work with the precisely calibrated optics of laser tweezers, and prolonged exposure to lasers can lead to photodamage in cells.[46–48]

Several systems use dielectrophoresis to manipulate objects. Dielectrophoresis (DEP) occurs when a non-uniform electric field is applied to a medium.[49–53] Objects in the medium polarize and move to or away from regions of high electric field strength, depending on how the objects polarize relative to the medium and the frequency of the electric field. Typically, objects are trapped or deflected by stationary electrodes patterned onto a surface,[54–58] but can be also be precisely positioned by moving the electrodes or altering the electric field using vision-based feedback control similar to the work discussed here.[59–61] Optoelectronic tweezers create thousands of movable DEP traps

that by projecting light onto a photoconductive surface with a video projector.[62–64] Like laser tweezers, DEP forces are nonselective and are ineffective on nanoparticles because they scale with the volume of the object. Precise DEP manipulation has so far been limited to two dimensions.

Acoustic tweezers trap objects using ultrasound waves.[65,66] In many acoustic trapping systems, piezoelectric transducers send standing ultrasound waves into a microfluidic device. Object in the device scatter the waves and are pushed to either a node or anti-node of the standing wave, depending on the density and deformability of the objects relative to the fluid.[67–70] An object trapped in a node can be positioned by changing the phase of the wave.[66,71–74] Like with laser tweezers and DEP, acoustic forces are nonselective and scale with the volume of the object being controlled. While acoustic tweezers create many traps at the same time, the traps are arranged according to the period of the sound wave and are not necessarily independent. Acoustic tweezers have also been limited to two dimensions so far.

Magnetic objects can be controlled using magnetic forces.[75–82] In many cases, magnetic objects are controlled using large, powerful electromagnets placed away from the trapping location. To trap objects at a point in the trapping region, they must be repeatedly pulled from where they are to the trapping location by changing the magnetic field. Feedback control algorithms for this have been developed in theory[83–87] and demonstrated in experiments.[75,78,83,88] Magnetic forces also scale with the radius of the particle, making control of nanoparticles difficult, and rapidly decrease with distance away from the magnet,[89,90] so only powerful electromagnets produce useful fields in the trapping location. Other methods directly integrate magnets into microfluidic chips using

microelectronics manufacturing methods to overcome these scaling difficulties.[79,91] In any case, magnetic tweezers can only control magnetic objects, so non-magnetic objects such as biological cells must be attached to magnetic objects using antibodies or other bonding agents.[79,81,82,91]

Electrically charged objects can be controlled using electrostatic forces. Under electrophoresis (EP), charged objects move toward regions of opposite charge when an electric field is applied. Since many biological objects carry an inherent charge, EP is frequently used in laboratories to separate cells and DNA, and its biological effects are well understood.[92] EP is easily generated in microfluidic devices using wires or patterned electrodes, and has been used to separate, deflect, and trap objects.[93] With feedback control, EP has also been used to precisely manipulate and suppress the Brownian motion of single molecules.[94–96] The force of EP on an object is influenced by charges that form at its surface, so EP generally scales with surface area rather than volume.[97] Electric fields used for EP manipulation are typically much lower than those used to lyse cells (> 100 V/cm for red blood cells[98]), but prolonged application of even low electric potential leads to electrolysis and electrochemical changes that fowl microfluidic devices.[99] Electrochemical affects can be mitigated by using non-reactive platinum electrodes and salt bridges.[100]

Hydrodynamic forces are better able to manipulate nanoparticles than optical, DEP, acoustic, and magnetic forces. Fluid flow is integral to the function of microfluidic devices and can be manipulated using syringe pumps, peristaltic pumps, air pressure, and many other methods. Drag forces scale only with the radius of an object, rather than volume, and do not depend on the material properties of the object, making them an

excellent choice to manipulate nanoparticles. Microfluidic devices designed to exploit hydrodynamic forces can separate, focus, and trap objects such as chemical analytes and cells.[101] Nanoparticles have also been precisely positioned in 2D by controlling pressure in a microfluidic device using valves and feedback control.[102–104] Fluid flow driven by pumps and air pressure enables steady high-throughput chemical analysis, but requires sophisticated valves and sensors for high resolution control.

Electroosmosis generates hydrodynamic forces using electric fields.[14,105–107] When water fills a microfluidic device made of glass and/or PDMS, silanol groups at the walls of the device dissociate, losing one hydrogen ion and exposing a stationary negative charge.[108] Positively charged ions in the fluid gather in a cloud at the newly charged surface. When an electric field is applied, the cloud moves under electrophoresis and drags the rest of the fluid in the device with it. The motion of the fluid at the walls of the device causes the resulting electroosmotic (EO) flow to be essentially uniform, rather than parabolic as for flows induced with external pressure. EO is easily generated using wires or patterned electrodes, and is routinely used for pumping fluid and sorting objects.[109,110]

1.3 Electrokinetic tweezing

Together, electrophoresis and electroosmosis create electrokinetic forces at low voltages that are ideal for manipulating single cells and nanoparticles, but do not naturally trap them. EP and EO are easily applied in a microfluidic device using relatively inexpensive voltage output devices or microcontrollers. Cells in the electric field are safe as long as electric fields are kept low.[98] While optical, DEP, acoustic, and

magnetic forces all scale with the volume of an object,[31,64,70,111] the electrostatic forces EP creates scale with surface area and the hydrodynamic forces EO creates scale only with radius, making them better for manipulating nanoparticles.[44,45,42] However, EP and EO cannot create movable, stable traps without additional control.

Fig. 1 Schematic of vision-based electrokinetic feedback control in two dimensions. The system is shown manipulating a neutral particle with electroosmotic (EO) flow only. A microfluidic device, control algorithm, and particle tracking system are connected in a real-time feedback loop. The vision tracking system measures the position of a particle chosen by a user. The control algorithm then calculates which EO fluid flow will carry this particle from its current towards its desired position, and electrodes then actuate the necessary fluid flow. This feedback loop repeats continually and at each time moves the chosen particle closer to its desired position, thus either trapping it in place or steering it along any desired trajectory.

Our research group developed a vision-based feedback control system that traps and moves objects in simple microfluidic devices using electrokinetic forces. As shown in Fig. 1, objects suspended in a fluid are entered into a microfluidic device. Their positions are tracked using microscope optics and image processing. One or more objects are selected by a user and moved to a desired location by calculating and applying an electric field that will push them in the right direction. This process is repeated to account for uncertainties in the model and the device, and quickly pushes objects to their desired locations.

1.4 Outline for the rest of this dissertation

The rest of this dissertation discusses the theory and implementation of EK tweezers for biology and nanotechnology. Chapter 2 details the EK physics and control algorithm that manipulate objects. Chapter 3 outlines an implementation of EK tweezers that uses commonplace research equipment and software, and demonstrates the use of this system in manipulating microbes, measuring attachment forces between cancer cells, and positioning and immobilizing nanoscopic quantum dots. In Chapter 4, metallic nanowires are assembled into nanostructures with several important modifications to this implementation which account for non-spherical objects. In Chapter 5, spatial optical properties of metallic nanowires are imaged with nanometer resolution by automatically scanning quantum dot probes in their vicinity. In Chapter 6, EK tweezing is extended into three spatial dimensions with a 3D microfluidic device and 3D imaging. Chapter 7 summarizes the developments presented in this dissertation, discusses their importance, and proposes future research opportunities. Finally, the intellectual contributions of the author are outlined relative to the group of collaborators.

Chapter 2

Principles of Electrokinetic Tweezing

2.1   Vision-based feedback control

Electrokinetic tweezers move objects by a vision-based feedback control loop made up of a microfluidic control device, a control algorithm, and an object tracking system. Before control, a user or program chooses the object to be controlled and where the object should move to. At each time step during control, the object is found by the object tracking system and pushed toward its desired position by calculating and applying the electric field that will create the needed electrokinetic forces. Each time the loop repeats, the chosen object is pushed closer to its desired position, trapping it in one position or dragging it along a complex trajectory.[112–116] EK tweezers are robust to imperfections in the microfluidic device and modelling, allowing the object to quickly reach its target as long as the control algorithm knows how to move it closer. Optimized EK tweezers manipulate objects with nanoscale accuracy.[115,117]

When an electric field is created in the control device, objects move due to electrophoresis and electroosmosis. The electric field in the microfluidic device is created by a voltage generator. In electrophoresis, a small charged particle is attracted to a region of opposite charge and quickly reaches a steady-state velocity in line with the applied electric field.[118–120] In electroosmosis, the movement of many charged particles at the walls of a fluid channel causes all the fluid in the device to move.[44] When an electrolyte solution is introduced into a channel made of glass or plastic, the walls of the channel

become negatively charged and attract a ~10 nm thick cloud of positively charged particles. When this cloud is pulled by electrophoresis it drags along the rest of the fluid and anything in it. The amount an object is moved by these forces depends on the strength of its own charge and the strength of the charge of the cloud at the walls.

Objects are controlled by creating EK forces that push them toward their desired positions. The microfluidic device must be able to create the needed EK forces. First, consider control in one dimension. An object is floating in a straight microchannel that has an electrode at each end. A voltage applied between the two electrodes moves the object to the right. When the voltage is reversed, the object moves to the left. If the object is to the left of its desired point, voltage is applied to push it to the right. Voltage is stopped as soon as the object reaches it. If the object passes the desired position, the voltage is reversed and the process is repeated. Naively, an object could be controlled in two dimensions at the intersection of two straight microchannels: one each to control the x and y axes. However, these two microchannels are not insulated from each other, and the electric field is more complex. A more complete understanding of the EK physics in a microfluidic device is required to control objects in two and three dimensions.

2.2   Physics

The total EK velocity of an object is the sum of its EP and EO velocities, *i.e.* $\vec{v}_{EK} = \vec{v}_{EP} + \vec{v}_{EO}$. The EP velocity $\vec{v}_{EP}$ is the steady-state velocity of a charged object in a still fluid when an electric field is applied. The EO velocity $\vec{v}_{EO}$ is the steady-state velocity of a neutral object in the flow caused by an electric field. In each case the object reaches a steady-state velocity quickly relative to the period of control.

EP velocity $\vec{v}_{EP}$ for an object in a liquid is given by the Helmholtz-Smoluchowski relation,[44]

$$\vec{v}_{EP} = \frac{\varepsilon_r \varepsilon_0 \zeta_p}{\eta} \vec{E} = \mu_{EP} \vec{E}, \tag{1}$$

where ζ_p is the electrokinetic "zeta" potential of the object, η is the dynamic viscosity of the liquid, ε_0 is the dielectric constant of vacuum, and ε_r is the relative dielectric constant of the liquid. The properties of the object and liquid are encapsulated by the electrophoretic mobility μ_{EP}, which can be measured directly by applying a known electric field $\vec{E}$ and observing the velocity of the object. The electric field is given by Laplace's equation $\vec{E} = -\nabla\Phi$ with boundary conditions that reflect the electric potentials applied to the channel-end electrodes.

EO velocity $\vec{v}_{EO}$ of an object in an electrolyte solution is the same as the EO velocity of the fluid. The flow everywhere in a microfluidic device is accurately described by the Stokes equations

$$\nabla \cdot \vec{v}_{EO} = 0$$
$$\eta \nabla^2 \vec{v}_{EO} = \nabla p \tag{2}$$

for mass (top) and momentum (bottom), where p is the pressure of the fluid.[44] The boundary condition for equation 2 is the velocity of the cloud at the walls

$$\vec{v}_{EO}\big|_w = \mu_w \vec{E}\big|_w = \frac{\varepsilon_r \varepsilon_0 \zeta_w}{4\pi\eta}\,\vec{E}\big|_w, \tag{3}$$

where the cloud at the wall has an electrophoretic mobility μ_w and a zeta potential ζ_w. In many cases, the flow everywhere in the device is well aligned with the electric field, and it is convenient to use the simpler approximation

$$\vec{v}_{EO} = \mu_{EO}\vec{E}, \tag{4}$$

where μ_{EO} is the electroosmotic mobility of the fluid in the device. Under this simple approximation, the EK velocity of an object in the device is given by

$$\begin{aligned}
\vec{v}_{EK} &= \mu_{EP}\vec{E} + \mu_{EO}\vec{E} \\
&= \mu_{EK}\vec{E},
\end{aligned} \tag{5}$$

where $\mu_{EK} = \mu_{EP} + \mu_{EO}$ is the electrokinetic mobility of an object in a fluid in that device.

2.3 Control

An object is positioned by repeatedly changing its EK velocity to point from where it is to where it should be. For simplicity, this velocity is set by proportional control

$$\vec{v}_{EK} = k(\vec{x}_d - \vec{x}), \tag{6}$$

where $\vec{x}$ is the current position of the object, $\vec{x}_d$ is the desired position, and k is a multiplier used to tune control performance. Integral and derivative terms may be added to account for steady-state error and slow response.

The voltage needed to create the control velocity is found by inverting the model of electrokinetic physics. The Laplace and Stokes equations are both linear (*i.e.* $f(ax + by) = af(x) + bf(y)$) with respect to voltage. By treating the set of m electrode potentials as a vector $\vec{V} = [V_1 \quad V_2 \quad \cdots \quad V_m]^T$, it can be written as a sum of basis vectors $\vec{V} = V_1 \hat{e}_1 + V_2 \hat{e}_2 + \cdots + V_m \hat{e}_m$, where $\hat{e}_1 = [1 \quad 0 \quad \cdots \quad 0]^T$, $\hat{e}_2 = [0 \quad 1 \quad \cdots \quad 0]^T$, ..., $\hat{e}_m = [0 \quad 0 \quad \cdots \quad 1]^T$. Therefore $\vec{v}_{EK}$ can be decomposed into

$$\begin{aligned} \vec{v}_{EK}(\vec{V}) &= \vec{v}_{EK}(V_1 \hat{e}_1 + V_2 \hat{e}_2 + \cdots + V_m \hat{e}_m) \\ &= V_1 \vec{v}_{EK}(\hat{e}_1) + V_2 \vec{v}_{EK}(\hat{e}_2) + \cdots + V_m \vec{v}_{EK}(\hat{e}_m), \end{aligned} \tag{7}$$

which is a sum of m basis models each multiplied by the associated electrode potential. In matrix notation, equation 7 is rewritten as

$$\begin{aligned} \vec{v}_{EK} &= [\vec{v}_{EK}(\hat{e}_1) \quad \vec{v}_{EK}(\hat{e}_2) \quad \cdots \quad \vec{v}_{EK}(\hat{e}_m)][V_1 \quad V_2 \quad \cdots \quad V_m]^T \\ &= \mathbf{A}\vec{V} \end{aligned} \tag{8}$$

where the matrix $\mathbf{A}$ is a linear map between the voltage $\vec{V}$ being applied and the resulting electrokinetic velocity of an object $\vec{v}_{EK}$. Equation 8 is a standard linear system and $\vec{V}$ can be solved for in several ways. The voltage with the smallest magnitude is found by the method of least squares,

$$\vec{V} = (\mathbf{A}^T \mathbf{A})^{-1} \mathbf{A}^T \vec{v}_{EK}. \tag{9}$$

Substituting equation 6 for desired velocity into equation 9, the voltage that will push an object to its desired position is

$$\vec{V} = (\mathbf{A}^T \mathbf{A})^{-1} \mathbf{A}^T k (\vec{x}_d - \vec{x}). \tag{10}$$

Repeatedly solving equation 10 at a fast rate traps selected objects with high accuracy at stationary positions or steers them along complex trajectories.

Multiple objects can be controlled at the same time by simultaneously solving equation 8 for each. The linear system for n objects is

$$\begin{bmatrix} \vec{v}_{EK,1} \\ \vec{v}_{EK,2} \\ \vdots \\ \vec{v}_{EK,n} \end{bmatrix} = \begin{bmatrix} \mathbf{A}_1 \\ \mathbf{A}_2 \\ \vdots \\ \mathbf{A}_n \end{bmatrix} \vec{V}, \tag{11}$$

where $\vec{v}_{EK,i}$ is the electrokinetic velocity and $\mathbf{A}_i$ is the model matrix for object i. Equation 11 can be solved for by least squares as in equation 9. While an exact solution is possible as long as there are as many electrodes as components of velocity to control (*e.g.*

a device with eight electrodes could theoretically control four objects in two dimensions), the maximum voltage that can be applied limits the number of objects that can be controlled and how close together they can be.[118]
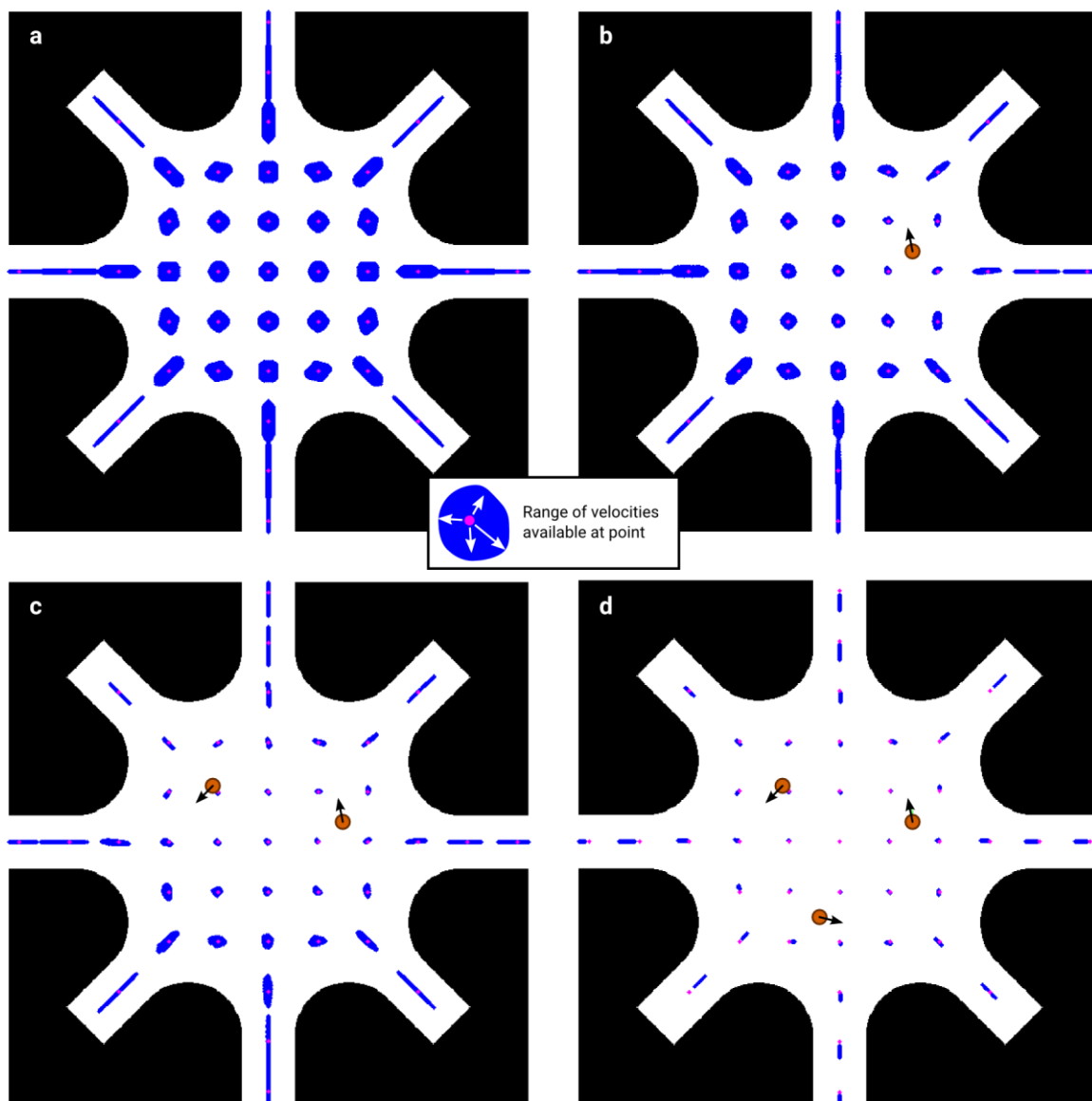
Fig. 2 Velocities available for control. As long as there are more electrodes than components of velocity to control, there are many possible solutions to the control problem. However, some solutions require high voltages that are impossible to create in practice. Here are shown the velocities it is possible to create to control the 1st, 2nd, 3rd, and 4th object (a, b, c, and d). Around each grid point (magenta), a region (blue) is drawn in which it is possible to achieve the control velocity for each additional object. **a)** The first object can be easily controlled in any direction anywhere in the control region. **b-c)** As the number of controlled objects increases, the range of velocities available for the next one decreases, especially in the vicinity of the objects. **d)** Control of 3 objects consumes most of the available velocity, despite there being two more electrodes than components of velocity to control.

Fig. 2 illustrates how control effort is consumed as an increasing number of objects are controlled at once in a microfluidic control device with four intersecting channels. Each pane simulates what velocities are available to control the 1st, 2nd, 3rd, and 4th object. In each scenario, there is a set of voltages that will achieve the desired control velocity, of which equation 10 is a member. The velocity field that each possible voltage will produce is illustrated for several grid points. Around each grid point (magenta) a region (blue) is drawn that bounds all the velocity vectors it is possible to control for each additional object. Controlling a new object shrinks the range of available velocities, especially in the vicinity of the object. The object selected first can be moved with adequate velocity anywhere in the control area (Fig. 2(a)). Once controlled, the bounding regions near the first object shrink (Fig. 2(b)), showing how difficult it is to control two objects in the same vicinity. Subsequent objects (Fig. 2(c and d)) limit the available velocities even further until control of a fourth object is unlikely unless it is kept still (Fig. 2(d)). Controlling many objects in close proximity leads to voltages that are unstable or impossible to achieve in practice.

2.4   Summary

Electrokinetic tweezers move objects by feedback control in simple microfluidic devices actuated by electric fields. An electric field created in the device by electrodes gives rise to electrophoresis (EP) and electroosmosis (EO). Under EP, objects move with the electric field according to their charge. Under EO, a dense cloud of charged particles gathered at the surface of the microfluidic device moves under EP, dragging all the fluid and objects in the device with them. Based on this model of electrokinetic forces, the control algorithm calculates the electric field that will move objects from where they are

to where they should be. Multiple objects can be independently controlled as long as the electric field is created by more electrodes than there are components of velocity to control, and objects are kept far apart from each other. Repeating this control algorithm precisely traps objects or moves them along complex trajectories.

Chapter 3

Implementation of Electrokinetic Tweezing

3.1   Motivation

An effective implementation of electrokinetic tweezers should be adaptable to many applications and easy to use. In general, EK tweezers are made up of a microfluidic control device, a microscopic imaging system, and control software. While the objective is always to precisely move an object to a desired position, the control device and imaging system may need to be modified to accommodate the properties of the objects and fluids being controlled. As a result, the control software must be able to work with many different control models, imaging methods, video cameras, and voltage output devices. The software should also allow users to easily interact with objects in the control region and alter control parameters so that they are able to carry out and repeat experiments without intimate knowledge of the control system.

Our group's first electrokinetic tweezers system used a smart camera and desktop computer. Objects were controlled at the intersection of two or more microchannels. The control region was magnified by microscope and watched by a camera with a digital signal processing (DSP) chip. Image processing software on the DSP chip located objects in real time. In parallel, a LabVIEW program on the computer downloaded the position of the objects from the camera over an Ethernet connection, calculated control, and then applied control through a digital-to-analog converter. Video feedback was received from the camera through an analog video port, digitized, and displayed on screen for user

interaction. Users selected objects to control and where to move them to by single mouse clicks. Using this system, our group controlled single and multiple microspheres and yeast cells with ~1 μm accuracy, the first demonstration of electrokinetic tweezing.[112–114]

This first system had several disadvantages. Changes to the image processing software on the camera's DSP chip were slow because it had to be compiled and uploaded to the camera before control. As a result, imaging conditions needed to be known ahead of time and the code had to be properly debugged. Communication between the camera and computer required custom programs and protocols. The positions of the objects being controlled were sent over an internet server to a client running on the computer. The image being processed from the camera was only available in real-time through an analog video port, so an extra analog-to-digital video converter was needed to display the image on the computer for user interaction. The computer calculated control and interacted with the user through a LabVIEW program, but the control calculation itself was a MATLAB script, and user interaction was primarily limited to selecting objects with one mouse click and the desired position with another. This system had limited functionality and would be difficult and time consuming to replicate.

A new system was developed to streamline development and bring EK tweezers to non-specialists. In this new system imaging, control, and user interaction are all handled in a program written for the MATLAB software platform. MATLAB is used frequently in engineering and provides many functions that process images, communicate with hardware instruments, and interact with users. MATLAB is compatible with many cameras and voltage output devices, so it is easy to set up a new system using devices chosen specifically for a control application. MATLAB also provides a toolkit for

designing and developing graphical user interfaces (GUIs). The responsive GUI described here allows user to select and manipulate objects as if playing a game, program complex trajectories, and record experiments for later analysis.

3.2 Hardware
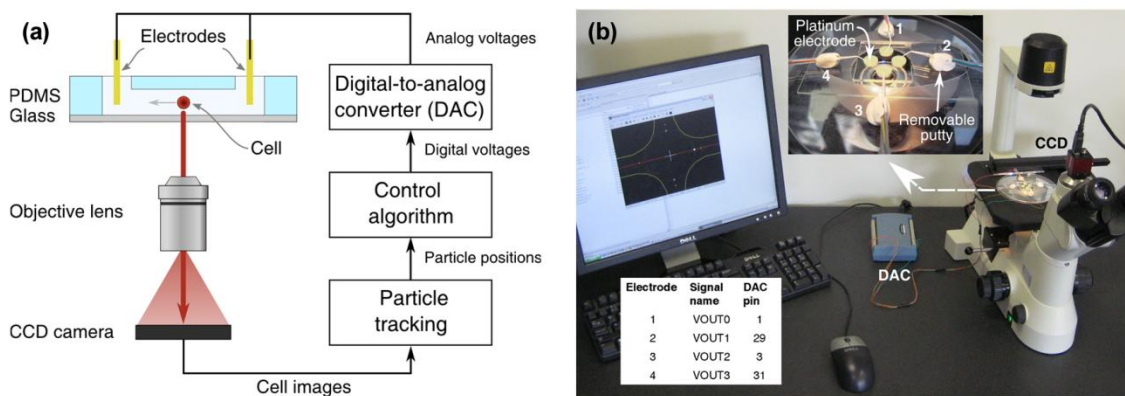
Fig. 3 Schematic of the experimental setup. (a) A CCD camera images the cells in bright-field or fluorescence illumination. A cell-tracking algorithm computes the position of the chosen cell and a control algorithm then determines the needed actuation voltages which are applied through a digital-to-analog converter (DAC) and platinum electrodes to the microfluidic device. **(b)** Photograph of the experimental setup with zoomed view of a microfluidic device. Here the yellow round shapes are the four reservoirs, platinum wire electrodes are brought in contact with the cell buffer fluid in these reservoirs. Left corner: The connection table for connecting the electrodes with the DAC (Measurement Computing USB-3101).

Fig. 3 shows an example of the new EK tweezing system. It consists of a microfluidic control device, inverted microscope, camera, voltage output device, and computer. The microfluidic device is placed on the stage of an inverted microscope (Eclipse TS100, Nikon, Tokyo, Japan) and is watched by the camera (Guppy F-033B, Allied Vision Technologies, Stadtroda, Germany). Platinum electrodes are held in each of four channel-end reservoirs with adhesive putty and connected to a digital-to-analog converter (DAC) (Measurement Computing, Norton, MA, USA) for voltage output. MATLAB software on the computer tracks objects imaged by the camera and calculates the control voltage to be applied by the DAC. The hardware shown here can be easily

replaced as long as the camera and voltage output device can communicate with MATLAB.

3.3   Microfluidic control device
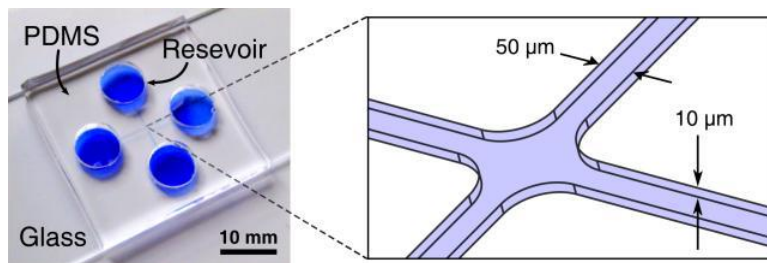
Fig. 4 Microfluidic control device for one object. The microfluidic device (left) consists of two intersecting microchannels each ~2 cm long made from PDMS using standard soft lithography techniques. Each channel is 10 µm deep and 300 µm wide except at the intersection (right), where it is narrows to a width of 50 µm to concentrate electrokinetic forces.

A microfluidic device with two intersecting microchannels is used for 2D control of a single object at a time. As shown in Fig. 4, the microfluidic control device is made of polydimethylsiloxane (PDMS).[121–124] The porous structure of PDMS provides good permeability for oxygen and carbon dioxide, making it safe for handling cells.[123,125] PDMS microfluidic devices are usually made by soft lithography.[126] First, a mold is created consisting of a silicon wafer on which the features of the microfluidic device are raised. The features can then be repeatedly copied by pouring a two-part liquid PDMS pre-polymer over the mold (*e.g.* Sylgard 184, Dow Corning, Auburn, MI, USA), curing it with heat until it is like rubber, and peeling it away from the mold. Functional elements such as valves, pumps, and sensors can be incorporated with additional processes. Microfluidic devices can also be made in plastic or glass by knife plotting, laser cutting, micromilling, and many other techniques.[15]

3.4   Modeling

Applying a voltage across the electrodes in the microfluidic device creates the electrokinetic forces used for control. Before control, the basic electric fields of the device are simulated in COMSOL. Fig. 5 shows the four basis electric fields for a microfluidic device with four electrodes. For each field, the end of one channel is set to 1 V while the other ends are set to 0 V, and all other boundaries act as electric insulation. All the fields are saved as grids that can be quickly referenced during control. Combining them according to the control algorithm creates an electrokinetic velocity that pushes the selected object from where it is towards where it should be.
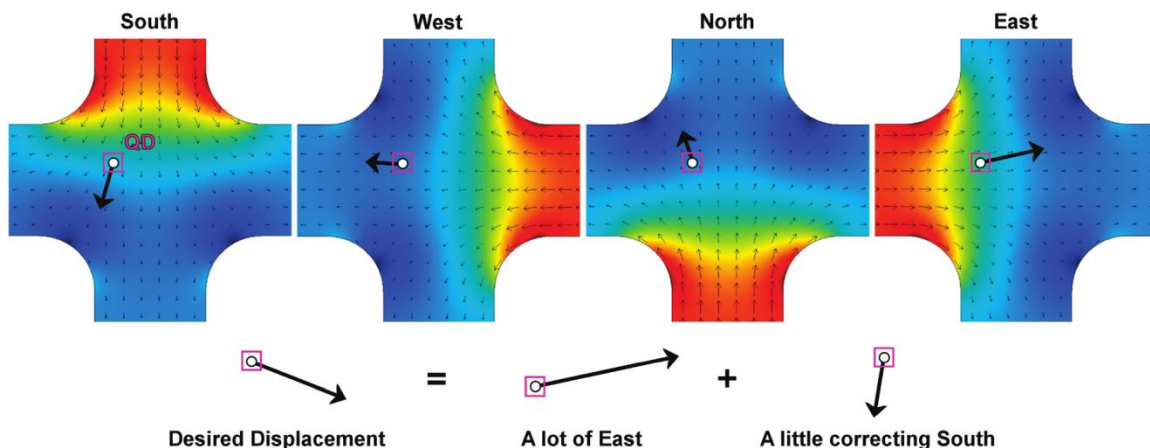
Fig. 5 Model of the four flow modes resulting from voltages applied to each electrode.[114,118] Any desired correcting velocity, at any particle location, can be created by combining these four actuation modes. Black arrows show the microfluidic velocities, color shows the applied electric potential, and the enlarged black arrows show an example of velocity decomposition.

3.5   Object tracking

Objects in the control area are monitored by microscope optics and a video camera. A basic setup is shown in Fig. 3. The microfluidic control device is put on the stage of an inverted microscope (TS100, Nikon, Tokyo, Japan) and viewed through a 20×

objective lens (Plan Fluor, Nikon, Tokyo, Japan). A video camera (Guppy F-033B, Allied Vision Technologies, Stadtroda, Germany) monitors the device and is connected to the desktop computer through an IEEE 1394 interface. The microscope and camera shown here can be easily replaced to meet the needs of other control applications as long as the position of the objects can be measured with enough resolution and speed.
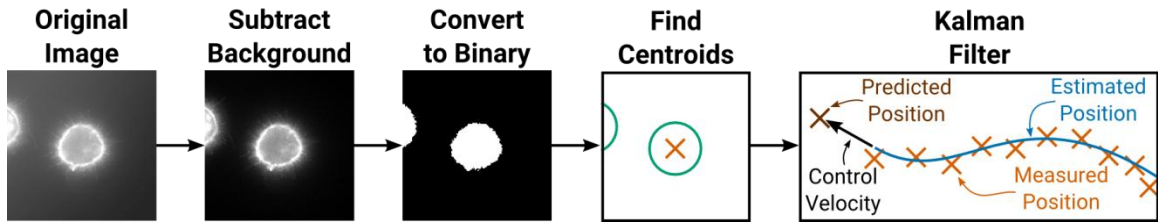
Fig. 6 Object detection imaging algorithm. Before tracking an object, a background image is saved when few objects are present in the device. During tracking, objects are detected by looking for groups of pixels that are brighter (or darker) than the background. First, the background is subtracted to remove device features. Next, the background-subtracted image is converted to black and white, where pixels greater than some intensity are set to 1 while all others are 0. The centroid of each group of bright pixels is found by averaging the position of each constituent pixel. If there is more than one object in the image, the centroid nearest the predicted position is accepted. The predicted position is found using a Kalman filter that accounts for noise in the system, and allows objects to be tracked in the presence of many other objects. To limit computational intensity, this algorithm is performed in a small window that follows each selected object.

Objects are detected in each new image by an image processing algorithm. For bright-field and fluorescent microscopy, it is often convenient to identify regions of pixels with values higher or lower than the background image, as outlined in Fig. 6 for bright objects on a dim background. Each image acquired from the camera is subtracted by a background image taken at some time when the control region was relatively free of particles, removing static device features. A binary image is produced from the difference image by setting pixels above (or below) a threshold to one, and all other pixels to zero. The binary image allows rapid morphological transforms such as hole filling and edge smoothing, if necessary. To account for the possibility that multiple particles are in the

search window, contiguous regions of pixels are labelled. The centroid of each contiguous region is calculated by averaging the position of each constituent pixel.

Objects are tracked between successive images by predicting their next positions. The initial position of an object is defined by a user, who clicks on the image in the vicinity of the selected object, or by automatically running the image processing algorithm over some region. In each subsequent frame, the precise centroid of the object is found by running the image processing algorithm for a small window around the predicted position of the object. If there are several objects in the search window, the accepted centroid is the one nearest the predicted position. Accurate prediction allows objects to be tracked through crowded populations of other objects.

The position of a tracked object is predicted by a Kalman filter. While it may be convenient to predict the position of an object based on the last control velocity, or to assume the object will be the nearest in the search window to its previous position, these approaches require careful control over device conditions. In practice, the microfluidic control device will have defects caused by mistakes made during fabrication or fowling from prolonged use. In addition, noise is introduced by the imaging and voltage output system. A Kalman filter accounts for these sources of noise and provides an accurate estimate of the actual and predicted position of an object in real-time.[127] For simplicity, it is assumed that an object moves in a straight line between successive images with the control velocity given by equation 8 ($\vec{v}_{EK} = \mathbf{A}\vec{V}$). This leads to the dynamic difference equation

$$\begin{bmatrix} \vec{x} \\ \dot{\vec{x}} \end{bmatrix}_k = \begin{bmatrix} \mathbb{I} & \Delta t \\ 0 & 0 \end{bmatrix} \begin{bmatrix} \vec{x} \\ \dot{\vec{x}} \end{bmatrix}_{k-1} + \begin{bmatrix} 0 \\ \mathbb{I} \end{bmatrix} \vec{v}_{EK}, \tag{12}$$

where $\vec{x}$ is the position of the object, $\dot{\vec{x}}$ is its velocity, and Δt is the period between the successive images at step $k - 1$ step k (*e.g.* $\Delta t = 0.05$ s for a 20 Hz control loop). The Kalman accounts for noise not considered by equation 12 to estimate and predict the position of an object. The expected noise in the system can be estimated, or measured using an auto-regressive filtering technique.[128] Filtered positions from the Kalman filter allow stable tracking and control of objects in the presence of other objects, imaging noise, and control noise.

3.6   MATLAB control program

The control program was written for the MATLAB software environment. MATLAB is a standard problem solving tool in engineering due to its stability, maturity, and ease of use.[129,130] MATLAB uses a scripting language that makes it easy to program linear algebra problems in control, and has toolboxes for image processing, hardware interfacing, and graphical user interfaces. For these reasons it is a convenient choice for developing our control system. Once mature, the system can be translated into a fast compiled language such as C and integrated into dedicated microcontrollers.

The control program runs in a loop at a fixed rate. At the beginning of each execution of the control loop, the most recent image is downloaded from the camera using MATLAB's Image Acquisition Toolbox. This image is displayed to the user in a graphical user interface (GUI) and processed by the image processing algorithm. The user can select an object visible in the image to control by clicking on it. The user can then set the desired position of the object by clicking and dragging it, or by drawing a trajectory for it to follow. A small image subregion around the predicted position of each

selected object is extracted from the camera image. Objects in the image are detected using image processing functions from MATLAB's Image Processing Toolbox. Positions are filtered by the Kalman filter and used by the control algorithm to calculate the control signal. The control voltage is applied to the microfluidic control device through a voltage output device using MATLAB's Data Acquisition Toolbox, and fed back to the Kalman filter to predict the next position of the objects. This loop repeats as quickly as possible, selected objects to their desired positions.

3.7   Graphical user interface

3.7.1   Overview

The GUI lets users interact with the control program. As shown in Fig. 7, the GUI has four regions (from top to bottom): a menu, a toolbar, a video display, and a bar for control information and settings. The menu gives access to infrequently used functions that handle hardware configuration and recordings. The toolbar gives easy access to frequently used functions for control: on/off, geometry calibration, trajectory drawing, and experiment recording. The video display shows the current camera image, icons showing the estimated (square) and desired (circle) positions of selected particles, and an outline of the device geometry. The left side of the bar on the bottom of the window shows the current frequency of control. The right side of the same bar provides fields that set the gain of the control algorithm and the velocity at which a selected object follow trajectories.

Fig. 7 Graphical user interface (GUI) and coordinate calibration. This simple GUI allows users to select objects, drag them by mouse, draw trajectories for objects to follow, and record experiments. To properly transform between the coordinates used for image processing and those used for control calculations, a schematic of the control device must be dragged, rotated, and scaled to match the image.

3.7.2   Setup and initialization

Before control, the voltage output device and video camera must be configured in MATLAB. Communication with DACs is supported through MATLAB's Data Acquisition Toolbox, but may differ between manufacturers, so initialization and voltage update functions must be programmed manually. Functions for two common manufacturers (Measurement Computing and National Instruments) are included with the program. Microcontrollers used for voltage output and some DACs can be controlled through a serial interface with functions from the Instrument Control Toolbox. Cameras often use standardized protocols such as DCAM and GigE that are well supported by the Image Acquisition Toolbox. To choose a supported camera, open the control GUI and select the device and resolution from the list of cameras in the "Video Input" menu. Camera settings, which may differ between manufacturers, are tuned in MATLAB's image acquisition GUI or in the initialization function of the control program. Cameras

that use proprietary protocols can be used by manually programming drivers when an appropriate programming interface is available.

During control, object positions are first measured relative to the camera image and need to be transformed into positions relative to control model. The transformation between image and model coordinates is defined by aligning a schematic of the model drawn on top of the image. To start alignment, press the "Channel Geometry" button at the left-most position on the toolbar, as shown in Fig. 7. Translate the schematic by dragging the white cross-hair at the center of the model to the center point of the control area. Rotated and scale by dragging the circular white handle at the edge of the control region (white dash). To rotate alone, hold the control key while dragging, or scale alone by holding the shift key while dragging. Repeat until the schematic matches the edges of the device. For symmetric control devices it is also important to make sure that the schematic is rotated so that the channel labels on the schematic match the channels of the control device. End alignment by pressing the "Channel Geometry" button again. This process is usually more convenient than aligning the microfluidic device on the microscope stage, and can be automated in the future with image processing that finds the edges of the channel.

To start or stop control, press the "Control on/off" toggle button to the right of "Channel Geometry." Object tracking works regardless of whether control is activated.

3.7.3 Manual control by mouse

The easiest way to interact with objects is to click and drag them by mouse. Select an object for control by left-clicking in its vicinity. A square icon and a circle icon will

appear around the object as shown in Fig. 8. The square icon displays the estimated position of the object and will follow the object around. The circle icon represents the desired position of the object. To move an object by mouse, drag the circle icon to the desired position. If control is fast enough, the object will closely follow the circle and the mouse. To stop tracking and control of an object, right-click either icon.
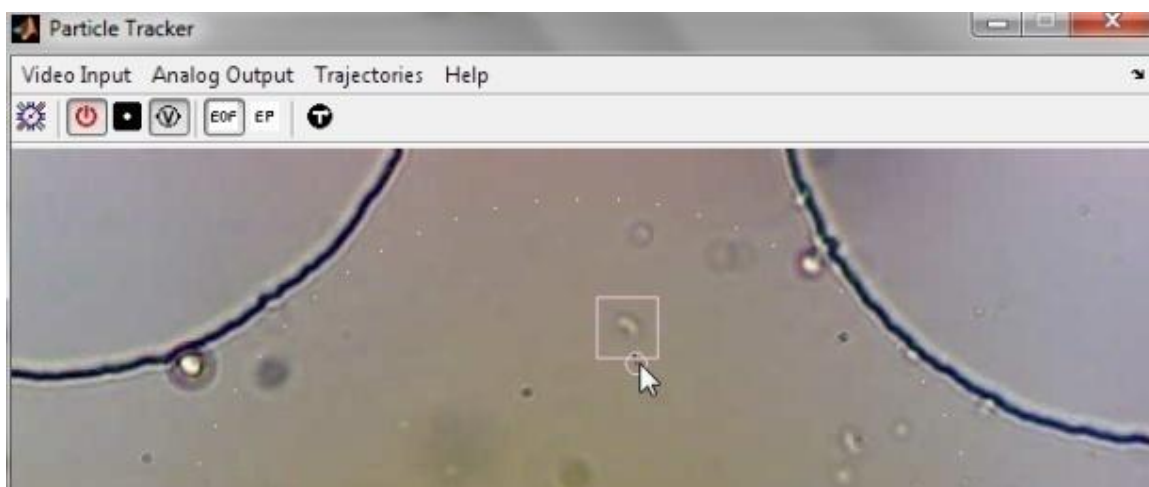
Fig. 8 Clicking and dragging objects. Left-clicking on an object initiates a new instance of the image processing and tracking algorithm. The square marker around the object indicates the current estimated position from the Kalman filter and the circle marker indicates the desired position. Objects are moved by clicking and dragging the circle marker to any point in the control region. The object will closely follow the mouse cursor if control is fast enough.

Clicking and dragging allows manual control of objects in the device similar to using tweezers in real life. This is especially useful for testing new fluids and objects. Fig. 8 shows manual trapping and manipulation of a swimming microbe. For this experiment, we used untreated water from a nearby stream. In addition to organic debris, there were many relatively fast swimming microbes. Despite the speed of the microbe, the feedback control algorithm is able to push it toward the mouse anywhere in the control region. Once control was ended, the microbe quickly escaped the trap and swam to the wall of the channel.

3.7.4   Automated control along trajectories

Control tasks can be automated and repeated by programs that replace mouse control. It is important to be able carry out and repeat precise experiments, but difficult to achieve using the mouse alone. Instead, programs run in parallel to the control program can replace mouse control by automatically selecting objects and setting their desired positions. For example, objects can be positioned along complex trajectories, positioned relative to specific features of the device, or scanned over a grid. Automation of tasks like these is vital to the experiments discussed in this dissertation.

| (a) | (b) | (c) |
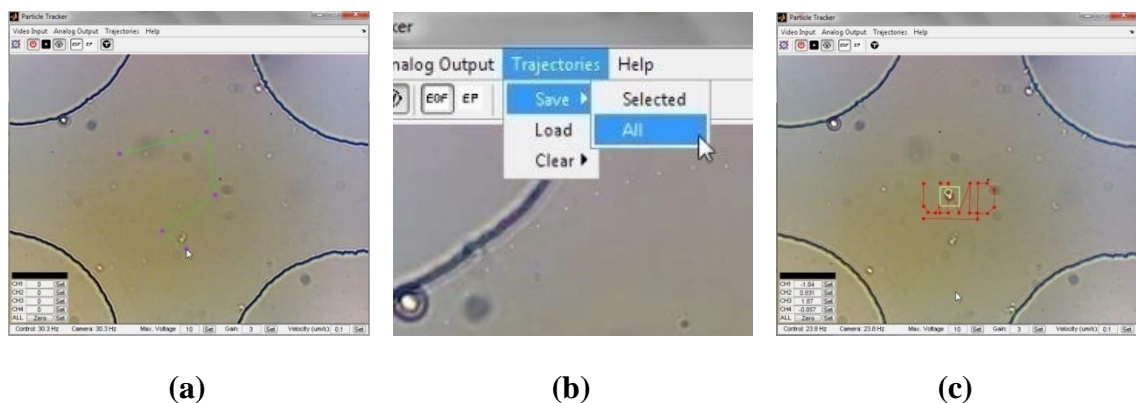
Fig. 9 Trajectory automation. (a) Trajectories can be drawn by clicking points in the control area. **(b)** Save and load trajectories using the "Trajectories" menu for repeated experiments. **(c)** Attach objects to trajectories by holding the shift key while dragging objects to the start of the trajectory. Double-click to start trajectory following.

Basic automation built into the program moves objects along trajectories drawn by the user. Trajectories can be drawn relative either to the microfluidic channels or the camera image. To start drawing a trajectory relative to the channels, click the "Edit Channel Trajectories" button on the toolbar. Channel trajectories transform along with the calibration schematic and are useful when objects must interact with a feature of the control device, or when saving and loading trajectories to repeat experiments. To start

drawing a trajectory relative to the image, click the "Edit Pixel Trajectories" button. Pixel trajectories do not transform and are useful for control tasks that do not need to be calibrated or for control demonstrations that should be kept at a certain orientation on the image. Start a new trajectory by left-clicking any image region not already occupied by a trajectory. As shown in Fig. 9(a), left-clicking another point draws a line from the previous point to the new one. Repeat to draw the desired trajectory. To move a point on a trajectory, click and drag it to a new position. To move an entire trajectory, hold the shift key while clicking and dragging any point on the trajectory. To delete the trajectory, right-click any point on it. To start a new trajectory, right-click any region of the image not already occupied by a trajectory. To finish trajectory drawing, click either the "Edit Channel Trajectories" or "Edit Pixel Trajectories" toolbar button again.

Trajectories can be saved and opened for later experiments using the "Trajectories" menu (Fig. 9(b)). Trajectories are saved as MATLAB data files that contain the positions of each point in the order they were drawn. Precise, high resolution trajectories can be created with MATLAB scripts or CAD programs by following this format.

For control, the desired position of the object is repeatedly set to a position along the linked trajectory (Fig. 9(c)). To link an object to a trajectory, hold the shift key while dragging the object to the start of the trajectory. To set the velocity of the object on a trajectory, set the "Velocity" field of the control settings toolbar. To start or stop trajectory following, double-click either the object markers. If there are multiple objects linked to trajectories, start all of them at once by clicking the "Play All Trajectories"

button in the toolbar. Trajectory following automatically stops when the end of the trajectory has been reached.

3.8   Manipulation of circulating tumor cells

One application for EK tweezing is monitoring and testing free-floating circulating tumor cells. Circulating tumor cells (CTCs) are cancer cells that are shed by a primary tumor into the bloodstream, travel some distance, reattach in another tissue, lay dormant for some time, then finally develop into metastatic tumors.[4-6] Tumors seeded by CTCs are a major cause of patient death because they avoid detection and treatment by methods that work on large tumors.[131] Advanced clinical imaging only detects tumors larger than ~5 million cells[132] and chemotherapies that target cell division do not affect CTCs while they are dormant.[133] However, CTCs appear in the blood of 30-50% of cancer patients who show no other evidence of metastasis, and strongly predict metastatic progression and death from cancer.[134,135] More research is needed to find new ways to treat CTCs, as well as learn how current treatments already affect them.

CTCs have long hair-like "microtentacles" that help them to attach to each other, penetrate blood vessel walls, and reattach in new tissues.[136-138] Microtentacles are long extensions of the cell membrane that arise when microtubules extend away from the center of a cell and overcome the tension of the actin cortex beneath the cell plasma membrane.[139] Microtentacles have been largely overlooked because they are suppressed[136,140,141] by increased tension of the actin cortex[140,142] when cells attach to a matrix or surface, where they are most commonly imaged. However, microtentacles of free-floating CTCs promote CTC aggregation[139,141,143] and attachment to endothelial

tissue.[144] CTC aggregates predict poor patient prognosis[19] and, in animal experiments, attach more frequently in lung capillaries than solitary CTCs.[145]

Several changes were made to the microfluidic device to allow EK tweezers to manipulate single cancer cells with microtentacles. Previous experiments controlled fluorescent microspheres and yeast cells with < 5 µm diameter in a microfluidic device that had ~10 µm high channels and large ports open to the air. Objects were suspended in deionized water and loaded into the device by hand. Any flow in the device was eliminated by making sure the level of the fluid was the same in all holes. The same sample could be controlled for long periods. This setup leads to several problems when controlling cancer cells. Breast cancer cells like the ones we would use are ~20 µm diameter, prefer biocompatible conditions, and quickly attach to surfaces. To account for the diameter of the cells as well as the presence of microtentacles, a new microfluidic device was made with 50 µm high channels. The device was monitored by a microscope whose stage was enclosed with an incubator that kept the sample at ~37 ℃ (body temperature). The ports of the device were sealed to limit disturbance from the incubator's fan, and to facilitate conveyance of cells. Cells were suspended in standard cell medium (Dulbecco's Modified Eagle's Medium) and conveyed between the southwest and southeast ports of the device by adjusting the level of the sample between two centrifuge tubes connected to the device by plastic tubing. New cells were introduced to the device on demand by moving one tube higher than the other. The six remaining channel-end ports were connected to electrodes through electrogel bridges put together by seating plastic pipette tips filled with electrogel (Spectra 360, Parker Laboratories, Fairfield, NJ, USA) into small holes at the end of the channels. In addition to preventing

air flow disturbances, the electrogel bridges protect cells from electrolysis. The PDMS chip was bonded to a glass coverslip by plasma treatment (BD-20AC, Electro-Technic Products, Chicago, IL, USA) to allow tubes and pipettes to be attached to the chip without breaking its bond to the coverslip.

The adhesive force between two cells was measured by bumping them into each other. One cell was held stationary by anchoring it to the glass surface of the device, and then a free-floating cell was pushed into it and pulled away at constant speed along a straight trajectory. While it is possible to push two free-floating cells together using the control algorithm, it is difficult to create opposing velocities in the same vicinity without high voltages that can damage cells or cause control instability.

First, one cell is anchored in place in the control region. Before filling the device with cell buffer, the device is filled with a 0.1% solution of poly-L-lysine (PLL) in water, incubated for ~10 minutes, and then washed with PBS. PLL encourages rigid attachment of stationary cells to the glass bottom of the control device. Cells are selected as they are conveyed into the control area, moved to a convenient region, and held in place for 1-2 minutes. Healthy cells attach with a durable bond while unhealthy cells are washed away by flow. As shown in Fig. 10, this method can also be used to pattern cells in arrays for studying many cells in parallel as well as interactions between them.

Attachment forces between two cells are measured by bumping a free-floating cell into an anchored cell. We drag a trajectory that leads to and from the attached cells. As shown in Fig. 11, the free-floating cell follows the desired position closely as it approaches the attached cell. As it is pulled away, it resists control. As the difference

between the desired position and the actual position of the object increases, the control force increases until the control force overcomes the attachment force and the cell quickly reaches the desired position.
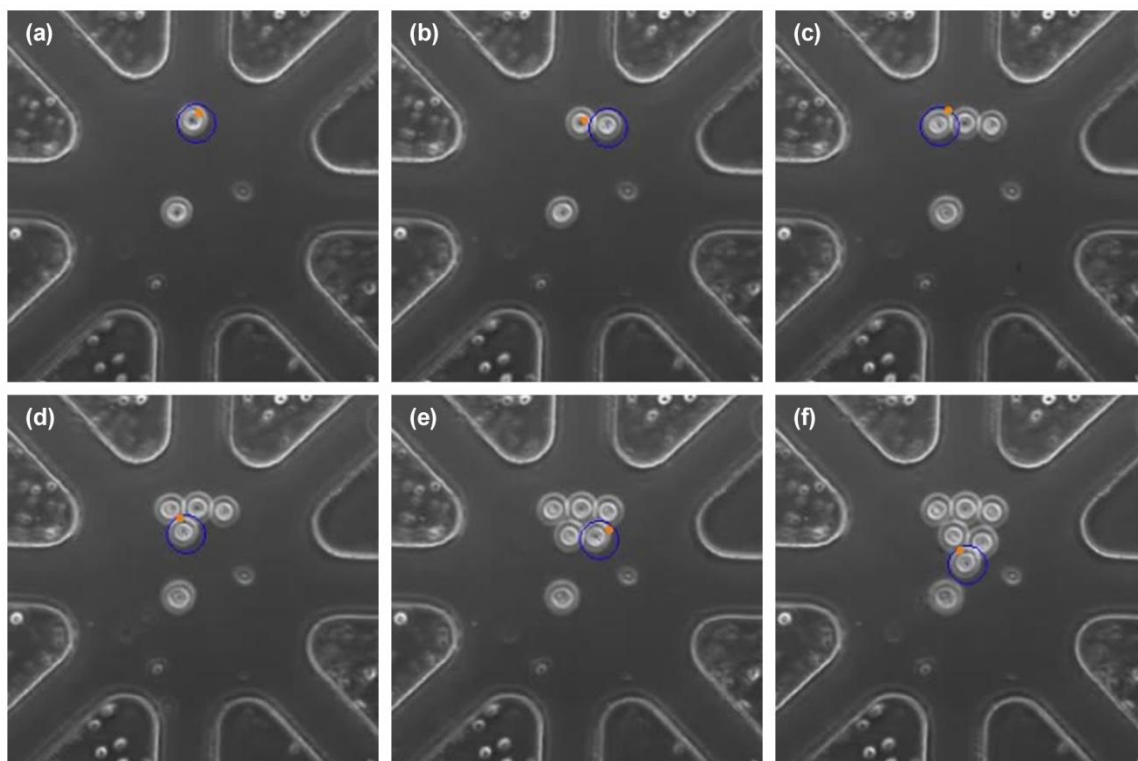
Fig. 10 Dynamic cell patterning. Cells are introduced to the control region of a microfluidic control device with four crossing channels. In each frame **(a-f)** a new cell is selected and held in place to form a pyramid.

Improvement of measurement, drug introduction, and imaging will allow this system to better monitor the effects of drugs on circulating tumor cells and their microtentacles. Attachment forces between cells can be estimated based on the strength of the applied control, but are not easy to verify. Measurement of attachment forces can be improved by modeling the effect of the cells on their local electrical and fluid fields, and directly sensing forces in the device. The effect a drug has on a CTC is dependent on its concentration, uptake, and duration of exposure. Drugs and other reagents can be

carefully introduced and washed away by adding microchannels dedicated to this purpose. Microtentacles are very thin and difficult to image, especially as they drift out of the focal plane. Imaging this system with a confocal microscope will improve imaging of the dynamic response of CTCs and their microtentacles to drugs.
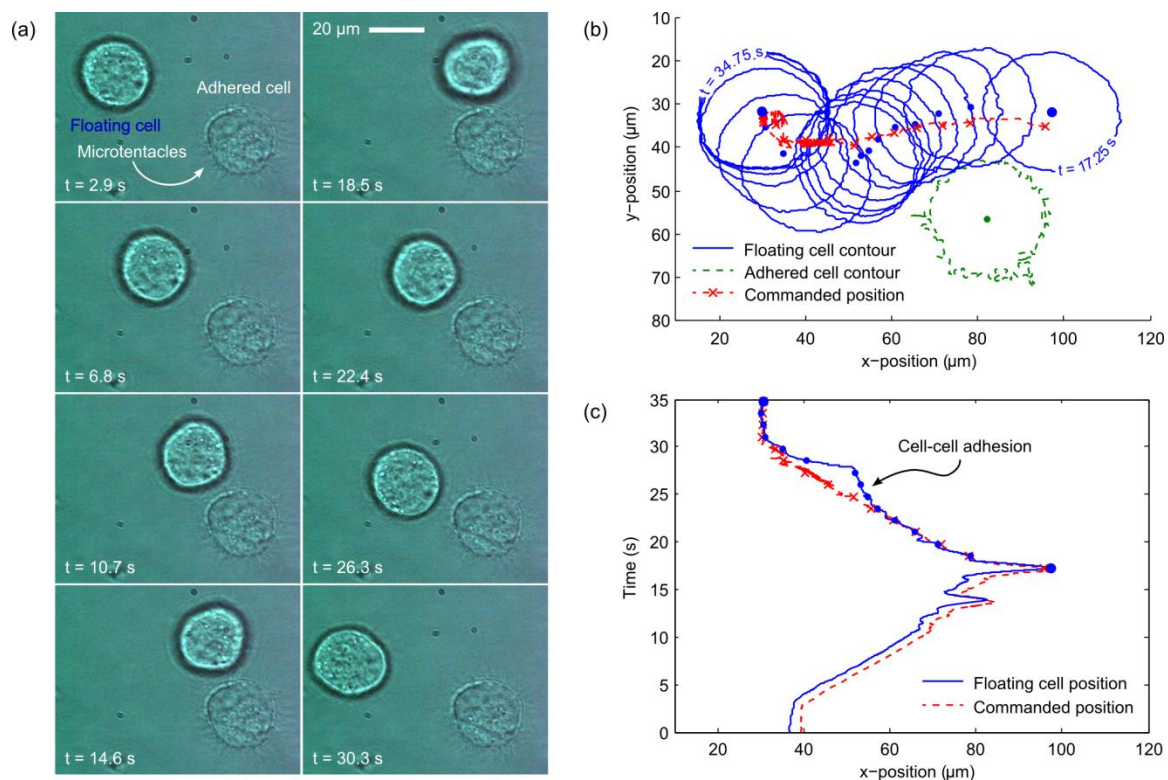
Fig. 11 Control of a single free-floating human breast tumor MDA-MB-436 cell. **(a)** The cell was steered toward and away from another breast tumor cell that had adhered to the chip surface and whose microtentacles are visible as faint white extensions. **(b)** The trajectory of the floating cell as it is pulled away to the left from the adhered cell (during t 5 17.25 s to 34.75 s). The commanded centroid position is shown by red crosses while the measured path and cell boundary is shown by blue dots and curves. The boundary of the adhered cell is shown in dashed green lines. **(c)** The *x*-location of the floating cell during inward and outward motion (commanded 5 red dashed; measured 5 blue solid). When the cell is pulled back, cell-to-cell adhesion retards leftward motion until the applied control breaks the two cells apart.

3.9   Manipulation of quantum dots

EK tweezing can also be used to select and position nanoparticles such as quantum dots nanoscale precision for quantum computing and biological labeling.

Quantum dots (QDs) are semiconducting crystals with dimensions usually less than 10 nm used as single-photon sources.[146] Compared to organic dyes commonly used for labeling and imaging in biology, QDs have long life and narrow, tunable emission spectra.[147–149] As part of photonic devices, QDs drive optical switches,[8] lasers,[150] and solar cells,[151] but need to be placed in regions that measure around 150 nm for efficient light-matter interaction.[152] Positioning single free-floating QDs in nanoscale regions is especially difficult due to Brownian motion, which scales inversely with the radius of an object. QDs quickly diffuse out of optical and DEP traps, whose forces scale with the volume of an object.[58,153] EK tweezers use fluid drag forces that only scale with radius[45,42] and can be used to position single QDs with nanoscale precision.[117,154]

Imaging was optimized for high accuracy and QD blinking. QDs were imaged using optics with high numerical aperture and a sensitive video camera (C9100-13, Hamamatsu Photonics, Hamamatsu City, Japan) under dark conditions. A sub-pixel imaging algorithm determined the position of QDs with accuracy smaller than the wavelength of light.[155] When a QD blinks off, control is stopped and the image processing region around the QD is expanded to account for uncontrolled diffusion. Normal control and imaging start again as soon as a bright QD is detected in the expanded window.

Positioning error from Brownian motion was reduced by suspending QDs in a viscous buffer and keeping them in focus. The viscosity of water was increased by adding an associating polymer (ACRYSOL RM-825, Dow, Midland, MI, US). EO actuation lost due to increased viscosity was recovered by adding a zwitterionic betaine surfactant and amplifying the control signal. Feedback control further reduces positioning error, but

only in two dimensions. Even during control, QDs are still able to diffuse away from the focal plane and blur, degrading the performance of the imaging algorithm until they are lost. To keep QDs in focus, a piezoelectric stage controlled by a focusing algorithm adjusted the distance between the control device and the microscope objective.
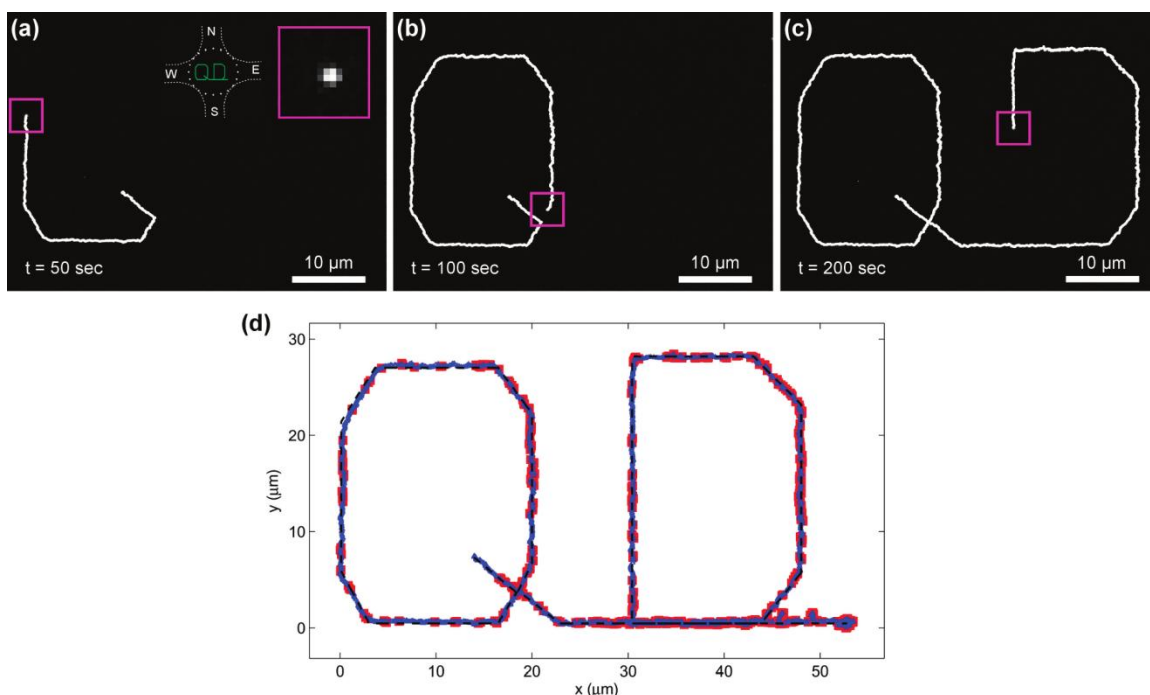
Fig. 12 Single quantum dot trajectory. (a-c) Time-stamped CCD camera images of a single quantum dot being steered along the desired trajectory. The white trace shows the measured path of the quantum dot up until its current location. The square magenta box shows the subpixel averaging window used to determine the current position of the QD. The insets in panel a show the orientation of the channel with the trajectory (green) and a close-up of the subpixel averaging window which contains the QD near its center. (d) Plot of quantum dot position along its trajectory. The dotted black line shows the desired trajectory programmed into the controller. The actual measured QD trajectory is shown in blue. The solid red squares depict when the quantum dot blinks off. At the end of the trajectory the QD is held in place for 2 min. The mean displacement from the trajectory is calculated to be 119.5 nm.

The adjustments to imaging and the fluid allowed a single QD to be trapped with 45 nm accuracy and, as shown in Fig. 12, steered along a 2D trajectory with 120 nm accuracy.[117] It was also possible to trap a 6 nm QD for at least one hour, only stopping when the QD was photobleached.
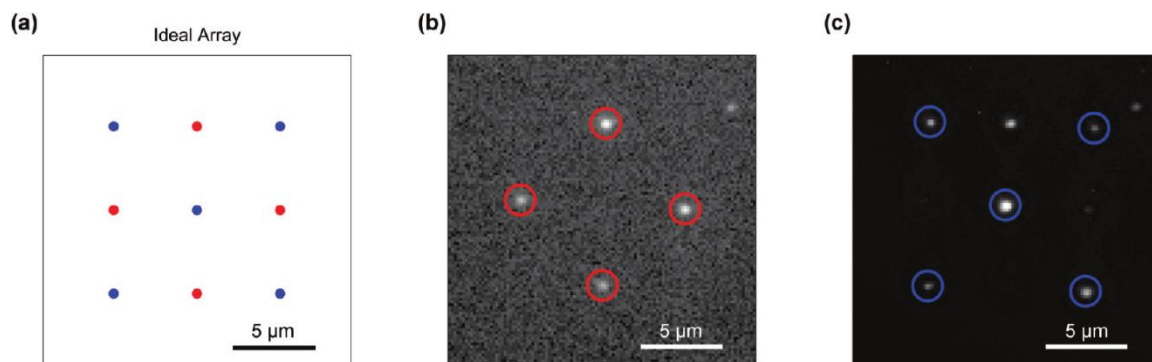
Fig. 13 Array of preselected QDs. (a) Idealized array design with the two different types of QDs alternating in a checkerboard pattern. (b) Completed array as visualized through a bandpass filter centered at 710 nm. The four QDs emitting at ~705 nm are circled in red while the 655 nm emitting QDs are not visible. (c) The same completed array as visualized through the 655 nm band-pass filter. The QDs emitting at 655 nm are circled in blue.

QDs were also immobilized with 127 nm precision by polymerizing a photoresist added to the buffer.[154] The buffer was made to polymerize with the addition of a photoresist that cross-linked when briefly exposed to a beam of ultraviolet (UV) light. In addition to immobilizing the QDs, the photoresist pushed them out to the walls of the microfluidic device. QDs were immobilized at the glass bottom of the device by steering them to the UV beam. Multiple QDs were arrayed as shown in Fig. 13 by moving the control device relative to the UV beam. QDs confined to the glass bottom of the device stayed in focus for reliable 2D control and, once polymerized, remained attached to the glass and continued to emit even after the control device was removed.

3.10   Summary

The implementation of electrokinetic tweezers presented in this chapter uses commercially available hardware and software that makes it easy to bring object manipulation to new settings. The first generation EK tweezers system used a complicated smart camera that led to redundancies in communication and limited

development of the EK tweezers as a useful tool to other researchers. A new system was developed that used a desktop computer and readily available video and voltage output hardware. Control software was written for MATLAB, a mathematical prototyping platform prevalent in engineering. Using this system, objects are controlled at the intersection of two or more microchannels. The EK physics of the device are modeled in COMSOL and saved before control. During control, objects in the control region of the device are monitored by a microscope and camera. The control program detects objects in each image and links them to previously detected objects using a Kalman filter. The voltage needed to push a selected object from where it is to where it should be is found by the model-based control algorithm and applied to the device through the voltage output device. This process is executed repeatedly and pushes an object closer to its desired position each time.

Users interact with the control program through a graphical user interface that displays the latest image from the camera and provides a set of tools that automate control tasks and record experiments. After setting up hardware and calibrating the orientation of the device, users select objects and set their desired positions primarily in one of two ways. Most simply, users click on an object and drag it to the desired position by mouse. For precision and repetition, users draw trajectories and attach objects to them. Experiments can be recorded and saved for post-processing.

Due to its flexibility in hardware and portability in software, this implementation is easy to use in new research settings. Here, we showed manipulation of motile microbes, floating cancer cells, and quantum dots. Wild motile microbes were controlled in a sample of water from a stream, and showed the robustness of the control algorithm to

unexpected variations in object velocity. Cancer cells were bumped into one another, and the attachment between them was measured. This method could be used to evaluate the effectiveness of drugs on circulating tumor cell, which are an important indicator and precursor of metastasis. Quantum dots were trapped with ~45 nm accuracy, and immobilized in a photocurable polymer. The ability to position nanoparticles such as quantum dots in the high field regions of nanophotonic structures is vital to the development of quantum information processors.

Future iterations of this system can be sped up and miniaturized. MATLAB was an excellent platform for developing EK tweezers into a robust and user-friendly system, but is primarily a mathematics prototyping platform that favors ease over speed. The next version of the control program would benefit from a faster scripting language such as Python or returning to a compiled language such as C. A full MATLAB installation also requires significant storage and processing power. While there are tools to limit the processing requirements for MATLAB programs, moving to another language would enable the use of a dedicated microcontroller or a dedicated single board computer such as a Raspberry Pi. Finally, the next version of the GUI can be designed for touch-screen tablets and phones, allowing users even easier control over their samples.

Chapter 4

Nanowire Assembly

4.1   Background

Nanosystem engineering paves a pathway toward inexpensive[156] and high bandwidth[157] nanoelectronics, subwavelength photonics,[158] ultrasensitive biological detectors,[159] customizable metamaterials,[160] and quantum circuits.[161] These applications require controlled interactions among different nanostructures such as quantum dots,[11] nanowires,[162] and plasmonic nanoantennas.[163,164] Nanostructures can be prepared by solution-phase chemistry with high uniformity and superb properties. However, integrated devices require the ability to assemble individual components in specific geometries with nanoscale precision. On-chip assembly approaches that rely on random deposition can assemble small-scale devices with a few interacting components.[163–165] However, these approaches suffer from low device yield, especially when constructing larger systems with many components. Deterministic assembly methods overcome this problem by positioning preselected nanostructures at desired locations on demand.

Deterministic assembly relies on the ability to manipulate nanostructures with nanoscale precision. Optical tweezers can manipulate[166] and assemble[41,167,168] nano and micro-scale structures in three dimensions using optical gradient forces that are proportional to the structure's polarizability. Because polarizability scales with volume, optical manipulation of nanoscale structures is challenging.[41] Magnetic tweezers[76] or dielectrophoretic actuation[153] can also manipulate nanostructures, but these methods

apply forces that also scale with volume. Mechanical tips have been used to drag or push nanostructures along a surface and position them with nanoscale precision.[169] This technique requires complex stabilization and control that is highly dependent on both the material composition of the nanostructure and the properties of the surface.[170] Mechanical forces can also damage the positioned nanostructure.[171]

Flow control is an alternate strategy for positioning nanostructures along a surface.[154,115] This approach uses fluid flow in a microfluidic device to move structures suspended in the fluid.[113] A feedback control system tracks an individual nanostructure in real time and continuously actuates flow to correct its position, which can be controlled with 39 nm precision.[115] This precision is insensitive to the composition or size of the structure and is determined primarily by the tracking precision and the accuracy of the control algorithm. Flow control can also manipulate a broad range of structures including fluorescent molecules,[95,172] quantum dots,[115,117,154,172] nanowires,[173] and live cells.[114] This versatility is vital for assembling nanosystems composed of many different materials using a single manipulation platform.

Here we demonstrate the use of flow control within an aqueous photoresist for the sequential positioning and immobilization of individual nanostructures to form nanoassemblies. We develop a toolbox of capabilities for positioning, orienting, and immobilizing nanostructures. We use obstructions in the microfluidic device as pivots, barriers, and guides to orient, separate, and combine multiple nanostructures. Once a nanostructure is positioned and oriented, we immobilize it by locally polymerizing the surrounding photoresist with UV illumination. As a demonstration of the scalability of the approach, we create nanoassemblies composed of multiple silver nanowires.

4.2 Experimental setup for microfluidic control
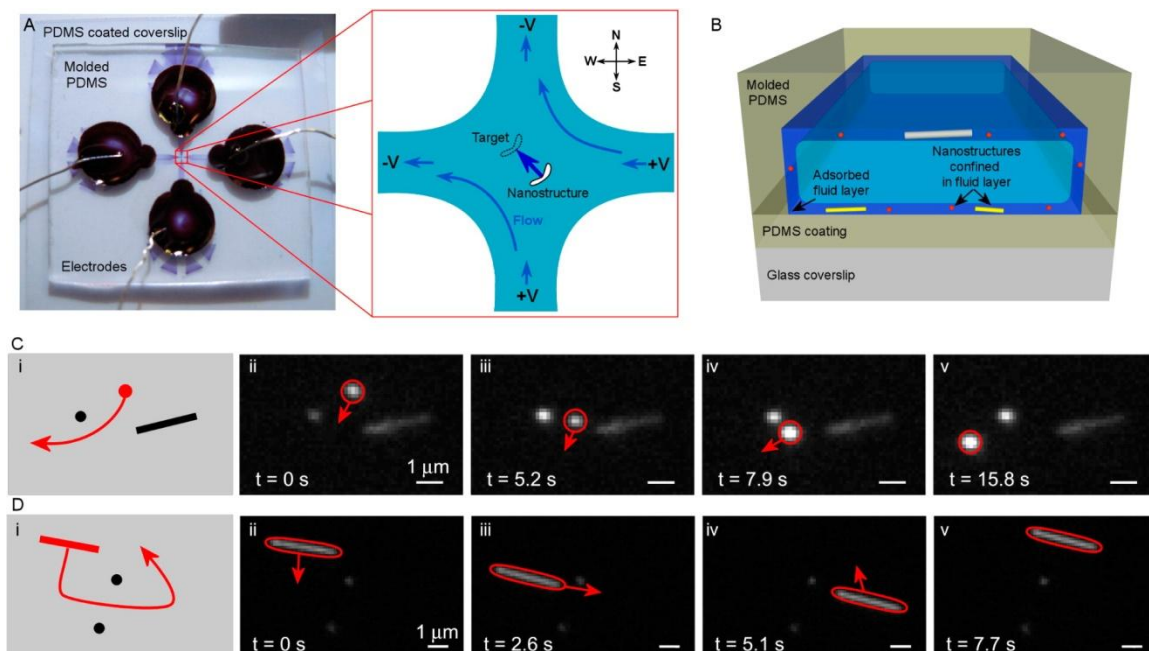
Fig. 14 Electrokinetic control of nanostructures. (a) Optical image of the microfluidic device. Channels are formed from molded PDMS placed on top of a PDMS-coated coverslip. Reservoirs are cut from the PDMS to access the channels (here filled with a dark fluid). Electrodes placed in the reservoirs actuate electroosmosis. The expanded region corresponds to the control chamber in the center of the cross channel. Voltages applied to the four electrodes create electroosmotic flow to move a nanostructure in any desired direction within the control chamber. **(b)** Schematic side view of the microfluidic channel depicting the fluid layers that confine nanostructures to the device surfaces. The microfluidic device is 5 μm high and the fluid layer is approximately 100 nm thick. **(c)**)i) Schematic of quantum dot steering between two nanostructures adhered to the device surface. (ii–v) Time-stamped images of the steering process. Arrows denote the direction of fluid flow. **(d)** (i) Schematic of silver nanowire steering between two nanostructures on the surface. (ii–v) Time-stamped images of the steering process. Arrows denote direction of fluid flow.

Fig. 14(a) shows an optical image of the flow control device used to manipulate nanostructures and create nanoassemblies. The device consists of two orthogonal microfluidic channels that intersect to form a control chamber (indicated by the red box). We mold channels in polydimethylsiloxane (PDMS) and place them on top of a PDMS-coated coverslip. The control chamber is approximately 100 μm in diameter and 5 μm in height. Electrodes placed in the four channel reservoirs actuate electroosmotic flow[44] within the control chamber along the four cardinal directions (North, South, East, and

West).[114] We actuate flow to move a suspended nanostructure in any desired direction by applying a combination of these four voltages, as illustrated in the red zoom-out box. To achieve nanoscale positioning, we use feedback control, which tracks the position of a suspended nanostructure in real time using an image processing algorithm.[155] The measured position serves as an input to a feedback controller that creates correcting flow to move to and maintain the nanostructure at a desired location.[114]

We perform all measurements using an inverted microscope system. An oil-immersion objective with an NA of 1.45 images nanostructures suspended in the control chamber, while an EMCCD camera acquires images at a 10 Hz frame rate. The control algorithm uses the acquired images to calculate the centroid position of the nanostructure and to adjust the voltages applied to the microfluidic device accordingly. We image non-fluorescent nanostructures using white-light illumination. Fluorescent nanostructures are imaged by exciting with a 532 nm laser source and focusing the collected emission to the camera.

4.3 Fluid chemistry

Flow control positions nanostructures along the plane of the chip surface. To prevent nanostructures from diffusing out-of-plane, we use a specialized fluid chemistry[154] that confines them to within 100 nm of the surface of the device, as depicted in Fig. 14(b). The control fluid is an aqueous solution containing a partially miscible acrylic monomer resin (SR-9035, Sartomer). We manipulate nanostructures in-plane on either the top or bottom of the device. The fluid also contains a rheology modifier (Acrysol RM-825, Rohm and Haas Co.) that increases viscosity to reduce Brownian

motion,[174] as well as a zwitterionic betaine surfactant (EDAB) that improves electroosmotic actuation along the PDMS surfaces.[175] The fluid is composed of 40–52.5% by volume monomer resin, 1.31–0.83 wt % rheology modifier and 0.30 wt % EDAB. It also contains 0.5 wt % of a water-soluble photoinitiator.[176] The photoresist polymerizes when exposed to UV light to immobilize nanostructures within the locally exposed region.[154] We polymerize the photoresist using a 375 nm UV laser focused through the bottom glass coverslip.

4.4   Positioning nanoparticles with flow control

We first demonstrate steering of colloidal quantum dots and silver nanowires. We use commercially available CdSe/ZnS quantum dots (Ocean Nanotech) and silver nanowires that we synthesize by reducing AgNO3 with ethylene glycol, using a procedure modified from reference [177]. The quantum dots are mixed in with the fluid while silver nanowires are locally deposited onto the device surface prior to filling. Some of the deposited nanowires detach from the surface and become suspended when the device is filled with fluid. Fig. 14(c and d) are series of optical images showing manipulation of a single quantum dot and a single silver nanowire, respectively. Fig. 14(c) shows a single quantum dot steered between a quantum dot and a silver nanowire that are immobilized to the surface. Fig. 14(d) shows a silver nanowire steered between two silver nanoparticles that are immobilized to the surface. In both cases, all three nanostructures were in the same focal plane, indicating that they were all at the surface of the device.

In previous work, we used flow control to position quantum dots with 39 nm precision.[115] Here we show that flow control can position silver nanowires with significantly better precision. We determine this precision by holding a silver nanowire in place and continuously monitoring its centroid position for 60 s. From the measured positions, we find the standard deviation of the wire position to be $\sigma_p = 5$ and 3 nm in the directions perpendicular to and parallel to the wire axis. These numbers are corrected for noise in the tracking algorithm, which we determine by tracking a stationary wire that is immobilized on the sample surface.
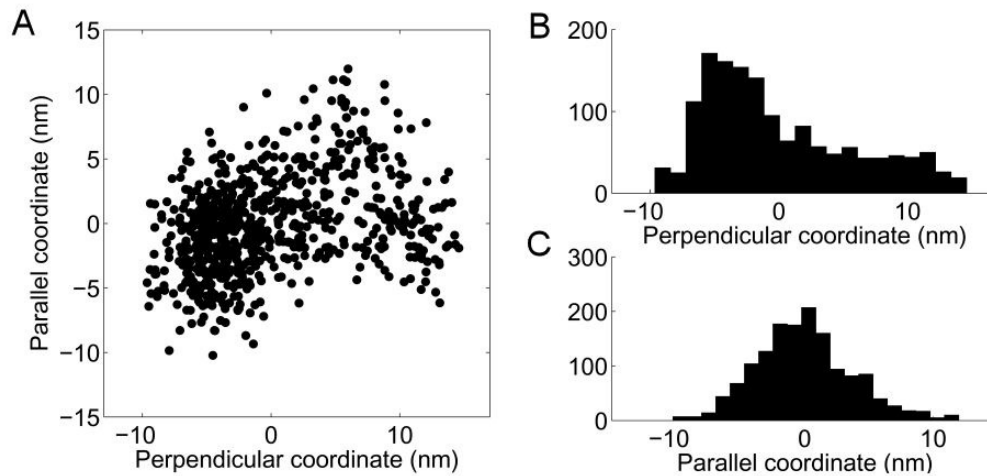
Fig. 15 Positioning precision for a silver nanowire. (a) Scatter plot of the measured centroid location of a nanowire held in place by flow control. Histograms of the measured positions in the direction **(b)** perpendicular and **(c)** parallel to the wire axis.

We determine the precision for positioning a silver nanowire by holding a single nanowire in place and continuously monitoring its position. Fig. 15(a) is a scatter plot of the held nanowire positions, which are rotated so that the x (y) coordinate correspond to the direction perpendicular (parallel) to the wire axis. Fig. 15(b and c) are histograms of the positions for each coordinate. The standard deviation in held position is $\sigma_{hp} = $ 6 (4) nm in the directions perpendicular (parallel) to the wire axis. We perform the same

measurement using a silver nanowire that is adhered to the surface to determine the precision of the tracking algorithm. We determine the uncertainty in tracking the wire position to be $\sigma_{tp} = 3$ (2) nm in the perpendicular (parallel) directions. The positioning precision is calculated by subtracting tracking uncertainty from the held position precision using $\sigma_p = \sqrt{\sigma_{hp}^2 - \sigma_{tp}^2}$, which yields $\sigma_p = 5$ (3) nm perpendicular (parallel) to the wire.

4.5   Rotating and orienting nanoparticles with pivots

In addition to the centroid position of a nanowire, we also need to control its orientation. Optical[178] and magnetic[179] fields can rotate nanostructures to desired angles, but the applied torque depends on the nanostructure's polarizability or magnetization, respectively. Flow control can rotate nanostructures independently of their material properties by taking advantage of shear flows.[173] However, this type of manipulation requires a more complex control algorithm and has only been demonstrated previously for wires with lengths exceeding 10 μm. Here we use flow control in combination with immobilized nanostructures that serve as pivots for orienting wires. This approach takes advantage of the confinement of nanostructures to a thin fluid layer near the device surface (Fig. 14(b)). Our method requires only a simple control algorithm, and can control the orientation of wires as short as 1 μm.
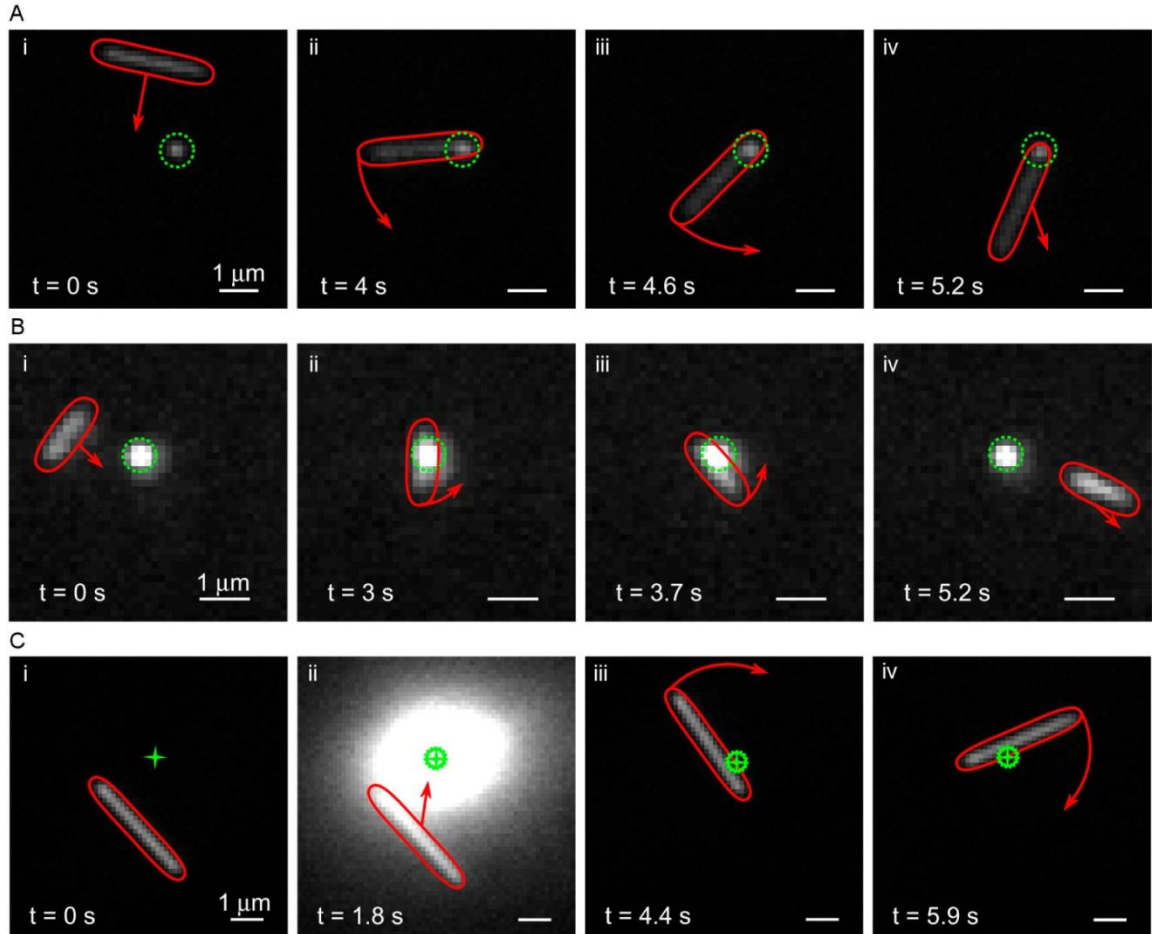
Fig. 16 Orienting silver nanowires with pivots. (a) Time-stamped images illustrating rotation of a silver nanowire using a nanoscale pivot. **(b)** Time-stamped images illustrating rotation of a gold nanowire using a nanoscale pivot. **(c)** Time-stamped images illustrating rotation of a silver nanowire using a polymerized pivot created by UV exposure. The green crosshairs denote the location of the UV focal spot. In all figures, the arrows denote direction of nanostructure translation and rotation and green circles indicate the location of the pivot.

Nanostructures are first deposited onto the device surface and they immobilize before the channels are filled with fluid. Fig. 16 shows several image sequences that demonstrate the rotation of a gold or silver nanowire using an immobilized pivot. We rotate the wire by pressing one of its ends against the pivot and applying a perpendicular flow. In row A, a silver nanowire (3 μm long) rotates about a pivot composed of a silver nanoparticle (indicated by a dashed circle). Row B shows rotation of a 1 μm long gold nanowire about a similar pivot. We can also create pivots as needed with UV

polymerization, as shown in row C. We create a pivot using a 1.5 s exposure of a 375 nm laser (25 W/cm^2) focused to a target location (shown by the green crosshairs), which polymerizes a region of fluid on the surface that is invisible to the camera (panels iv,v). The silver nanowire rotates around this fabricated pivot as shown in frames iii and iv. These polymer pivots can be created anywhere within the device to aid in the manipulation of nanostructures.
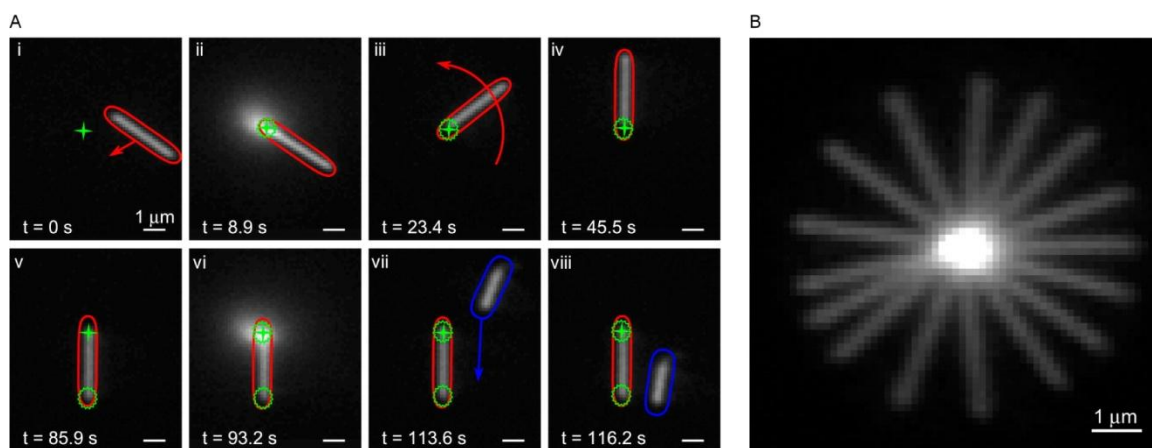
Fig. 17 Orienting a silver nanowire after immobilizing one of its ends. (a) (i) The nanowire is positioned so that its end is at the focus (green crosshair) of the UV laser. (ii) Local UV exposure immobilizes one end of the nanowire. (iii,iv) The nanowire is rotated about the immobilized end and held at a vertical orientation. (v) The stage is translated so that the UV focus is at the free end of the nanowire. (vi) A second UV exposure immobilizes the second end of the nanowire. (vii,viii) Subsequent actuation of fluid flow confirms that the nanowire is immobilized, as is seen from the motion of a second silver nanowire (blue). **(b)** Composite image from several frames of a silver nanowire rotating 360° about its immobilized end.

We can directly rotate a nanowire without using obstructions by partially immobilizing one of its ends. Fig. 17(a) is a sequence of images that demonstrate this process. First, we position one end of a silver nanowire to the location of the UV focal point (indicated by the green crosshair). A 0.5 s UV exposure (intensity of 90 mW/cm^2) loosely affixes the nanowire to the surface by partially polymerizing the surrounding fluid. The affixed end acts as a pivot about which the nanowire rotates. A subsequent UV

exposure at the second wire end permanently immobilizes the wire in place at the desired

orientation. An affixed end allows for 360° rotation of a wire, as shown in Fig. 17(b).

By affixing the end of the silver nanowire we can achieve precise control of its

orientation using feedback. The angle of the silver nanowire is measured by performing a

least-squares fit of the image to a line.[173] This information is fed back to the controller

that continually adjusts flow to hold the wire orientation at the desired angle. We quantify

the orientational precision by monitoring the angle of a wire held by feedback for 1 min.

The angular standard deviation, correcting for fluctuations in the tracking algorithm, was

measured to be $\sigma_\theta = 0.4°$.
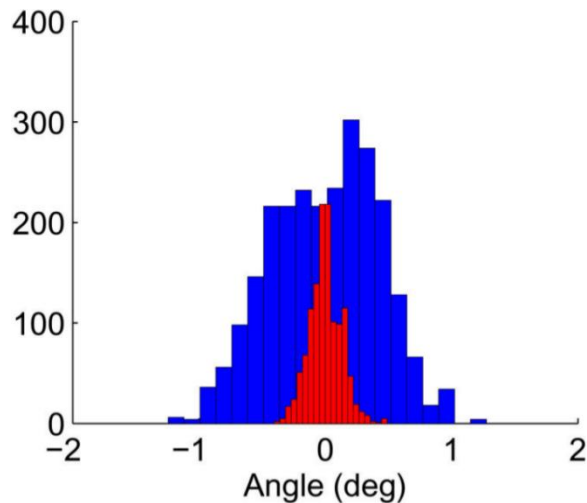
Fig. 18 Histograms comparing the measured angle of a silver nanowire that is immobilized on a surface (red) with one that is oriented by flow control (blue).

Affixing one end of a silver nanowire to the surface with polymer provides

precise control of the nanowire's orientation. We quantify orientational precision by

monitoring the angle of a wire held by feedback for 1 minute. Fig. 18 plots histograms of

the measured angles for the held wire (blue) compared to the measured angle for an

immobile silver nanowire (red). We calculate the standard deviation in held angle, $\sigma_{h\theta} =$

0.42°. The standard deviation of the immobilized nanowire's angle provides an estimate for the uncertainty in tracking the wire's angle, determined to be $\sigma_{t\theta} = 0.13°$. We subtract the tracking uncertainty from the held angle precision to calculate the 2 orientation precision given by $\sigma_\theta = \sqrt{\sigma_{h\theta}^2 - \sigma_{t\theta}^2}$, which is calculated to be 0.40°.

To determine the precision with which we can immobilize, we repeat the full procedure illustrated in Fig. 17(a) for 15 silver nanowires. For each nanowire, we immobilize one end, rotate the wire to N–S orientation, and then immobilize the second end. We measure the final orientation of all 15 wires and calculate the differences in angle from the desired orientation. The measured differences have a standard deviation of 0.53°. This standard deviation is close to the measured precision of the control algorithm, which suggests that the immobilization step contributes only a small additional error.

4.6 Manipulating nanoparticles with barriers and guides

Immobilized nanowires can further enhance manipulation by acting as barriers to separate, combine, and orient moving nanostructures. Fig. 19 shows how an immobilized silver nanowire can be used to separate and combine quantum dots. The silver nanowire and quantum dots are imaged simultaneously using a combination of white light and 532 nm excitation. Fig. 19(a) shows two quantum dots being separated using an immobilized silver nanowire (delineated in green) as a barrier. The figure shows a sequence of time-stamped images, along with an illustration of the approach. Separation uses the end of the nanowire to wedge one quantum dot (circled in blue) apart from the second (circled in red). Fig. 19(b) shows the reverse process, in which we combine two quantum dots by pushing them against a common nanowire barrier. Once combined, the

quantum dots can be steered together and positioned to a desired location. These same

approaches can be applied to other types of nanostructures.
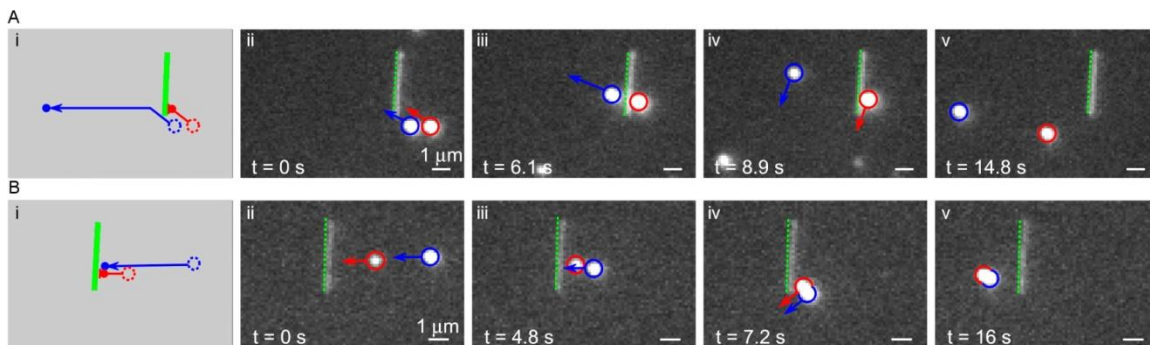
Fig. 19 Using a nanowire to separate or join quantum dot pairs. (a) (i) Quantum dot separation (blue from red) using a silver nanowire barrier. (ii-v) Time-stamped images of the separation. **(b)** (i) Combining two quantum dots (blue to red) using a silver nanowire barrier. (ii-v) Time-stamped images. In all panels the arrows denote direction of particle motion and green delineates the location of the barrier.
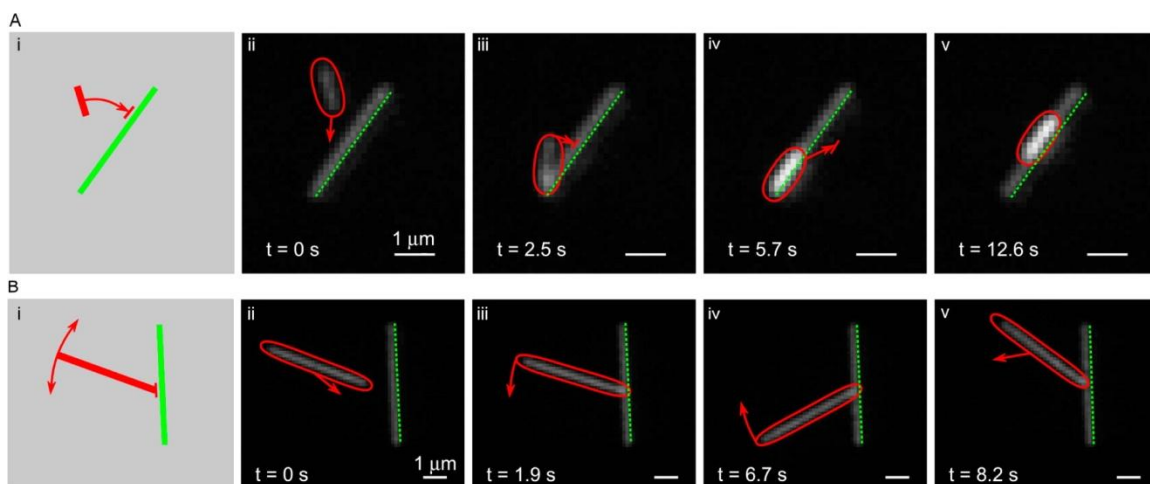
Fig. 20 Aligning free-floating nanowires with immobilized nanowires. (a) (i) Alignment of a gold nanowire to an immobilized silver nanowire guide. (ii-v) Time-stamped images of the alignment process. **(b)** (i) Silver nanowire rotation using a second immobilized silver nanowire barrier. (ii-v) Time-stamped images of the rotation. In all panels, the arrows denote direction of fluid flow and object rotation and green delineates the location of the immobilized nanowire.

Fig. 20 demonstrates nanostructure orientation using silver nanowire guides and

barriers. In Fig. 20(a), flow is used to align a gold nanowire with a silver nanowire. The

silver nanowire serves as a guide to orient the gold nanowire in the parallel direction.

Once together, the silver nanowire guides the gold nanowire along its surface (panels iv–

v). Immobilized nanowires can also orient mobile nanowires at various relative angles. Fig. 20(b) demonstrates orientation of one silver nanowire using a second immobilized silver nanowire as a barrier. We create a component of the fluid flow normal to the barrier to exert a force that holds one end of the mobile silver nanowire in place by static friction. A parallel flow component rotates it in either direction. Static friction provides ample footing for rotation angles as large as 40° to normal.

4.7   Assembling nanoparticles

As a final demonstration, we use a combination of the techniques from our toolbox to fabricate nanoassemblies from individual silver nanowires, as shown in Fig. 21. For each structure, we first immobilize a nanowire either along the E–W direction (panels A and D) or N–S direction (panels B, C, and E) using the technique outlined by Fig. 17(a). We assemble the subsequent nanowires in panels A–D by first coarsely orienting and placing them near the correct location (the technique in Fig. 16, but using the immobilized nanowire ends as pivots). We then achieve finer orientation by anchoring one end of the nanowire and rotating the other. Once oriented, we immobilize the second nanowire end. The nanoassembly pictured in Fig. 21(E) uses the technique shown in Fig. 20(b) to orient a second nanowire perpendicular to the first. We orient subsequent nanowires using the "v"-shaped footholds created by the first two and immobilize them with UV. Additionally, when required, we use immobilized barriers to separate unwanted nanowires from a desired nanowire (using the technique described in Fig. 19(a)) to perform assembly with these isolated nanostructures.
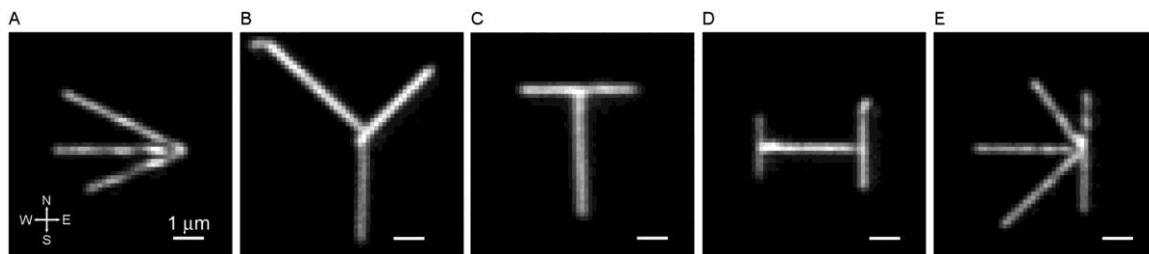
Fig. 21 Optical images of silver nanowire nanoassemblies constructed using different combinations of techniques from our fabrication toolbox.

4.8   Summary

In this chapter, we developed a microfluidic toolbox for constructing complex nanostructures on chip with nanoscale accuracy. Nanoparticles are suspended in a fluid containing a photoresist. Electrokinetic tweezers position single nanoparticles on the flat glass bottom of a microfluidic device. Nanoparticles are immobilized in polymer when the local photoresist is exposed to UV. Silver nanowires are oriented and arranged into nanostructures by pivoting them around polymerized anchors, and can be used to guide light in the form of surface plasmons.[162]

Assembly of nanostructures with electrokinetic tweezers could be used to construct plasmonic circuits and nanosystems. Plasmonic nanowires guide light in the form of surface plasmons[162] and can be assembled into plasmonic circuits for subwavelength interferometers[158] and resonators.[180] Integrating single emitters, such as QDs,[163] with nanowires yields single photon transistors for quantum computation[161] and efficient single photon sources for quantum communication.[181] Electrokinetic tweezers can position several objects at the same time using fluid forces that do not depend on material properties,[160] so this toolbox could be used to efficiently assemble large,

complex nanoparticle systems such as lumped element nanoelectronics[157] and user-defined metamaterials.[160]

Chapter 5

Nanoscale Imaging and Spontaneous Emission Control

5.1   Background

Controlled interactions between nano-emitters and plasmonic nanostructures are important for a broad range of applications in photonics and quantum optics. Plasmonic nanostructures localize electromagnetic fields to nanometer dimensions in the form of surface plasmon polariton (SPP) waves. Accurate placement of nano-emitters in the high-field regions of SPP modes can improve the efficiency and directionality of light emitters,[182,183] provide large nonlinear optical effects at low light levels,[161,184,185] enhance sensing capabilities[186,187] and enable the development of lump-element nanophotonic circuits[157] as well as quantum optical circuits for quantum networking.[161,181] Nano-emitters can also serve as nearly ideal localized excitation sources that can be used to probe electromagnetic properties of plasmonic nanostructures, such as the local density of optical states (LDOS), with high spatial resolution.[188]

A variety of methods have been applied for sub-wavelength probing of plasmonic structures. Near-field scanning optical microscopy utilizes a tapered tip to probe the LDOS.[189–194] This tapered probe, however, can add unwanted distortion to the image.[188,195,196] Other imaging techniques, such as electron energy-loss spectroscopy[197] and cathodoluminescence imaging spectroscopy,[198,199] enable the study of plasmonic mode structures with nanometric precision by using a tightly focused electron beam.

However, these techniques typically require high vacuum and an electron beam that has been accelerated at high voltage, which limit their applicability.

An ideal probe for nanoscale electromagnetic imaging is a single, isolated, point-like dipole emitter, which provides high spatial resolution with minimal distortion of the LDOS.[188] Additionally, the strong back-action of the plasmonic nanostructure on the emitter can enhance or suppress spontaneous emission. This back-action provides an effective method for performing spontaneous emission control,[163,200] forming the basis for novel light sources[183] and quantum circuits.[161] Methods that incorporate either single emitters[201,202] or ensembles of emitters[200,203] on a scanning tapered probe have been demonstrated for both near-field imaging and spontaneous emission control, but these techniques have so far been limited to an imaging resolution of about 100 nm. Mechanical dragging of diamond nanocrystals in the vicinity of plasmonic structures using scanning-probe manipulators has also been demonstrated,[204,205] but to date this method has only provided sparse sampling of the electromagnetic mode with too few data points to reconstruct an accurate image. Three-dimensional manipulation of 75 nm diamond nanocrystals by optical trapping has also been reported recently and used to image the LDOS of dielectric waveguides,[206] but the extension of this approach to plasmonic structures is challenging because the field typically decays on a length scale that is on the order of the size of the nanocrystal. Random diffusion of fluorescent molecules has also been used to image plasmonic hot spots, achieving spatial imaging accuracy as fine as 1.2 nm.[207] However, this procedure is entirely stochastic and cannot be used to probe a desired location or target on demand.

Semiconductor quantum dots (QDs) are ideal nano-emitters for local probing and excitation of plasmonic nanostructures. QDs are bright and highly efficient room-temperature light sources with a stable, narrow and tunable emission spectrum.[208] They also exhibit single-photon emission, making them potential candidates for quantum devices.[209] Additionally, owing to their nanometric size, QDs can act as sensitive probes for studying the electromagnetic properties of plasmonic nanostructures with high spatial accuracy. However, the application of QDs as nanoscale probes has been challenging. Their small size makes them difficult to manipulate using standard approaches such as optical trapping.[41] Although optical trapping of single QDs has been demonstrated,[166] the spatial accuracy of this trapping procedure has not been reported and the positioning accuracy that can be achieved with this approach remains unclear. Additionally, optical trapping forces are not selective, which can result in many particles getting caught in a single trap over a short timescale. Alternate methods that utilize tapered probes with single QDs attached to the tip[210] or, conversely, scan an attached sample over a single QD immobilized on a surface,[211] have been reported. However, these approaches have been largely limited by QD blinking and bleaching, which significantly distort the acquired image.

In this chapter, we demonstrate that a single QD can be used as a nanoprobe for imaging plasmonic nanostructures and for spontaneous emission control with high spatial accuracy. Specifically, we use a single QD to image the LDOS of a silver nanowire (AgNW). The QD is deterministically positioned at desired locations adjacent to the AgNW by actuating flow in a microfluidic device through electroosmosis,[44] thereby moving the QD via viscous drag.[117,154] Using this approach, we image the LDOS with a

spatial accuracy as fine as 12 nm. Furthermore, we utilize the back-action of the AgNW on the QD to perform spatially resolved spontaneous emission control with nanoscale accuracy. We demonstrate control of the QD lifetime by placing it in regions with different magnitudes of the LDOS. The high spatial accuracy of our approach reveals oscillations in the QD spontaneous emission rate, as it is positioned along the wire axis. These oscillations are the signature of direct coupling to surface plasmon modes induced by interference between counter-propagating surface plasmon waves. The ability to control light–matter interactions at these length scales is crucial for optimizing interactions between single emitters and surface plasmons, and has an important role in the study of quantum optics in plasmonic structures as well as in the development of nanoscale quantum devices.[161]
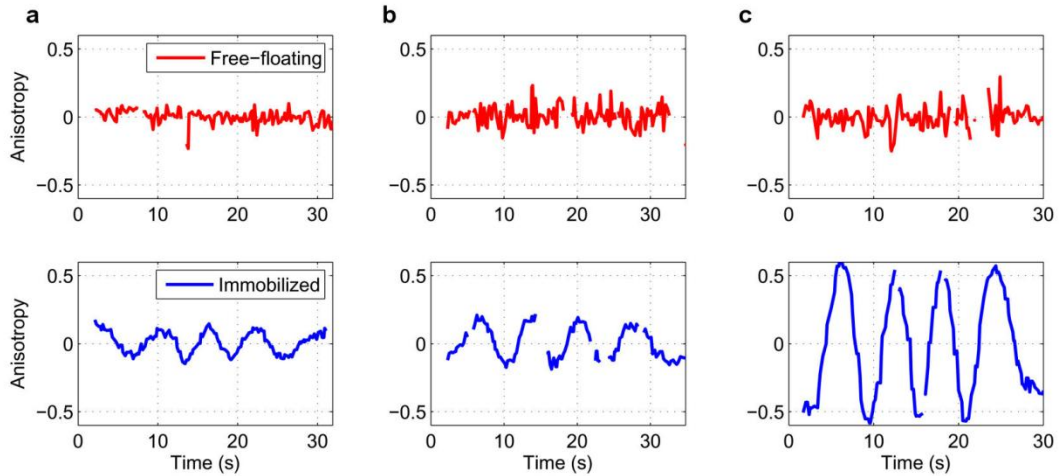
Fig. 22 QD Polarization in channel. The emission anisotropy of three pairs of QDs (a-c) measured as a function of polarization (which was rotated in time). Each pair consisted of a free-floating (red) and an immobilized (blue) QD. The emission polarizations for each pair were characterized simultaneously using a setup where the emission was sent through a half-wave plate and then split into vertical (V) and horizontal (H) polarization by a calcite beam displacer. Plotted here is the measured emission anisotropy, $(I_V - I_H)/(I_V + I_H)$, for each QD as the emission polarization is rotated with the half-wave plate. The immobilized QDs demonstrate a clear polarization dependence, which is expected,[213] however the free-floating QDs appear largely unpolarized. We attribute this lack of polarization for the colloidally suspended QDs to rotational Brownian motion, which causes polarization effects to be averaged out if the data acquisition time exceeds the free rotation rate. As a result, our free floating probe QDs will behave as effectively isotropic emitters.

5.2 Imaging approach

Our imaging approach relies on the strong electromagnetic interactions between the QD and the SPP mode of the wire. When a QD is positioned near an AgNW, energy from the photoexcited QD is transferred to the wire's SPP mode through an electric dipole interaction.[163] The rate of energy decay of an isotropic emitter into the guided SPP mode of the AgNW is given by Fermi's Golden Rule

$$\gamma_{nw} = 2\pi\mu^2 \langle |E(r,\omega)|^2 \rangle D(\omega), \qquad (13)$$

where $D(\omega)$ is the spectral density of electromagnetic modes, $E(r,\omega)$ is the electric field operator for the AgNW mode and μ is the transition dipole moment of the emitter.[212] Although QDs can exhibit polarized light emission and are therefore not completely isotropic,[213] rotational Brownian motion in the fluid averages out orientational effects on a timescale that is much faster than the data integration time (Fig. 22), enabling the QD to behave as an effectively isotropic emitter. The spontaneous emission rate is often expressed in terms of the LDOS defined as:[214]

$$\rho(\omega) = \frac{\langle |E(r,\omega)|^2 \rangle D(\omega)}{4\pi k^2}, \qquad (14)$$

where $k = \omega/c$. Thus, γ_{nw} is proportional to the LDOS, and provides a direct measure of the local field intensity of the AgNW mode at the location of the emitter. In our experiment, this rate is measured in two independent ways: by monitoring the radiated light intensity from the wire end and by directly measuring the QD lifetime as a function

of position. These two observables provide mutually complementary approaches for studying the electromagnetic properties of the wire.

5.3   Electrokinetic tweezing of QD nanoprobes

5.3.1   Microfluidic device and reagents

An optical image of the microfluidic device used to position QD nanoprobes around AgNWs is shown in Fig. 23(a). Two perpendicular microfluidic channels intersect at a central control region (dashed circle), where QDs are imaged and manipulated. Fig. 23(b) illustrates the probing procedure for an AgNW. AgNWs with an average diameter of 100 nm and an average length of 4 μm (scanning electron microscopy image in Fig. 23(b) inset) are deposited on the polydimethylsiloxane (PDMS) surface of the control region. The channels are filled with fluid containing QDs that are confined to a thin sheath along the surface by the fluid chemistry.[154] Within this sheath, single QDs are selected and scanned along a trajectory that samples the LDOS of AgNWs at a desired set of locations using flow control. The deposited AgNW acts as an obstacle for the QDs, indicating that the QDs are constrained to be within 100 nm of the surface (the diameter of the AgNW). The QD fluorescence signal is collected using a confocal micro-photoluminescence system,[117,154] and 25% of the emission is sent to a CCD camera for tracking. The remaining 75% of the emission is sent to an avalanche photodiode (APD) for performing lifetime measurements. Each detection event from the APD is saved with a time stamp that is synchronized to the camera frame acquisition rate.
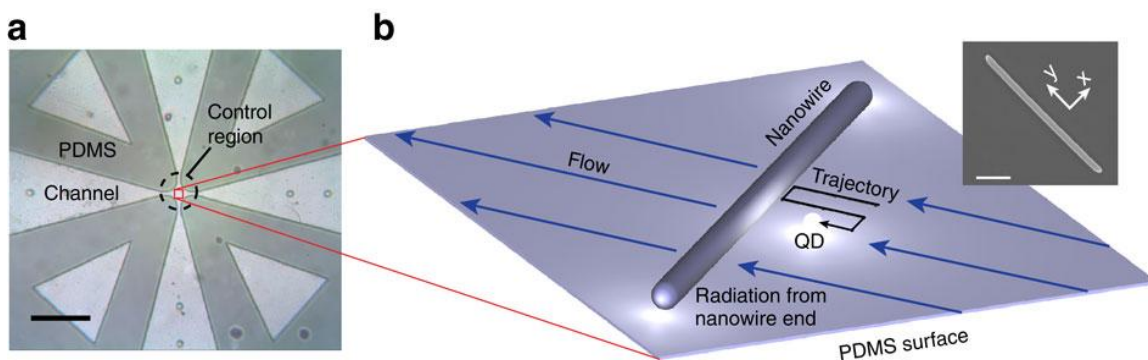
Fig. 23 Near-field probing with a single QD. (a) Optical image of the microfluidic crossed-channel device. Flow in the centre control region (dashed circle) is manipulated in two dimensions by four external electrodes (not shown). Scale bar, 500 μm. **(b)** Schematic of the positioning and imaging technique. A single QD is driven along a trajectory close to the wire by flow control. The coupling between the QD and AgNW is measured either by the radiated intensity from the wire ends or by QD lifetime measurements. The inset shows a scanning electron microscopy image of a typical AgNW used in our experiments (scale bar, 1 μm). The x-y coordinate system is defined relative to the orientation of the AgNW, as illustrated in the inset.

The microfluidic device was composed of a molded PDMS cross pattern placed on top of a glass coverslip. The resulting channel was 5 μm in height with a control region that was ~100 μm in diameter. The QDs were excited simultaneously by a 532-nm continuous wave laser at an intensity of 250 W cm^{-2} and a 405-nm pulsed laser with a 10-MHz repetition rate at 35 W cm^{-2}. A fraction (25%) of the QD emission was imaged using an EMCCD camera (Hamamatsu C9100-13) operating at 10 Hz frame rate, while the remaining signal was focused onto an APD (PerkinElmer SPCM-AQR) for time-resolved lifetime measurements. Data were analyzed using a time correlation single-photon-counting module (PicoQuant PicoHarp300) that synchronizes photon events with camera frames.

AgNWs were synthesized by reducing AgNO$_3$ with ethylene glycol (EG).[177] In a typical synthesis, 5 ml of EG (Fisher Scientific) was placed in a 50-ml round-bottom flask equipped with a condenser, a thermometer and a magnetic stirring bar. After the EG was heated to 160 °C in an oil bath, 0.5 ml of PtCl$_2$ (Aldrich, 1.5×10^{-4} M in EG)

was injected into the solution to synthesize 1–5 nm precursor nanoparticles. After 4 min, 2.5 ml of AgNO$_3$ (Aldrich, 0.12 M in EG) and 5 ml of poly(vinyl pyrrolidone), (Mw ≈ 40,000, City Chemical LLC, 0.36 M in EG) were added simultaneously over 6 min with an accompanying color change from yellow to yellowish grey. When the AgNO$_3$ had been completely reduced by EG for 60 min, the solution was cooled to room temperature. To remove the remaining EG, poly(vinyl pyrrolidone) and silver nanoparticles, the solution was diluted with ethanol and centrifuged at 2,000 RPM for 15 min. After repeating several times until the supernatant became transparent, the solution was redispersed in H$_2$O. The resulting bicrystalline[55] AgNWs were typically 100–120 nm in diameter and 3–10 μm in length, as determined by scanning electron microscopy.

The control fluid was composed of 45–48% by volume ethoxylated-15 trimethylolpropane triacrylate resin (SR-9035, Sartomer), 1.25–1.4 wt% rheology modifier (Acrysol RM-825, Rohm and Haas Co.),[174] 0.15–0.3% of a zwitterionic betaine surfactant[175] and CdSe/ZnS core-shell QDs (Ocean NanoTech, Carboxylic Acid, 620 nm) in deionized water. The triacrylate resin causes the fluid sheath to form. The surfactant was introduced to improve electroosmotic actuation on the PDMS surface, while the rheology modifier was used to reduce Brownian motion and inhibit unwanted adhesion of the QDs to surfaces.

5.3.2   Positioning QDs with nanoscale accuracy

QD positions are tracked with sub-wavelength accuracy by fitting the imaged diffraction spot to a Gaussian point-spread function. The spatial accuracy of the tracking

algorithm is limited by system vision noise, which includes a combination of camera read noise, multiplication noise and shot noise. We determine the tracking accuracy by monitoring an immobilized QD on a glass surface for 1 min. The measured QD positions are plotted as red data in Fig. 24(a). The red bars in Fig. 24(b) plot a histogram of the measured QD position along x and y coordinates respectively. The solid yellow line represents a Gaussian fit where the standard deviation (SD) is used to determine a tracking accuracy of $\sigma_{tr} = 12 \pm 1$ (11 ± 1) nm along the x (y) directions.
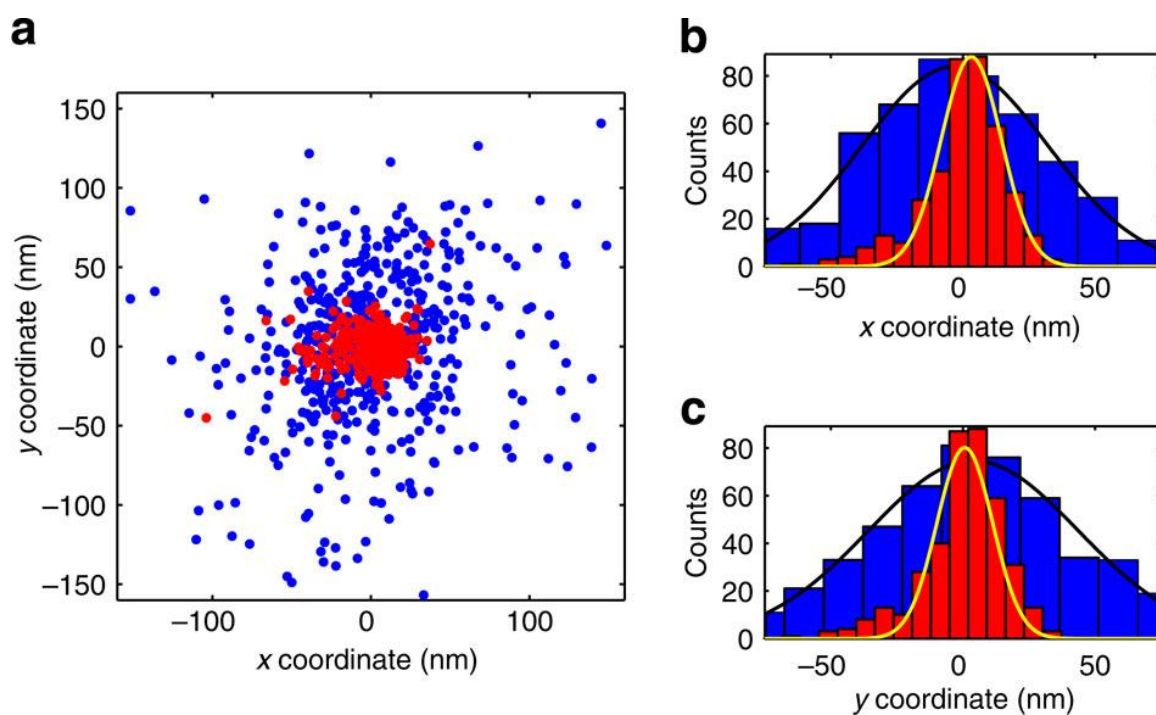
Fig. 24 QD tracking and positioning accuracy. **(a)** Scatter plots of the measured positions of a QD over the course of 1 min. Red data points correspond to a QD that is immobilized, while blue data points correspond to a QD that is held in place by flow control. **(b,c)** Histograms of the x and y coordinate corresponding to data from panel a. Red bars are the histogram for an immobilized QD, while blue bars are the histogram for a positioned QD. The yellow solid line is a Gaussian fit for an immobilized QD showing a measure SD of 12 ± 1 (11 ± 1) nm along the x (y) coordinate. The black solid line is a Gaussian fit for the positioned QD with SD of 36 ± 2 (40 ± 2) nm for the x (y) coordinate.

Nanoscale positioning accuracy is achieved by employing vision-based feedback control that creates corrective flows to position the QD at a desired location. The

positioning accuracy is measured by monitoring a QD that is held in place by flow control for 1 min. The measured QD positions are plotted as blue data points in Fig. 24(a). The blue bars in Fig. 24(b) are a histogram of these measurements, while the black solid line is a Gaussian fit where the SD determines a positioning accuracy of $\sigma_P = 34 \pm 3$ (39 ± 3) nm along the x (y) directions. These numbers were corrected for noise in the tracking algorithm using the relation $\sigma_P = \sqrt{\sigma^2 - \sigma_{tr}^2}$, where σ is the total measured position fluctuations. The high positioning accuracy ensures that we can deterministically probe the wire mode at a desired location on demand with nanometric accuracy. It is important to note that the positioning accuracy does not limit the spatial imaging accuracy of the system, as the position of the QD is known to a higher accuracy than it can be controlled.

Fig. 25(a–c) shows a series of images of a single QD being moved progressively closer to an AgNW. When the QD is in close proximity to the wire, light radiates from the wire ends (Fig. 25(c)). This radiation arises from direct dipolar coupling of the QD excitation to the waveguided SPP mode. The extraction efficiency of the QD excitation into the AgNW mode is given by $\eta_{ex} = \gamma_{NW}/\gamma$, where γ is the total decay rate of the QD due to all radiative and non-radiative decay channels and γ_{NW} is defined in equation 13. In the limit in which γ is dominated by free-space modes, the efficiency is proportional to the LDOS at the location of the emitter. Therefore, by simultaneously monitoring the QD position and the radiated intensity from the wire end, we can construct an image of the LDOS. In addition, we measure the LDOS by directly measuring the QD radiative lifetime.[200] Such direct lifetime measurements have the advantage that they are independent of sample geometry, as they do not rely on monitoring the AgNW end

radiation. Thus, in contrast to measurements that monitor the distal end of a wire, lifetime imaging can be applied to objects that are sub-wavelength in all three dimensions, such as metallic nanospheres and nanorods.
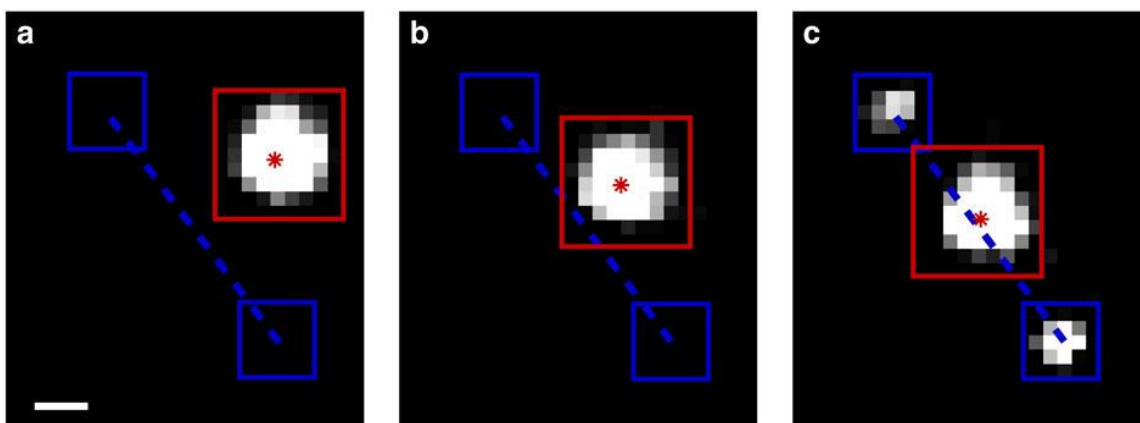
Fig. 25 Coupling a QD to an AgNW. (a-c) A series of images showing coupling of the QD to the AgNW as the QD is moved closer to the wire. The scale bar is 500 nm and intensities are plotted on a logarithmic scale. The red and blue boxes show the image integration region used to calculate the radiation intensities and positions of the QD and the wire ends, respectively. The measured location of the QD is labeled with a red star and the axis of the AgNW is labeled with a blue dashed line.
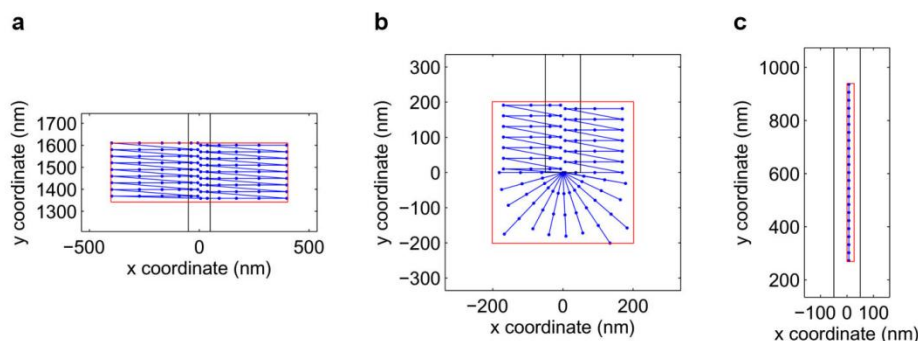
Fig. 26 Scanning Trajectories. (a) Mid-wire scanning trajectory corresponding to Fig. 27. **(b)** A trajectory scanning the wire tip corresponding to Fig. 30. **(c)** A trajectory scanning the wire along the side corresponding to Fig. 32. Blue points connected with lines correspond to the trajectory points, connected in order of scanning. During the experiment, flow is applied to position the QD to the desired trajectory point for two seconds before moving on to the next point. Red boxes define the scanning regions. Black lines designate the physical extent of the wire. Some points along the trajectory lie inside the wire or on the opposite side of the wire, however, since the wire acts as an obstacle the QD cannot generally reach these points and instead is forced against the wire to ensure data is collected as close as possible to the surface. Additionally, the trajectory points are more densely spaced closer to the wire in order to ensure probing of the near-field region.

QD probing was performed at various locations along the middle and end of the AgNW. The QD trajectories, as shown in Fig. 26, were selected to maximize data sampling near the wire surface. A significant challenge of probing with QDs is that they blink,[215] which leads to emission intensity fluctuations that complicate the interpretation of the radiated intensity from the wire end. Our imaging approach offers a convenient solution to this problem because it enables the simultaneous measurement of the intensity radiated both from the wire end and directly from the QD. The direct radiation from the QD is used to normalize for QD blinking and local field enhancement of the pump. The QD emission and the AgNW-radiated intensity are measured by summing the pixels within their respective windows (Fig. 25(a–c)). We define the normalized coupled intensity $\bar{I}$ as:

$$\bar{I}(x,y) = \frac{\sum_{n,m}\left(I_{n,m}^{NW} - I^{BKG}\right)}{\sum_{p,q}\left(I_{p,q}^{QD} - I^{BKG}\right)},$$

(15)

where $I_{n,m}^{NW}$ and $I_{p,q}^{QD}$ are the intensities of the $(n,m)^{\text{th}}$ and $(p,q)^{\text{th}}$ pixels within the AgNW and QD windows respectively, while I^{BKG} is the average pixel background intensity. The background level is calculated by averaging pixels sufficiently far away from the AgNW and the QD. The value of $\bar{I}$ is proportional to the coupling efficiency η, and thus to the LDOS of the nanowire.

5.4   Probing the side of an AgNW

Fig. 27(a) is a scatter plot of $\bar{I}$ as a function of QD position when the QD was positioned near the midpoint of the AgNW. The dashed lines represent the location of the

AgNW surface which is assumed to be 50 nm from the wire axis (the typical radius of the wires used in this work). The wire orientation and length were determined by tracking the diffraction spots of the radiated light from the wire ends (blue boxes in Fig. 25(c)) using the same algorithm used to track the QD. The data points are plotted relative to the measured wire location with the y-direction aligned along the wire axis and the x-direction corresponding to distance from the wire axis, as indicated in the inset of Fig. 23(b), with the origin placed at the lower end of the wire. We note that different locations along the y coordinate may experience different propagation losses to the wire end, which could cause a small distortion of the image. However, the absorption length of an AgNW was measured to be 4.7 μm (Fig. 28 and Methods), which is much longer than the 200 nm scanning distance. Thus, propagation losses are expected to have only a minimal effect on the data.

Fig. 27(b) shows $\bar{I}$ as a function of radial distance from the wire axis, which is seen to increase as the QD approaches the wire surface. For a cylindrically symmetric AgNW, the evanescent field from the surface is predicted to follow a Bessel-function decay.[216] The data are therefore fit to a function of the form $|\beta K_0(\alpha x)|^2$ where $K_0(\alpha x)$ is the zeroeth-order modified Bessel function, x is the distance from the AgNW axis, and α and β are fitting parameters (calculated from the fit to be $0.006\,\mathrm{nm^{-1}}$ and 0.142, respectively). The solid blue line in Fig. 27(b) is the Bessel-function fit and the red dashed line corresponds to the AgNW evanescent field as calculated using finite-difference time-domain (FDTD) simulation. The FDTD solution was multiplied by a constant to provide the best fit to the data. Both the analytical and numerical solutions show good agreement with the measured LDOS profile.
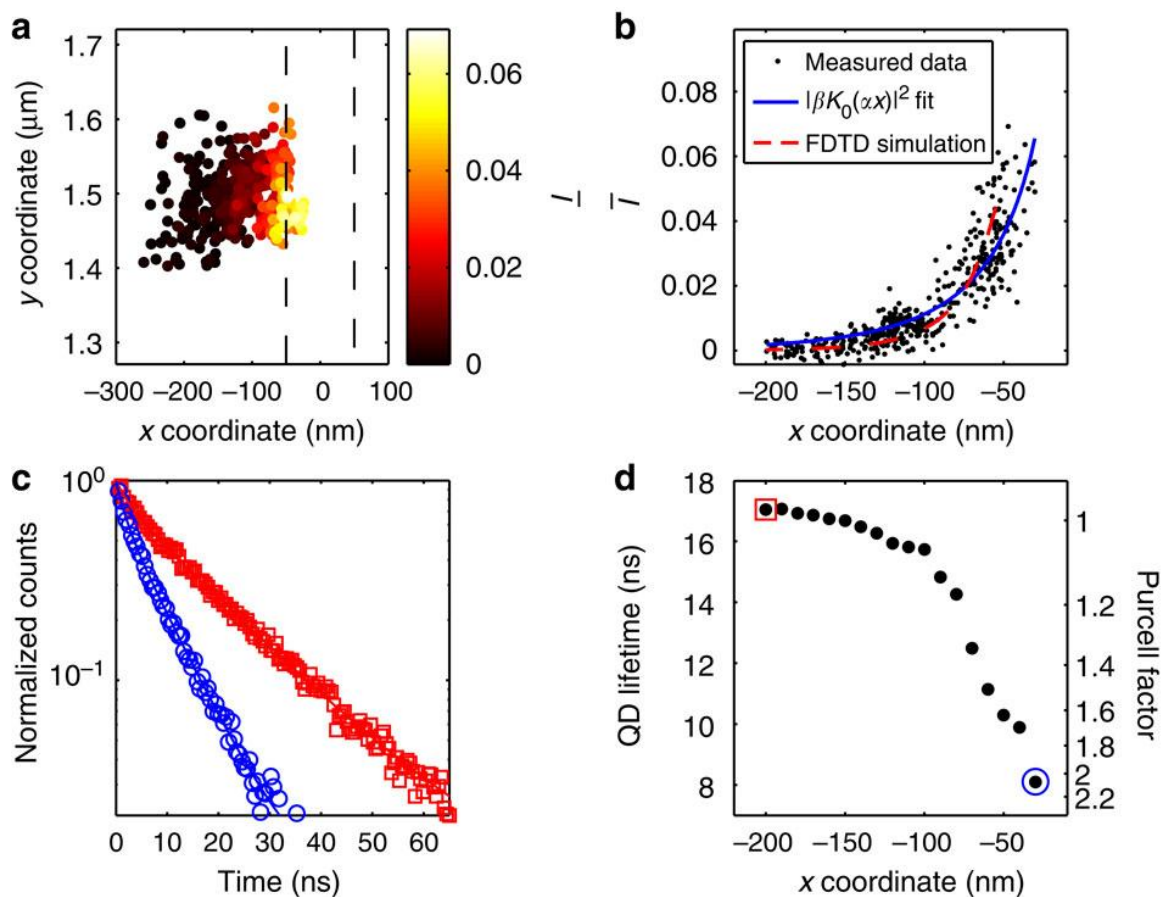
Fig. 27 Probing the LDOS profile near the middle of the AgNW. (a) $\bar{I}$ as a function of position near the middle of the wire. The dashed region indicates the assumed location of the AgNW surface. **(b)** $\bar{I}$ as a function of distance from the wire axis (x coordinate) using data from panel **a**. The blue line indicates the best fit to a modified Bessel function. The red dotted line is an FDTD simulation of the AgNW evanescent field. The simulation result was fit to the data using an overall scaling factor. **(c)** Radiative decay of the QD at 200 nm (red squares) and 30 nm (blue circles) distance from the AgNW axis with lifetime fits of 17 and 8 ns, respectively. **(d)** QD lifetime as a function of x position. The second y-axis denotes the Purcell factor corresponding to the measured lifetimes. Colored markers indicate the data points used for panel **c**.

Simulations were performed using the Lumerical FDTD Solutions software package (http://www.lumerical.com). A 4-μm-long AgNW with 100 nm diameter was simulated surrounded by a background index of 1.4, which corresponds to the index of refraction for PDMS. The QD fluid was assumed to have the same index. Simulations were performed by exciting the AgNW with a transient dipole source, and calculating the field after the dipole excitation had finished.

The spontaneous emission lifetime of the QD was measured using the APD, while the camera simultaneously measured the QD position. Fig. 27(c) shows two time-resolved fluorescence measurements obtained by collecting photon events detected when the QD was at radial distances of 200 ± 12 nm (red squares) and 30 ± 12 nm (blue circles) from the wire axis, respectively. A biexponential fit was used to determine the QD's lifetime,[217] yielding values of 17 and 8 ns for the two distances, respectively. This reduction in lifetime at short distance is consistent with previous measurements of QDs coupled to nanowires.[163]

Fig. 27(d) plots the QD lifetime as a function of position. Each lifetime was calculated by grouping all photon events in which the QD was within a ±12 nm window from the specified radial distance. The positional dependence of the lifetime mirrors the intensity of the emission from the wire end, demonstrating a clear agreement between the two methods, as well as the ability to perform spontaneous emission control by localizing the QD near the wire surface. The color scale in Fig. 27(d) is labeled both in units of raw lifetime (left labels) and Purcell factor (right labels), which is defined as $F_P = \gamma/\gamma_0$, where γ_0 is the emission rate of the QD far from the AgNW and γ is the measured decay rate.

5.5   Propagation loss

In probing along the length of the AgNW, the measured parameter I may experience distortion due to different propagation losses to the wire end. The position dependence of propagation loss can be determined by monitoring the emission intensity from the two ends of the AgNW simultaneously as the QD is moved along the length of

the wire. Here we calculate the propagation length of a typical AgNW used in this work. We describe the radiated intensity from the two AgNW ends as having an exponential dependence according to:

$$I_j = \beta^{(j)} e^{-(x-L/2)/x_l},\qquad(16)$$

where x is the location of the QD between the wire ends, $\beta^{(j)}$ is the radiated intensities from the two AgNW ends labeled $j = 1$ and 2 when the QD is coupled in the middle of the wire, L is the length of the wire, and x_l is the decay length of the SPP mode. In the case where the two facets of the AgNW are completely symmetric, $\beta^{(1)} = \beta^{(2)}$, but in general this is not the case.

The ratio of the measured intensities is therefore:

$$\frac{I_1}{I_2} = \beta e^{-2x/x_l},\qquad(17)$$

where β and x_l are now constant fitting parameters. Fig. 28 plots the average value of I_1/I_2 as a function of position along an AgNW for an experiment where the QD was probed along the length of the wire. We use a fitting function of the form in equation 17 and calculate a propagation length of 4.7 μm, which corresponds well with other published results.[180]
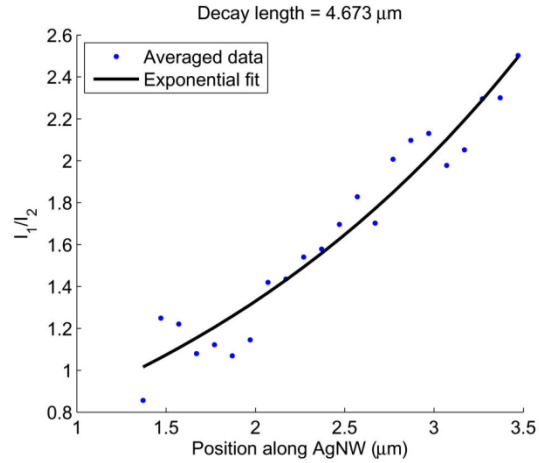
Fig. 28 SPP decay along AgNW length. Ratio of emission intensity measured from both AgNW ends as a function of position along the wire. The black line is an exponential fit.

5.6   Spatial accuracy of measured QD positions

The measurements in Fig. 27(b) can be used to infer the spatial imaging accuracy. This accuracy is determined by calculating the root mean square (RMS) deviation in the measured positions of the QD relative to the position predicted by the Bessel-function fit. The RMS deviation provides an upper bound on the spatial imaging accuracy (Fig. 29). Using this approach, the spatial imaging accuracy was determined to be 12 nm, which is consistent with the 12 ± 1 nm tracking accuracy calculated previously by observing an immobilized QD, indicating that the spatial imaging accuracy is primarily limited by vision noise.

Here we derive a bound on the spatial accuracy of the measured data points. Both the measured data and Bessel-function fits are shown as a function of distance from the wire axis. The red lines indicate the spatial distance of each data point from the predicted value given by the Bessel function fit. Fluctuations in the spatial coordinate of the raw data relative to the Bessel function arises from both position uncertainty due to

measurement error (fluctuations along the horizontal axis) and intensity noise (fluctuations along the vertical axis). Thus,

$$\sigma_d^2 = \sigma_x^2 + S_I \sigma_I^2, \tag{18}$$

where σ_d represents the fluctuations in the distance between the measured position and predicted value (the red lines in Fig. 29(a)), and σ_I represents fluctuations in the measured value of $\bar{I}$ due to effects such as shot noise and camera pixel noise. The spatial imaging accuracy is given by σ_x, which is the uncertainty in the measured value of the QD position. The value $S_I = [\partial d / \partial \bar{I}]^2$ is the sensitivity parameter for the intensity fluctuations, which depends on the slope of the Bessel function at the measured intensity value. We calculate σ_d using the root mean square distance between data points and the Bessel function fit along the position axis. From equation 18 it can be seen that $\sigma_x \leq \sigma_d$. Thus, σ_d provides a worst case estimate of the spatial imaging accuracy.

The inequality will tend to overestimate the imaging accuracy when intensity noise is not negligible. From the Bessel function fit one can see that when the QD is near the nanowire (approximately 50 nm from the surface) the measured intensity is strongly dependent on the position of the QD due to the steep slope of the curve. In this region the value of S_I, which is related to the inverse of the slope, is small and we expect the noise to be dominated by the measurement inaccuracy of the QD position. Further away from the wire where the slope becomes shallow and S_I becomes large, the intensity noise contributes significantly to the measured error. In this region, the bound will overestimate uncertainty of the measured QD position.
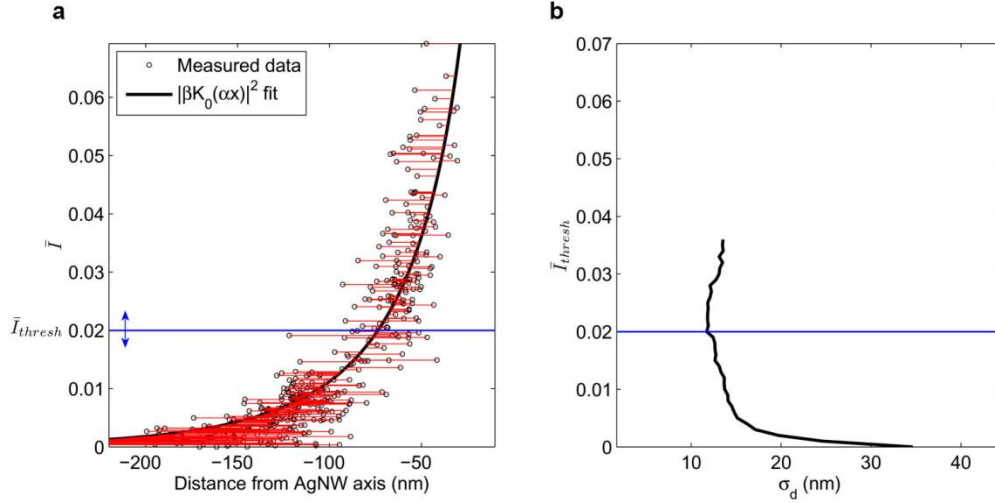
Fig. 29 Spatial Accuracy of Measured QD Positions. (a) Fig. 27(b) with Bessel-function fit. Red lines indicate spatial distance between the measured QD position and position predicted by Bessel-function fit based on the measured intensity. $\bar{I}_{thresh}$ is labeled with a blue line. **(b)** Plot of σ_d as a function of $\bar{I}_{thresh}$. The minimum standard deviation of 12 nm occurs at $\bar{I}_{thresh} = 0.02$ and is represented by the horizontal blue line.

In order to prevent overestimation of the calculated spatial accuracy we introduce an intensity threshold $\bar{I}_{thresh}$ as indicated in Fig. 29(a). All data points whose coupled intensity $\bar{I}$ exceeds this threshold are included in the calculation for σ_d, while data points that lie below the cutoff are rejected. We varied $\bar{I}_{thresh}$ in order to determine when the intensity noise becomes significant in the calculation of σ_d. Fig. 29(b) plots σ_d as a function of $\bar{I}_{thresh}$. The calculated σ_d is largely independent of the intensity threshold for larger values of $\bar{I}_{thresh}$. For $\bar{I}_{thresh} < 0.01$ the bound for the position accuracy begins to rapidly increase because we are including more data points from the region that is highly sensitive to intensity noise. Since each data point in Fig. 29(b) represents an upper bound on the spatial accuracy, we take the minimum value as the tightest upper bound which gives the best estimate. The minimum value is calculated to be 12 nm and is attained at $\bar{I}_{thresh} = 0.02$ (plotted with a horizontal blue line).

5.7   Probing the tip of an AgNW
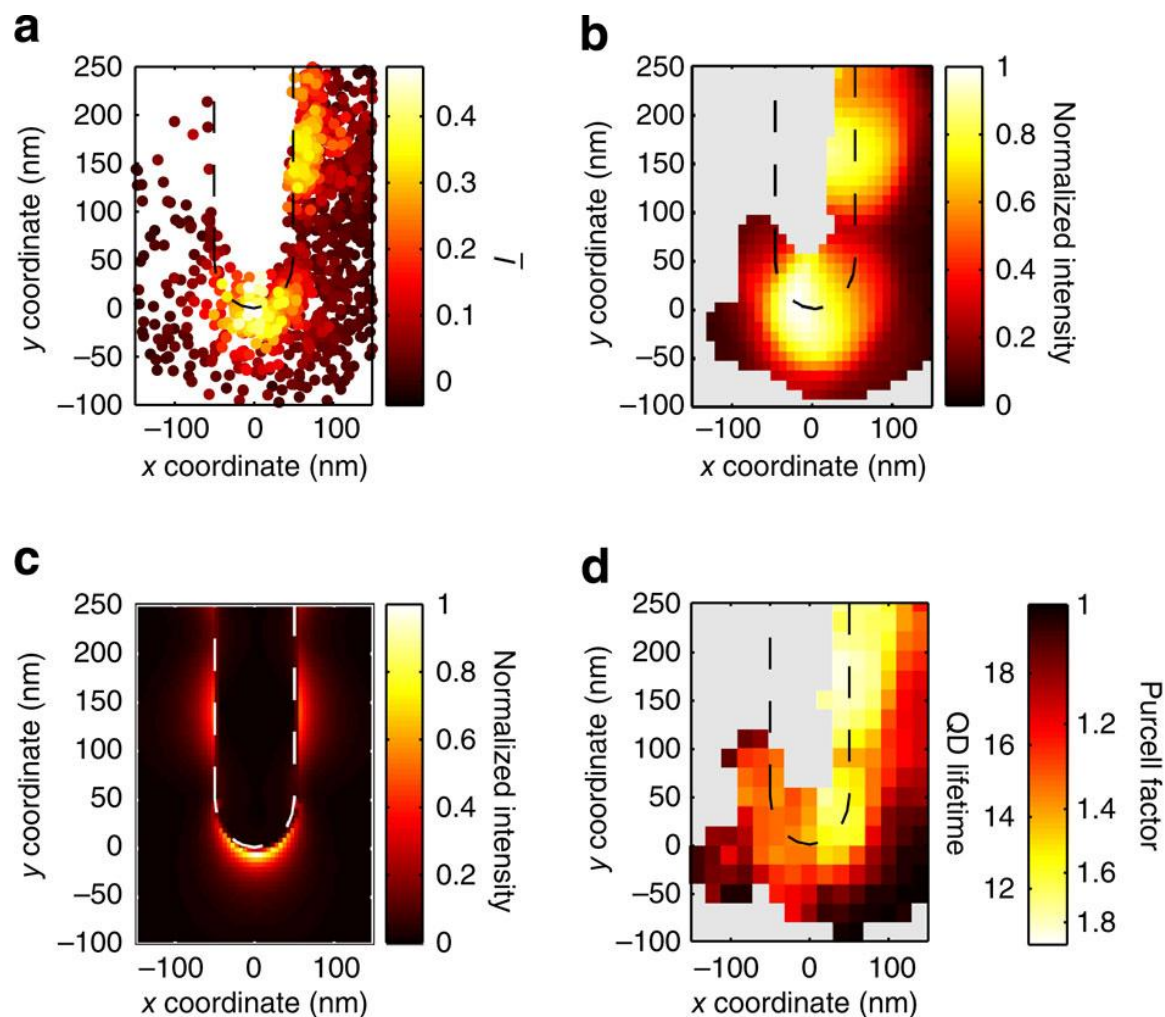
Fig. 30 Probing the tip of an AgNW. (a) Scatter plot of measured positions and intensities near the end of the AgNW. The color of each data point corresponds to $\bar{I}$. The dashed region indicates the location of the AgNW. **(b)** Reconstructed image using a Gaussian-weighted average. The image intensity is normalized by its maximum. **(c)** FDTD simulation of the AgNW mode profile showing an enhancement at the tip (also normalized by its maximum). **(d)** Image of the measured QD lifetime as a function of position. The color scale is labeled with both lifetime and Purcell factor.

Fig. 30(a) is a scatter plot of data recorded when a QD was scanned near one end of the AgNW, while the intensity was monitored at the opposite end. Probing the AgNW tip required several minutes of QD scanning. Over this time span, sample drift can be appreciable, potentially creating image distortion. To account for sample drift, the QD

position was measured relative to the wire end that was tracked throughout the experiment. The ability to correct for drift represents an important practical advantage of this approach, enabling us to acquire images over long periods without distortion.

The raw data presented in Fig. 30(a) can be used to construct an image of the LDOS. The value of each pixel in the image is found by taking a Gaussian-weighted spatial average of the raw data. The Gaussian is centered at the location of the pixel and the SD is set to 33 nm, corresponding to the RMS-combined spatial accuracy of the QD (12 nm) and the tracked AgNW end (30 nm) (Fig. 31). The reduced spatial accuracy at the wire ends is attributed to the fact that their emission is much dimmer than the direct QD emission, as can be seen in Fig. 25(c). The additional error incurred by tracking the wire end is not fundamental to the imaging procedure and could be largely removed by using brighter tracking objects to monitor the drift. The resulting two-dimensional image is shown in Fig. 30(b). Comparison of the measured LDOS profile with the calculated mode obtained from FDTD simulations (Fig. 30(c)) shows good agreement. Fig. 30(d) plots the measured QD lifetime in the region around the AgNW tip. Each lifetime measurement was obtained by combining all photon events for which the QD was within a 33-nm radius of the centre pixel location. The measured lifetime exhibits good agreement with the results obtained from measuring the intensity of the wire end.
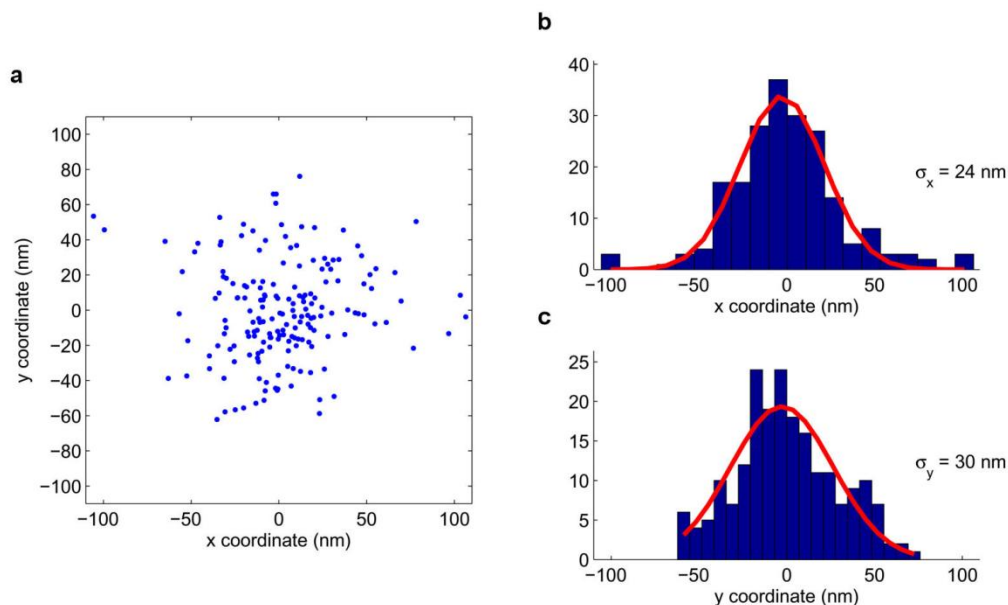
Fig. 31 Spatial accuracy of measured AgNW end positions. (a) Scatter plot of the measured positions of an AgNW end over the course of 1 minute. **(b-c)** Histograms of the x and y positions with Gaussian fits measuring 24 ± 2 and 30 ± 3 nm standard deviations respectively. A single QD is stuck onto an AgNW and the position of the wire end is determined by measuring the center of the diffraction spot of the radiated light and fitting it with a Gaussian point spread function. This light radiated from the wire end is much dimmer than the direct emission from the QD. Thus, the accuracy with which we can track the AgNW is worse than the accuracy with which we can track the QD.

5.8   Spatial oscillation of the LDOS due to interference

In addition to the high field intensity at the wire end, the data in Fig. 30 suggest the presence of an oscillatory mode structure along the sides of the AgNW. To examine this mode structure in more detail, the LDOS was probed along a 500-nm region at one end of a wire. The measurement results for $\bar{I}$ are shown in Fig. 32(a), where position is once again plotted relative to the wire end to compensate for drift. In this measurement, the QD was positioned as closely as possible to the wire surface. Under these conditions, most of the QD positions were measured within the dashed AgNW region. Data points located within this region are attributed to the QD being pushed slightly onto the top of the wire, which does not act as a perfect obstacle.
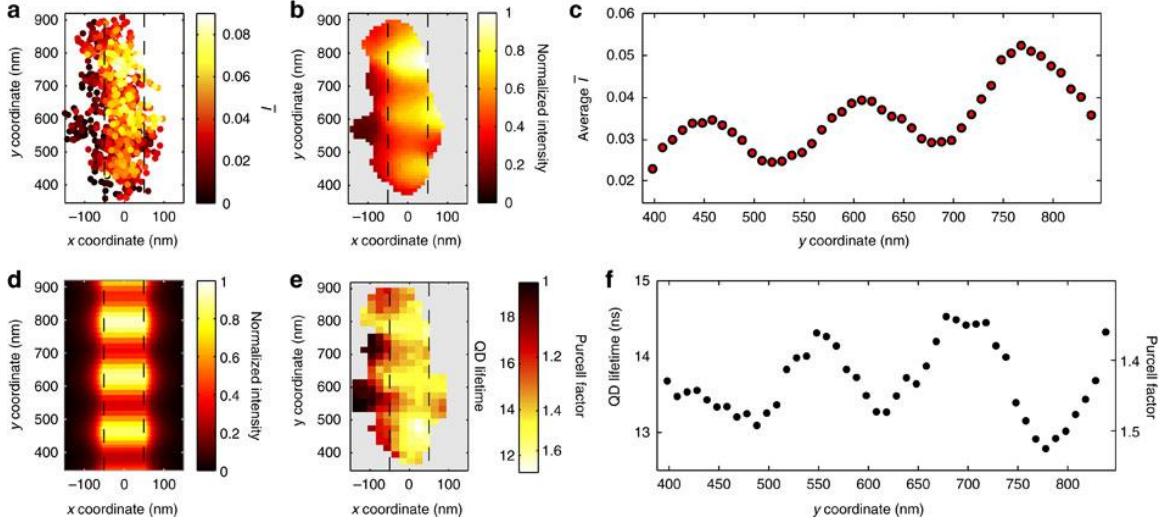
Fig. 32 SPP wave interference along an AgNW. (**a**) Scatter plot of the measured QD positions near the end of the wire. The color of each data point corresponds to the value of $\bar{I}$ measured at each location. The dashed region indicates the location of the AgNW. (**b**) Reconstructed image using a Gaussian-weighted average. The image intensity is normalized by its maximum. (**c**) Plot of an averaged value of $\bar{I}$ as a function of position along the wire. (**d**) FDTD simulation of the field intensity standing-wave pattern along the side of the AgNW (normalized by its maximum), with the profile within the dashed wire region corresponding to the field immediately outside the wire. (**e**) Image of the measured QD lifetime as a function of position. The color scale is labeled with both lifetime and Purcell factor. (**f**) Plot of QD lifetime measured along the length of the AgNW.

A periodic pattern is observed in the scatter plot along the length of the AgNW. These oscillatory fringes arise from interference between the QD emission component coupled to the forward propagating SPP wave and the backward propagating wave that is reflected from the wire end.[180] The oscillatory pattern is more readily observed in the Gaussian image reconstruction (Fig. 32(b)). Fig. 32(c) shows $\bar{I}$ plotted as a function of the y coordinate, where each data point is averaged over a ±33 nm window centred at the y coordinate. Averaging is performed only for points that are within 50 nm of the wire axis. By measuring the peak-to-peak distance from Fig. 32(c), we determine the wavelength of the SPP mode to be 320 nm, which is consistent with the 329 nm wavelength calculated from FDTD simulations. The simulated FDTD field profile is displayed in Fig. 32(d) and exhibits good qualitative agreement with the measured data.

The spatial dependence of the QD lifetime along the AgNW is shown in Fig. 32(e). The lifetime in a given pixel was measured by consolidating all photon count events when the QD was within 33 nm of the centre location of the pixel. Fig. 32(f) plots the QD lifetime when photon counts were combined using the same spatial window used to obtain Fig. 32(c). A clear oscillation in the QD lifetime is observed, mirroring the oscillations in intensity from the wire end. The QD lifetime oscillation is caused by interference between the spontaneous emission components of the forward and backward propagating SPP waves. This mechanism for modifying the spontaneous emission provides an important means of controlling and optimizing light–matter interactions between quantum emitters and nanophotonic structures.
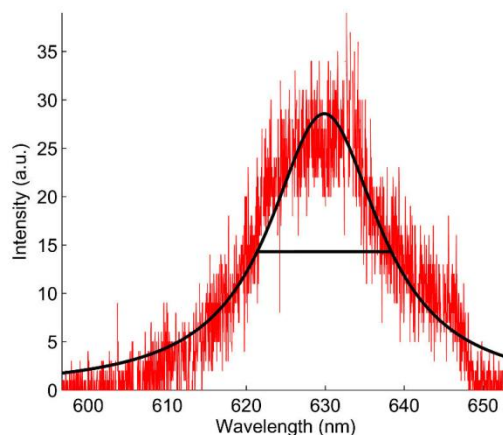
Fig. 33 Single QD Spectrum. Emission spectrum (red) of a single QD that was immobilized on a glass coverslip as measured using a grating spectrometer (Acton SP 2758). The black curve is a Lorentzian fit indicating a spectral linewidth of 17 nm.

The oscillations in Fig. 32 result from the interference between the forward propagating SPP wave and the backward wave that reflects from the near end of the AgNW. Interference will occur so long as the length difference between the two paths of the SPP waves is within the coherence length of the optical field, which can be

determined from the measured emission spectrum of a single QD. This measurement was performed using a grating spectrometer (Fig. 33). The spectral bandwidth of the QD emission, in units of free space wavelength, was determined to be $\Delta\lambda_0 = 17$ nm centered at a wavelength of $\Delta\lambda_0 = 630$ nm, which agrees well with other measured results.[218,219] The coherence length of the field propagating in the AgNW can be calculated directly from the measured spectral bandwidth using the relation[220]

$$L_{coh} = \frac{1}{2\pi}\frac{\lambda^2}{\Delta\lambda},$$ (19)

where $\lambda = 320$ nm is the measured wavelength of the SPP mode and $\lambda = \Delta\lambda_0(\lambda/\lambda_0)$. From the measured QD emission bandwidth and wavelength of the SPP mode, the coherence length is calculated to be 1.89 μm, which is long enough to observe good interference at a distance of up to 944 nm away from the AgNW end. Thus, the relatively narrow emission bandwidth of QDs makes them ideal candidates for studying interference and coherent optical effects in plasmonic nanostructures. It should be noted that other nanoscopic emitters, such as fluorescent molecules and nitrogen vacancy centers in nanodiamonds, can have much broader room-temperature emission linewidths,[149,221] sometimes exceeding 100 nm. These broad linewidths result in a significantly reduced coherence length, making it more difficult to probe interference effects without spectral filtering, which would result in a large reduction of measured signal.

5.9   Summary

A technique was demonstrated in this chapter for both nanoscale imaging of the LDOS of a silver nanowire and spontaneous emission control using a single QD. It enables on-demand control of light-matter interactions, provides a highly flexible method to optimize coupling between single quantum emitters and nanophotonic structures, and can be used to study other nanoscale phenomena such as Förster resonance energy transfer[203] and local electric field sensing.[222] The probing technique is robust to emitter degradation and photobleaching.[219] Degrading probe emitters are quickly replaced by selecting a new QD, enabling image acquisition over long integration times. Coupled with precision selection, positioning, and immobilization of single QDs,[154] this probing technique will enable deterministic and optimized assembly of active quantum emitter and plasmonic structures, leading to the development of nanoelectronic devices[157] and quantum optical circuits.[161]

Chapter 6

Electrokinetic Tweezing in 3D

6.1   Background

Vision-based electrokinetic feedback control has allowed simple microfluidic devices to manipulate microscopic[112–114] and nanoscopic[94,115,117,223] objects on chip, and has advantages over other methods. Electrokinetic (EK) tweezing, which uses electrophoretic (EP)[224] forces and/or electroosmotic (EO)[225,226] flows, allows control of the position of essentially any visible object which acquires an electric surface charge, or that is suspended in a fluid that exhibits EO flow, or both.[116] It has allowed the manipulation of one and multiple cells,[114,116] single protein molecules and fluorophores,[95] and nanoscopic quantum dots.[115,117,154] EK tweezers require less actuation effort than other methods to manipulate nanoscopic particles due to the favorable scaling of EO actuation with particle size (drag forces scale with the radius of the particle[154] rather than with its volume as do optical,[33] dielectrophoretic,[51] and magnetic forces[227]). This favorable scaling has enabled EO manipulation and trapping of single quantum dots to tens of nanometers precision[117] – the best reported precision of any method to date. EK manipulation has also been used to control the orientation of nanorods in addition to their positions by modulating the shear forces around them.[173,228]

However, all of these prior EK results have been restricted to two spatial dimensions. Here, we present a device design, associated physical modeling, 3D imaging, feedback control, and experimental results for 3-dimensional EK tweezing. As in

previous work,[229–231] EK actuation in the third dimensions (3D) is enabled by a multi-layer device. The device is fabricated by cutting microchannels into several films of polydimethylsiloxane (PDMS) and stacking them one on top of the other to form a control volume at their intersection. When voltages are applied from one layer to another, the created electric fields (for EP actuation) or fluid flows (for EO actuation) have a vertical component. Exploitation of this vertical component enables control of single particles in all 3 dimensions.

Fig. 34 Schematic of vision-based electrokinetic feedback control in two dimensions. The system is shown manipulating a neutral particle with electroosmotic (EO) flow only. A microfluidic device, control algorithm, and particle tracking system are connected in a real-time feedback loop. The vision tracking system measures the position of a particle chosen by a user. The control algorithm then calculates which EO fluid flow will carry this particle from its current towards its desired position, and electrodes then actuate the necessary fluid flow. This feedback loop repeats continually and at each time moves the chosen particle closer to its desired position, thus either trapping it in place or steering it along any desired trajectory.

We first briefly summarize how EK tweezers work in two spatial dimensions before showing how to extend the method to work in the third dimension. As shown in Fig. 34, for a 2D microfluidic device, a control algorithm, and a particle tracking system (microscope, camera, and software) are connected in a real-time feedback loop. At each time step, the particle tracking system measures the position of a chosen particle. The control algorithm then compares this measured position with the particle's desired position and calculates the necessary voltages to create an EK velocity to move that particle from where it is towards where it should be. This feedback loop repeats

continually, and at each time moves the chosen particle toward its desired position, thus either trapping it at a stationary target, or steering it along a complex trajectory by dynamically updating the target.[112–116] This process is robust to imperfections in the microfluidic device and modeling uncertainties: so long as the control algorithm knows how to move the particle from where it is *towards* where it should be, the positioning error is decreased at each time step, and the particle quickly reaches its target location – and it does so with nanoscale precision if the system has been optimized.[115,117]

6.2 Development of a multi-layer 3D microfluidic control device

In this paper, the horizontal and vertical forces needed for 3D manipulation are produced with a microfluidic device that consists of five layers of PDMS microchannels stacked on a microscope slide. PDMS films of 250 μm thickness were patterned with microchannels using a desktop vinyl cutter (Lynx 12, Sign Warehouse, Denison, TX, USA). As shown in Fig. 35(a), each PDMS layer possesses eight circular reservoirs of 3 mm diameter spaced equally around a 15 mm diameter radial pattern. The bottom four layers also possess a single straight microchannel that extends between the left-most and right-most reservoirs and chokes to a width of 385 μm at its midpoint. The layers were stacked and aligned by hand on a microscope, beginning by placing the first microchannel layer on a glass microscope slide. The remaining microchannel layers were rotated 45, 90, and 135 degrees clockwise (from the bottom to the top) relative to the first layer before being aligned and stacked on the layer below. The fifth and final layer only possesses holes for the eight channel-end reservoirs, and seals the top microchannel. The four microchannels intersect at the center of the completed device to form an octagonal

column in which particles entering from a microchannel at the top can move into a microchannel at the bottom, and vice versa.
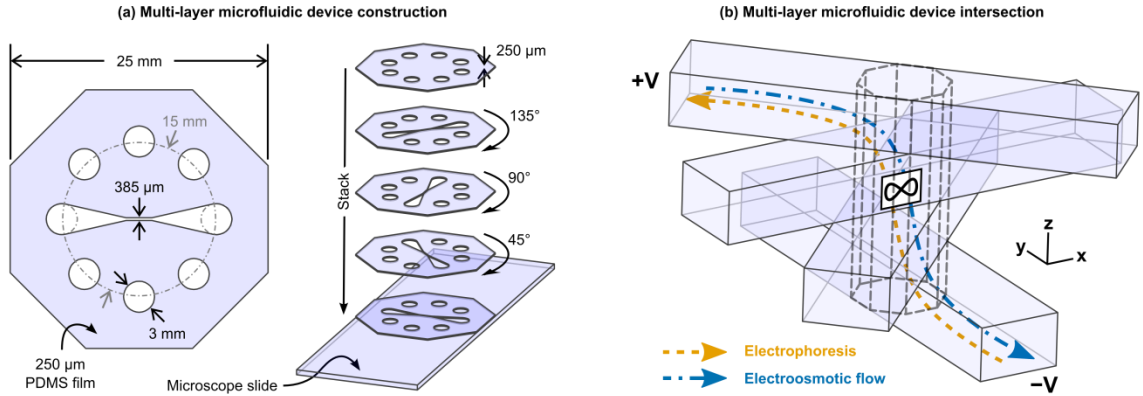
Fig. 35 Design, fabrication, and modelling of the multi-layer microfluidic control device. (a) Four layers each of PDMS film of 250 μm thickness were patterned to have a single microchannel and were stacked and aligned to form an octagonal control volume at the center of the device. A fifth layer, without microchannels, sealed the device. **(b)** When this device is actuated from top left (+V voltage) to bottom right (-V voltage), an EO flow is created from top left to bottom right (blue arrow) that drags all particles present in the device. A particle which possesses a surface charge will also experience an EP velocity in addition to the EO flow. For example, a particle with a negative surface charge will experience an EP velocity (orange arrows) which opposes the EO velocity.

Electrodes inserted into the eight channel-end reservoirs (two for each of the four channels) create an electric field in the microfluidic device that produces 3D EP and EO actuation. As shown in Fig. 35(b), when a positive potential is applied to an electrode in the top microchannel and a negative potential is applied to an electrode in the bottom microchannel, both the EP (orange dash) and EO (blue dot-dash) effects produce vertical velocities in the control volume. Any particle in the control volume can therefore experience a sinking or lifting force if actuation is applied from a top electrode to one below it, or vice versa. By properly actuating each of the eight electrodes at once we are able to precisely control both the horizontal and vertical velocities of any chosen particle. The vertical EK velocities used to steer a particle along the ∞ trajectory shown in

Fig. 35(b) are shown in Fig. 39. The horizontal EK velocities are similar to those in our prior 2-dimensional EK tweezing devices.[114,118]

6.3 Determining the 3D position of a particle

6.3.1 Defocus masking

For the control algorithm to work, it needs to know the location (x, y, z) of the particle. This location is sensed, in real-time, by a single camera and a defocus imaging method.[232–235] A "defocus mask" with multiple apertures is positioned between the infinity-corrected objective lens and the tube lens of a conventional wide-field microscope with video camera, as illustrated in Fig. 36(a) for two apertures. Light from a particle below the focal plane diverges through each aperture and reaches the image sensor of the camera at two separate locations. Conversely, light from an object positioned above the focal plane converges through each aperture, intersects before reaching the image sensor, and reaches the sensor at two separate, but flipped, locations. The distance between the two locations increases as the particle moves vertically away from the focal plane: this allows measurement of the distance of the particle from the focal plane, but does not indicate which side of the focal plane the particle is on.

(a) Simplified diagram of defocus imaging system

Focal plane

Objective lens

Defocus mask

Tube lens

Image sensor

(b) Three aperture defocus mask pattern

4 mm

2 mm

12.5 mm

(c) Imaged defocus pattern of a fluorescent particle

z < 0　　z = 0　　z > 0

20 µm
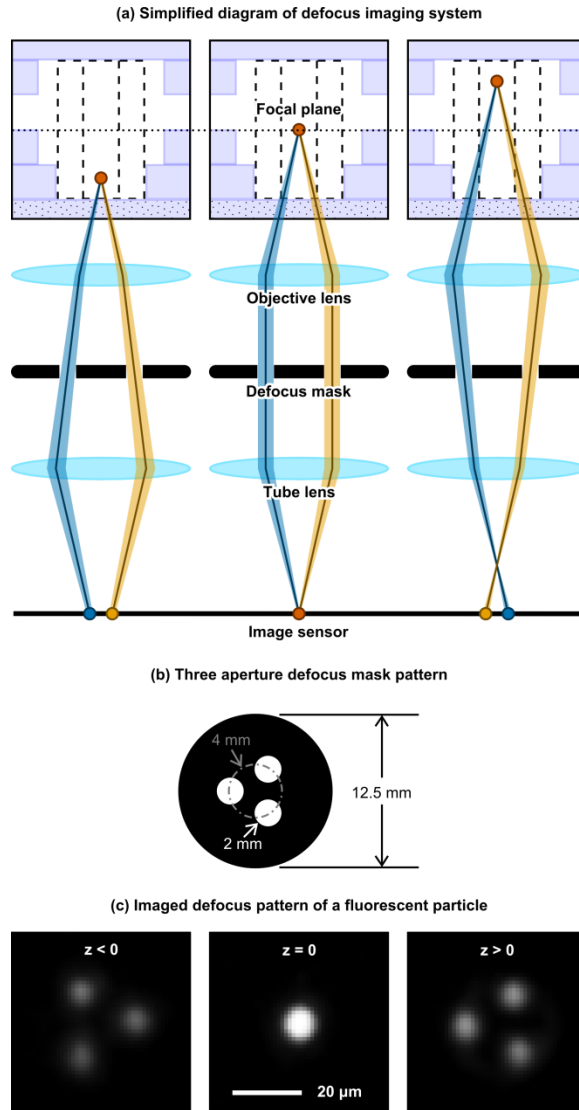
Fig. 36 Single-camera defocus imaging concept.[232–235] **(a)** In this simplified diagram, light from a particle passes through two apertures printed in a "defocus mask" mounted between an infinity-corrected objective lens and the tube lens of the microscope. Light from an object below the focal plane is captured at the image plane in two locations separated by a distance which scales with particle elevation. This image flips as the particle crosses the focal plane while a particle at the focal plane appears in focus. **(b)** To determine which side of the focal plane a particle is on, a mask with three apertures of 2 mm diameter arranged radially in a 4 mm diameter pattern was mounted on the back of a microscope objective. **(c)** The three projections of an out-of-focus particle appear at the vertices of an equilateral triangle. The distance between the projections scales with the elevation of the particle, and the orientation of the defocus pattern is flipped depending on which side of the focal plane the particle is on.

A defocus mask with three apertures was used to project three images of each particle onto the image sensor. The projection scales linearly with the displacement of the particle from the focal plane, as well as flips orientation when the particle crosses the

focal plane. The mask, as shown in Fig. 36(b), consisted of three apertures of 2 mm diameter separated by equal distance around a 4 mm diameter circle. The mask was laser-printed onto a clear transparency film and mounted on the back of the 20× magnification objective lens of a microscope. Using this mask as in Fig. 36(c), particles positioned above and below the focal plane are imaged as groups of three bright spots located at the vertices of an equilateral triangle whose orientation is flipped depending on which side of the focal plane the particle is on. Particles at the focal plane ($z = 0$ μm) appear in focus, with all three projections overlapping.

Particles far from the focal plane are located by finding groups of projections that match the configuration of the defocus mask. Individual projections are detected by finding regions of bright pixels. Before control, a particle dried on glass is imaged twice: once at the focal plane, and once at a known distance from the focal plane when the three projections are distinct. As shown in Fig. 37(a), the three projections are distinct when $|z| \geq \sim 20$ μm. The locations A, B, and C of the projections relative to the in-focus particle are saved and used as the template for finding out-of-focus particles. During each execution of the control loop, all the projections in a tracking window are found and compared to the template. First, vectors are drawn between each combination of projections. Next, the vectors are compared to the vector between points A and B on the template. If a vector has the same angle as the template vector, within some tolerance, the position of the associated particle is estimated by scaling the template and saved to a list. This is repeated with the vector between points B and C on the template. Finally, matches are accepted if two positions in the list overlap, within some tolerance. The side of the

focal plane a particle is on is easily determined by whether the group matches the orientation of the normal or flipped template.
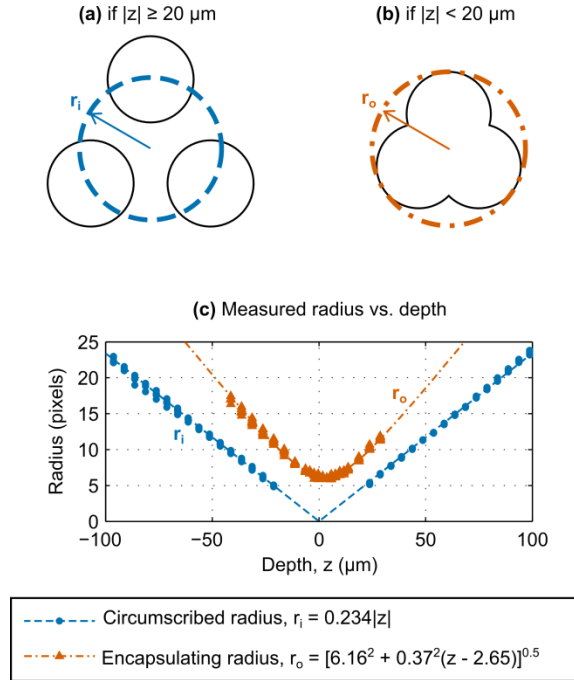
Fig. 37 Defocus pattern image processing. (a) Away from the focal plane ($|z| \geq$ 20 μm) the three projections of a particle are segregated and appear in the image as individual bright spots. A circle of radius r_i is inscribed through the centroids of the projections. **(b)** Near the focal plane ($|z| \leq$ 20 μm) the three projections overlap in the image, requiring an alternate metric of particle elevation. Therefore, a circle of radius r_o is drawn around the extent of the aggregate defocus pattern. **(c)** The inscribed radius r_i scales linearly with the displacement of a particle from the focal plane at a rate of 0.234 pixels/μm (blue circles), while the encapsulating radius r_o scales hyperbolically with a semi-major axis of 6.16 pixels and semi-minor axis of 0.37 μm centered around $z = 2.65$ μm.

Particles near the focal plane are located by measuring the extent of their overlapping projections. As shown in Fig. 37(b), the projections of a particle overlap when $|z| < {\sim}20$ μm and are measured by drawing a circle around them. As shown in Fig. 37(c), the circle of radius r_i (blue cirlces) drawn through the distinct projections of the defocus pattern scales linearly with the elevation of the particle, while the circle of radius r_o (red triangles) drawn around the extent of the overlapping defocus pattern scales hyperbolically. This hyperbolic scaling around the focal plane leads to high sensitivity of

the imaging algorithm to noise, and even a small change in r_o will cause a large change in the estimated vertical position of the particle. Uncertainty is reduced using a Kalman filter.[127]

The accuracy of the above imaging algorithm was quantified by measuring the elevation of microspheres adhered to a device as the device was raised and lowered by manually adjusting the fine focus of the microscope. Fluorescent polystyrene microspheres of 5 μm diameter were dried in place in the microchannels of a microfluidic device, and the device was raised and lowered from $z = $ -80 μm to $z = $ +80 μm. The vertical range is limited primarily by the numerical aperture (NA) of the microscope objective lens because the vertical depth in which a particle is detectable decreases as NA increases. In the xy horizontal plane, the microspheres were tracked throughout the measured range with a standard deviation as good or better than $\sigma_{xy} \approx 0.1$ μm. In the vertical z direction, the standard deviation varied with the distance of the microspheres from the focal plane, and was nearly the same on either side of the focal plane. Microspheres located near the focal plane ($|z| \leq 20$ μm), where the three projections of each microsphere overlap, were tracked with a vertical standard deviation of $\sigma_z \approx 0.4$ μm. Microspheres at a distance of $|z| \approx 20$ μm from the focal plane, where the three projections first separate (as in (a) of Fig. 37), were imaged with a vertical standard deviation of approximately $\sigma_z \approx 0.05$ μm, as good as the imaging accuracy in the xy horizontal plane. For particle elevations between 20 and 80 μm from the focal plane, the three projections of each microsphere gradually blur and dim, resulting in a gradual degradation of the standard deviation from $\sigma_z \approx 0.05$ μm at $|z| = 20$ μm to $\sigma_z \approx 0.15$ μm at $|z| = 80$ μm.

6.4   Experimental setup

Combining the 3D imaging above with our top to bottom electrokinetic actuation enables 3D EK tweezing. The multi-layer microfluidic device is observed using an inverted wide-field microscope (TS100, Nikon Corporation, Tokyo, Japan) with 20× fluorescent objective (Plan Fluor, Nikon Corporation, Tokyo, Japan) and a charge-coupled device camera (Guppy F-033C, Allied Vision Technologies, Stadtroda, Germany) that are calibrated for 3D defocus imaging. Eight electrodes are inserted into each of the eight channel-end reservoirs of the device and connected to a digital-to-analog voltage output device (USB-3106, Measurement Computing, Norton, MA, USA) that is in turn connected to a personal computer. Custom software locates, tracks, and manipulates, in real-time, any chosen object in the control volume. During each iteration of the control loop, the desired position of the object is dynamically updated with coordinates supplied either by user input or by a pre-planned trajectory. The voltages required to move the particle from its measured position towards its desired position are calculated by the control algorithm and are applied to the microfluidic device. This loop is continually repeated at ~20 Hz, enabling steering of objects along complex trajectories as well as precise and accurate trapping of objects in 3D.

6.5   Positioning of a single polystyrene microsphere

6.5.1   Steering along the edges of a tilted cube

To demonstrate 3D electrokinetic tweezing, we steered a single polystyrene microsphere of 5 μm diameter (G0500, Duke Scientific Corporation, Palo Alto, CA, USA) along the edges of a tilted cube. Fig. 38(a) shows the two-dimensional images

acquired from the camera at four different time points as the microsphere was steered along the desired trajectory with a constant velocity of 2.5 µm/s. The trajectory of the microsphere (orange dots) closely follows the desired cube trajectory (solid green line). Fig. 38(b) shows a trace of the 3D path of the microsphere. During steering, the increased imaging error near the focal plane is mitigated by a Kalman filter, which uses the EK velocity predicted by the mathematical model to estimate which side of the focal plane the microsphere is on. The errors measured here for 3D steering are comparable to the error attained with our early 2D steering results.[113,114]
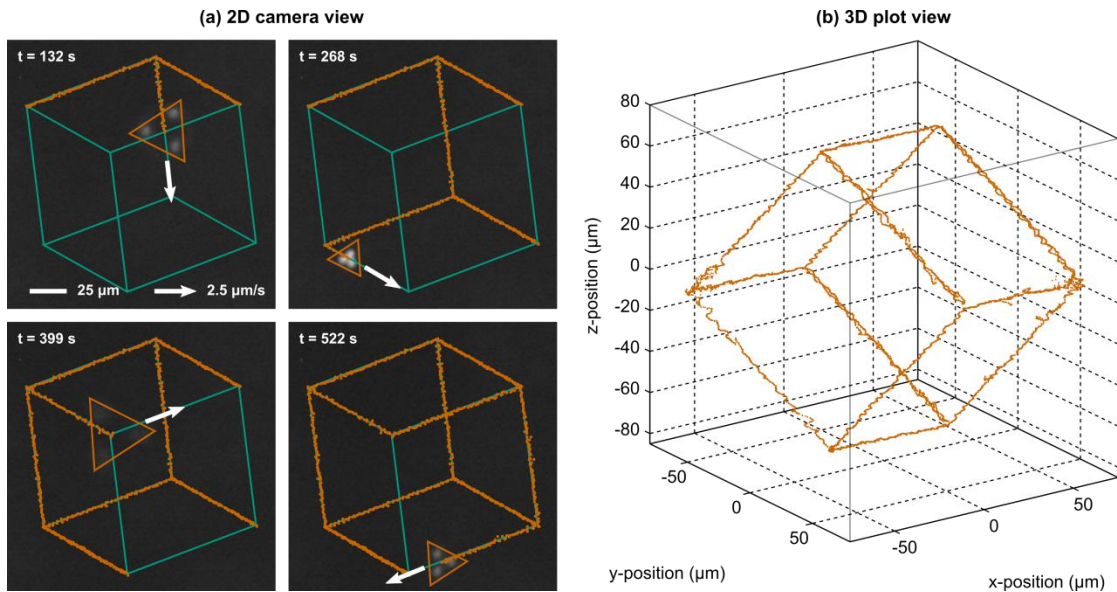
Fig. 38 A single polystyrene microsphere of 5 µm diameter was steered along the edges of a tilted cube at a velocity of 2.5 µm/s. (a) The image of the device through the defocus mask is shown at times $t =$ 132, 268, 399, and 522 s. The desired cube trajectory is overlaid as a solid green line and the path taken by microsphere is shown by orange dots. **(b)** A 3D plot of the complete path taken by the microsphere. The microsphere was steered with an RMS error of 1.17 µm in the xy plane and 1.25 µm in the vertical z direction.

6.5.2 Accuracy of stationary trapping

To quantify EK trapping accuracy, we trapped microspheres at several elevations in the control volume. Microspheres trapped below the focal plane ($z < $ -20 µm) were

trapped with a root mean square (RMS) error of less than 1 μm both in the xy plane and in the z direction. Microspheres trapped above the focal plane ($z > 20$ μm) experienced the same accuracy in the xy plane, but a slightly decreased accuracy in the z direction of ~1.5 μm (at this time it is still unclear why trapping accuracy in the z direction differs slightly from one side of the focal plane to the other). At the focal plane, microspheres were trapped with an RMS error of ~1.5 μm in the xy plane and ~2.5 μm in the z direction. Increased error in the z direction for a microsphere near the focal plane is due to increased imaging sensitivity to noise, as discussed above, as well as errors due to uncertainty in whether the particle is above or below the focal plane.

6.5.3 Measurement of electrophoretic and electroosmotic mobilities

The relative contribution of EP and EO to the velocity of the microspheres was estimated by comparing the measured velocity of the particle with the electric field controlled in the device. As in equation 5 of Chapter 2, $\vec{v}_{EK} = \mu_{EK}\vec{E}$, the EK mobility $\mu_{EK} = \mu_{EP} + \mu_{EO}$ relates the velocity of a particle with the electric field in the device, and is the sum of the EP and EO mobilities. Based on the data in Fig. 38, the net EK mobility for the polystyrene microspheres suspended in DI water in our PDMS microfluidic device is approximately $\mu_{EK} \approx$ -17.6 $\times 10^{-9}$ m^{2}V^{-1}s^{-1}. Without more information it is difficult to separate the EK mobility into its constituent EP and EO parts. Based on our previous work for 2D control,[114] we estimate that the EO mobility of the device is $\mu_{EO} \approx 36.5 \times 10^{-9}$ m^{2}V^{-1}s^{-1}. The EP mobility of the microspheres is then $\mu_{EP} \approx$ -54.1 $\times 10^{-9}$ m^{2}V^{-1}s^{-1}, which is consistent with that work. With these mobilities, Fig. 39(a) shows four of the fields created while moving a particle along the vertical

plane ∞ trajectory shown in the inset in panel (b) of Fig. 35. Fig. 39(b) shows the

opposing, but well aligned, contributions from EP (yellow) and EO (blue) to the overall

EK velocity.
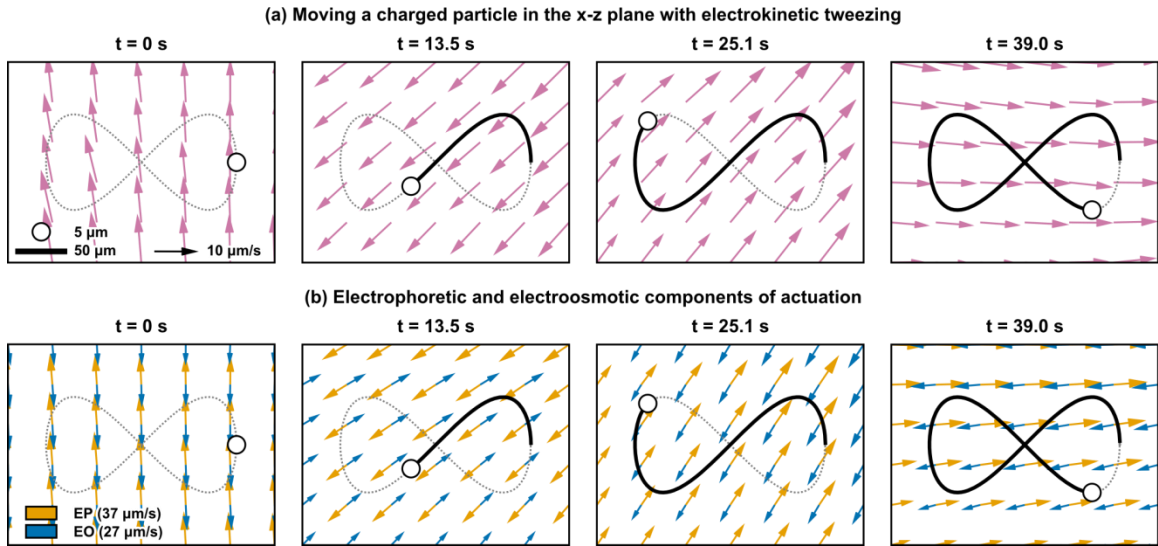
Fig. 39 Electrokinetic velocities created while steering a particle along a vertical trajectory. (a) By applying the correct voltage to each of the eight electrodes at once it is possible to impart the desired horizontal and vertical EK velocities to a particle at any location. For example, here we show the EK velocity fields created while steering a particle along the vertical ∞ trajectory shown in panel **(b)** of Fig. 35. Note that at each time the EK velocity is pointed along the tangent of the desired trajectory at the location of the particle (black circle). **(b)** For a negatively charged particle, the velocity components due to EP (orange) and EO (blue) oppose each other, but since their sum is usually non-zero the control algorithm can use their combination (the magenta arrows in panel a) to manipulate any single particle as desired.

6.6   Summary

Electrokinetic tweezing of microparticles in three dimensions was demonstrated

in this chapter with a multi-layer microfluidic device, a model-based control algorithm,

and a single-camera 3D imaging system. Compared to laser tweezers and other methods,

EK tweezers are inexpensive and use fluid forces that scale with radius of the object

being controlled rather than volume,[44] allowing them to manipulate nanoscale objects in

2D with accuracy in the tens of nanometers.[115,117,154,236] The multi-layer microfluidic

device is fabricated with a desktop fabrication technique and produces both the horizontal and vertical forces needed to move particles in all three dimensions. The position of each particle is estimated in real-time using a 3D imaging system that makes out-of-focus particles appear in a triangular pattern which scales with the elevation of the particle. This system was used to precisely steer polystyrene microspheres of 5 μm diameter along a three-dimensional trajectory, as well as trap them in place with accuracy as good as 1 μm. To the best of our knowledge, this is the first experimental demonstration of EK tweezing in three spatial dimensions.

Chapter 7

Conclusions

In this thesis I described the implementation of a system that manipulates nano and microscopic objects using electrokinetic forces, its use in manipulating cancer cells and nanoparticles, and its extension into three dimensions.

EK tweezers are a vision-based feedback control system that allow simple microfluidic devices to perform complex laboratory techniques and uses forces that scale favorably for small objects,[44,116] enabling gentle control of cells and nanoprecise control of nanoscale objects.[115,154] The implementation of EK tweezers uses commercially available hardware and software and provides an easy-to-use graphical user interface, making it easy adapt to multiple research applications. As a demonstration, EK tweezers are used to measure the attachment forces between two cancer cells that possess microtentacles, protrusions from the cell membrane present on circulating tumor cells (CTCs) that allow them to attach reattach at distant tissues and to other CTCs, leading to metastasis.[136–138]

EK tweezers are next used to manipulate nanoscopic quantum dots and metallic nanowires for on-demand selection, assembly, and imaging of nanophotonic structures. Quantum dots (QDs) are semiconductor nanocrystals that can be used as single-photon emitters[146] when placed with 150 nm of the high field regions of nanophotonic circuits.[152] Using sensitive optics and a high viscosity fluid, single QDs were trapped with an accuracy of 45 nm and steered on complex trajectories with an accuracy of 120 nm, well

within the desired accuracy.[117] A photoresist was added to the fluid, allowing QDs to be immobilized in a polymer with 127 nm accuracy when exposed to a UV flash.[154] Metallic nanowires allow light to be transferred in the form of surface plasmons and can be used to construct nanophotonic circuits such as subwavelength interferometers[158] resonators,[180] single-photon sources,[181] and nonlinear quantum devices.[161] EK tweezers positioned and oriented silver nanowires by pivoting them around polymerized anchors, and assembled them into complex nanostructures.[236] The optical properties of single nanowires were then imaged with nanoscale resolution by scanning single QD probes in around them using a program run in parallel to control.[115]

Finally, I extended EK tweezers into three dimensions using a multi-layer microfluidic device design and a single-camera 3D imaging system. The multi-layer microfluidic device is fabricated with a desktop fabrication technique and produces both the horizontal and vertical forces necessary for manipulation of particles in all three dimensions. The position of each particle is estimated in real-time using a defocus imaging system that masks out-of-focus particles into a triangular pattern that scales with the elevation of the particle.[232–235] This system steered polystyrene microspheres of 5 μm diameter along a three-dimensional trajectory, and trapped them with accuracy as good as 1 μm. To the best of our knowledge, this is the first experimental demonstration of EK manipulation in three dimensions.

The methods and automation developed here can be used in any research area where there is need to handle nano and microscopic objects that are otherwise impossible to address. Broadly, vision-based feedback control like in EK tweezers can help microfluidic devices operate efficiently despite uncertainties in devices and samples. In

biology, the ability to analyze the genetic and protein makeup of single cells allows characterization of heterogeneity, detection of rare biomarkers, and elucidation of complex biological processes that are lost in the noise of bulk experiments.[3] In nanotechnology, the ability to select and position nanophotonic components such as quantum dots and nanowires can be used to build and analyze nanoelectronic devices[157] and quantum optical circuits.[161] The ability to do all these things in 3D opens many more possibilities that are only just beginning to be explored.

Intellectual Contributions

Table of Contributions

All the work here was the result of many years of collaboration. In this chapter, I try to attribute key aspects of the work to the people most responsible for them. For quick reference, the table below summarizes my contribution relative to my collaborators. The first column lists the projects discussed in this dissertation. The second column highlights my work on those projects. The third column highlights the work of my collaborators.

Project	My contribution	Collaborators' contribution
Implementation of Electrokinetic Tweezing (Chapter 3)	*with Probst:* Development of an intuitive hardware and software platform for rapid application of EK tweezing for cell and particle manipulation tasks Programming and support of graphical user interface which enable manipulation tasks such as particle dragging and path planning	*Armani, Chaudhary, Probst*: Development of initial modeling, control, and image processing
Nanowire Assembly (Chapter 4)	Application of EK tweezing platform and GUI for the manipulation of quantum dots and nanowires Development of imaging and control algorithms to identify and handle QD blinking Implementation of nanowire imaging and development of control algorithms for control of nanowire orientation	*Ropp*: Primary development of microscopy platform, experiment staging, and data processing *Probst*: Modification of microfluidic control device and actuation, experiment staging *Ropp, Probst, Kumar*: Development of photocurable medium for immobilization of nanostructures

Nanoscale Imaging and Spontaneous Emission Control (Chapter 5)	Development of GUI for automated scanning of optical characteristics of nanowires using QDs as probes	
Electrokinetic Tweezing in 3D (Chapter 6)	Design and fabrication of a multi-layer microfluidic device capable of producing 3D electrokinetic forces

Modeling and implementation of three dimensional control

Implementation and calibration of three dimensional imaging | *Armani, Chaudhary, Probst*: Development of initial modeling, control, and image processing for two dimensional control

Probst: Formalization and simulation of three dimensional control |

Implementation of Electrokinetic Tweezing

Development of hardware and software platform

Roland Probst and I developed the next generation implementation of electrokinetic tweezing. Probst gathered hardware compatible with MATLAB. With his guidance, I developed the graphical user interface.

Steering of multiple particles and microbes

The new implementation recreated old manipulation results for up to three objects, and was used to show manipulation of as many as five objects and swimming microbes for the first time. With Satej Chaudhary and Probst, manipulation results for the steering of multiple particles were replicated using the next generation platform. Optimal steering of up to five particles was demonstrated for the first time with Chaudhary (not shown here). Steering of swimming microbes was performed with Probst.

Manipulation of circulating tumor cells

With Probst, EK tweezers were set up in Stuart Martin's laboratory at the University of Maryland, Baltimore. Probst developed the technique to plug the reservoirs of the device with electrode gels. To allow cells to be controllably introduced to the control region without becoming stuck, I developed a manually controlled gravity-based fluid conveyor that fed cells from a reservoir of cells in nutrient medium into the device. I performed most patterning and bumping experiments. Martin graciously donated his time, space, and equipment. In addition to culturing and maintaining cells, his comments and suggestions were invaluable.

Manipulation of quantum dots

Probst, Chad Ropp, and I set up EK tweezers in Edo Waks' photonics laboratory. Probst optimized the control device for quantum dot control. Ropp assembled optics. With Rakesh Kumar, Srinivasa Raghavan, and lots of trial and error, Probst and Ropp developed the viscous photocurable buffer used to control and immobilize QDs. I supported software, developed imaging to track blinking QDs, implemented piezo stage control to keep QDs in focus, and developed targeting to guide QDs to the center of the UV beam. I supported experiments primarily carried out by Probst and Ropp.

Nanowire Assembly

I implemented imaging and control of nanowires that allowed manual assembly of nanostructures. Ropp noticed the ability to rotate a nanowire by immobilizing one end with polymer, or by pivoting it around a previously immobilized QDs or empty polymer.

I implemented image processing and control to precisely control the orientation of the nanowire. Nanowire image processing was aided by Pramod Mathai.[173] Ropp performed experiments with my support.

Nanoscale Imaging and Spontaneous Emission Control

The spatial dependence of photonic coupling between a QD and a nanowire was imaged by scanning the QD over the nanowire. I developed the scanning program that automated the movement of a QD probe between a set of grid points. The program allowed users to align a graphical representation of the nanowire to the nanowire, draw the imaging area, and specify the resolution of the grid. Experiments and image post-processing processing and analysis were carried about by Ropp with my support.

Electrokinetic Tweezing in 3D

Inspired by Probst's and Shapiro's earlier work,[231] I extended EK tweezing to three dimensions with a novel multi-layer microfluidic device and 3D imaging. I designed and developed the device by cutting films of PDMS using a vinyl cutter, as suggested by Katayoon Saadin. I modeled and implemented three dimensional control in the EK tweezing platform by adding the needed variables and user controls to the program. I implemented 3D imaging by modifying the microscope optics and developing the imaging algorithm. I performed all experiments.

Bibliography

1. Holde, K. E. van. Biochemistry at the Single-molecule Level: Minireview Series. *J. Biol. Chem.* **274,** 14515–14515 (1999).

2. Birnbaum, J. & Williams, R. S. Physics and the Information Revolution. *Phys. Today* **53,** 38–42 (2007).

3. Wang, D. & Bodovitz, S. Single cell analysis: the new frontier in 'Omics'. *Trends Biotechnol.* **28,** 281–290 (2010).

4. Pantel, K., Alix-Panabières, C. & Riethdorf, S. Cancer micrometastases. *Nat. Rev. Clin. Oncol.* **6,** 339–351 (2009).

5. Hüsemann, Y. *et al.* Systemic Spread Is an Early Step in Breast Cancer. *Cancer Cell* **13,** 58–68 (2008).

6. Naumov, G. N. *et al.* Persistence of Solitary Mammary Carcinoma Cells in a Secondary Site A Possible Contributor to Dormancy. *Cancer Res.* **62,** 2162–2168 (2002).

7. Gunn, C. CMOS Photonics for High-Speed Interconnects. *IEEE Micro* **26,** 58–66 (2006).

8. Bose, R., Sridharan, D., Kim, H., Solomon, G. S. & Waks, E. Low-Photon-Number Optical Switching with a Single Quantum Dot Coupled to a Photonic Crystal Cavity. *Phys. Rev. Lett.* **108,** 227402 (2012).

9. Bennett, C. H. & Brassard, G. Quantum cryptography: Public key distribution and coin tossing. *Theor. Comput. Sci.* **560, Part 1,** 7–11 (2014).

10. Shor, P. Polynomial-Time Algorithms for Prime Factorization and Discrete Logarithms on a Quantum Computer. *SIAM J. Comput.* **26,** 1484–1509 (1997).

11. Alivisatos, A. P. Semiconductor Clusters, Nanocrystals, and Quantum Dots. *Science* **271,** 933–937 (1996).

12. Averitt, R. D., Sarkar, D. & Halas, N. J. Plasmon Resonance Shifts of Au-Coated Au_2S Nanoshells: Insight into Multicomponent Nanoparticle Growth. *Phys. Rev. Lett.* **78,** 4217–4220 (1997).

13. Whitesides, G. M. The origins and the future of microfluidics. *Nature* **442,** 368–373 (2006).

14. Squires, T. M. & Quake, S. R. Microfluidics: Fluid physics at the nanoliter scale. *Rev Mod Phys* **77,** 977–1026 (2005).

15. Herold, K. E. & Rasooly, A. *Lab on a Chip Technology: Fabrication and microfluidics.* (Horizon Scientific Press, 2009).

16. Bhise, N. S. *et al.* Organ-on-a-chip platforms for studying drug delivery systems. *J. Controlled Release* **190,** 82–93 (2014).

17. Verpoorte, E. Microfluidic chips for clinical and forensic analysis. *ELECTROPHORESIS* **23,** 677–712 (2002).

18. Nagrath, S. *et al.* Isolation of rare circulating tumour cells in cancer patients by microchip technology. *Nature* **450,** 1235–1239 (2007).

19. Stott, S. L. *et al.* Isolation of circulating tumor cells using a microvortex-generating herringbone-chip. *Proc. Natl. Acad. Sci.* **107,** 18392–18397 (2010).

20. Zheng, S. *et al.* 3D microfilter device for viable circulating tumor cell (CTC) enrichment from blood. *Biomed. Microdevices* **13,** 203–213 (2011).

Bibliography

21. Hood, L., Heath, J. R., Phelps, M. E. & Lin, B. Systems Biology and New Technologies Enable Predictive and Preventative Medicine. *Science* **306,** 640–643 (2004).

22. Valencia, P. M., Farokhzad, O. C., Karnik, R. & Langer, R. Microfluidic technologies for accelerating the clinical translation of nanoparticles. *Nat. Nanotechnol.* **7,** 623–629 (2012).

23. Chaillet, N. & Régnier, S. *Microrobotics for Micromanipulation*. (John Wiley & Sons, 2013).

24. Zeng, J. *et al.* A Minimally Invasive Method for Retrieving Single Adherent Cells of Different Types from Cultures. *Sci. Rep.* **4,** (2014).

25. Anis, Y. H., Holl, M. R. & Meldrum, D. R. Automated Selection and Placement of Single Cells Using Vision-Based Feedback Control. *IEEE Trans. Autom. Sci. Eng.* **7,** 598–606 (2010).

26. Fleming, S. D. & King, R. S. *Micromanipulation in Assisted Conception*. (Cambridge University Press, 2003).

27. Stroscio, J. A. & Eigler, D. M. Atomic and Molecular Manipulation with the Scanning Tunneling Microscope. *Science* **254,** 1319–1326 (1991).

28. Guthold, M. *et al.* Controlled manipulation of molecular samples with the nanoManipulator. *IEEEASME Trans. Mechatron.* **5,** 189–198 (2000).

29. Grier, D. G. A revolution in optical manipulation. *Nature* **424,** 810–816 (2003).

30. Zhang, H. & Liu, K.-K. Optical tweezers for single cells. *J. R. Soc. Interface* **5,** 671–690 (2008).

31. Neuman, K. C. & Nagy, A. Single-molecule force spectroscopy: optical tweezers, magnetic tweezers and atomic force microscopy. *Nat Meth* **5,** 491–505 (2008).

32. Ashkin, A. History of optical trapping and manipulation of small-neutral particle, atoms, and molecules. *IEEE J. Sel. Top. Quantum Electron.* **6,** 841–856 (2000).

33. Neuman, K. C. & Block, S. M. Optical trapping. *Rev. Sci. Instrum.* **75,** 2787 (2004).

34. Neale, S. L., Mazilu, M., Wilson, J. I. B., Dholakia, K. & Krauss, T. F. The resolution of optical traps created by Light Induced Dielectrophoresis (LIDEP). *Opt. Express* **15,** 12619 (2007).

35. Padgett, M. & Bowman, R. Tweezers with a twist. *Nat. Photon* **5,** 343–348 (2011).

36. Curtis, J. E., Koss, B. A. & Grier, D. G. Dynamic holographic optical tweezers. *Opt. Commun.* **207,** 169–175 (2002).

37. Agarwal, R. *et al.* Manipulation and assembly of nanowires with holographic optical traps. *Opt. Express* **13,** 8906 (2005).

38. Leach, J. *et al.* 3D manipulation of particles into crystal structures using holographic optical tweezers. *Opt. Express* **12,** 220 (2004).

39. Conkey, D. B., Trivedi, R. P., Pavani, S. R. P., Smalyukh, I. I. & Piestun, R. Three-dimensional parallel particle manipulation and tracking by integrating holographic optical tweezers and engineered point spread functions. *Opt. Express* **19,** 3835 (2011).

40. OTKB, Thorlabs, Newton, NJ, US.

41. Dienerowitz, M. Optical manipulation of nanoparticles: a review. *J Nanophoton* **2,** 021875 (2008).

42. Einstein, A. Über die von der molekularkinetischen Theorie der Wärme geforderte Bewegung von in ruhenden Flüssigkeiten suspendierten Teilchen. *Ann. Phys.* **322,** 549–560 (1905).

43. Brown, R. A Brief Account of Microscopical Observations made in the Months of June, July, and August, 1827, on the Particles contained in the Pollen of Plants; and on the General Existence of Active Molecules in Organic and Inorganic Bodies. *Misc. Bot. Works Robert Brown* 463–486 (2015). doi:10.1017/cbo9781107775473.016

44. Probstein, R. F. Physicochemical Hydrodynamics. (1994). doi:10.1002/0471725137

Bibliography

45. Sutherland, W. LXXV. A dynamical theory of diffusion for non-electrolytes and the molecular mass of albumin. *Philos. Mag. Ser. 6* **9,** 781–785 (1905).

46. Mirsaidov, U. *et al.* Optimal optical trap for bacterial viability. *Phys. Rev. E* **78,** 021910 (2008).

47. König, K., Tadir, Y., Patrizio, P., Berns, M. W. & Tromberg, B. J. Andrology: Effects of ultraviolet exposure and near infrared laser tweezers on human spermatozoa. *Hum. Reprod.* **11,** 2162–2164 (1996).

48. Neuman, K. C., Chadd, E. H., Liou, G. F., Bergman, K. & Block, S. M. Characterization of Photodamage to Escherichia coli in Optical Traps. *Biophys. J.* **77,** 2856–2863 (1999).

49. Lapizco-Encinas, B. H. & Rito-Palomares, M. Dielectrophoresis for the manipulation of nanobioparticles. *Electrophoresis* **28,** 4521–4538 (2007).

50. Zhang, C., Khoshmanesh, K., Mitchell, A. & Kalantar-zadeh, K. Dielectrophoresis for manipulation of micro/nano particles in microfluidic systems. *Anal. Bioanal. Chem.* **396,** 401–420 (2009).

51. Pohl, H. A. *Dielectrophoresis: the behavior of neutral matter in nonuniform electric fields*. (Cambridge University Press, 1978).

52. Pethig, R. Dielectrophoresis: Status of the theory, technology, and applications. *Biomicrofluidics* **4,** 022811 (2010).

53. Khoshmanesh, K., Nahavandi, S., Baratchi, S., Mitchell, A. & Kalantar-zadeh, K. Dielectrophoretic platforms for bio-microfluidic systems. *Biosens. Bioelectron.* **26,** 1800–1814 (2011).

54. Thomas, R. S., Morgan, H. & Green, N. G. Negative DEP traps for single cell immobilisation. *Lab Chip* **9,** 1534 (2009).

55. Huang, J.-T., Wang, G.-C., Tseng, K.-M. & Fang, S.-B. A chip for catching, separating, and transporting bio-particles with dielectrophoresis. *J Ind Microbiol Biotechnol* **35,** 1551–1557 (2008).

56. Morgan, H., Sun, T., Holmes, D., Gawad, S. & Green, N. G. Single cell dielectric spectroscopy. *J Phys Appl Phys* **40,** 61–70 (2006).

57. Hunt, T. P. & Westervelt, R. M. Dielectrophoresis tweezers for single cell manipulation. *Biomed Microdevices* **8,** 227–230 (2006).

58. Hölzel, R., Calander, N., Chiragwandi, Z., Willander, M. & Bier, F. F. Trapping Single Molecules by Dielectrophoresis. *Phys. Rev. Lett.* **95,** (2005).

59. Edwards, B., Engheta, N. & Evoy, S. Electric tweezers: Experimental study of positive dielectrophoresis-based positioning and orientation of a nanorod. *J. Appl. Phys.* **102,** 024913 (2007).

60. Chang, D. E. & Petit, N. Toward controlling dielectrophoresis. *Int J Robust Nonlinear Control* **15,** 769–784 (2005).

61. Melnyk, M. P. & Chang, D. E. Time optimal control of a dielectrophoretic system. *Asian J. Control* **13,** 480–491 (2010).

62. Chiou, P. Y., Ohta, A. T. & Wu, M. C. Massively parallel manipulation of single cells and microparticles using optical images. *Nature* **436,** 370–372 (2005).

63. Wu, M. C. Optoelectronic tweezers. *Nat. Photon* **5,** 322–324 (2011).

64. Valley, J. K., Jamshidi, A., Ohta, A. T., Hsu, H.-Y. & Wu, M. C. Operational Regimes and Physics Present in Optoelectronic Tweezers. *J Microelectromech Syst* **17,** 342–350 (2008).

65. Wu, J. Acoustical tweezers. *J Acoust Soc Am* **89,** 2140 (1991).

66. Hertz, H. M. Standing-wave acoustic trap for nonintrusive positioning of microparticles. *J. Appl. Phys.* **78,** 4845 (1995).

67. Wang, J. & Dual, J. Theoretical and numerical calculations for the time-averaged acoustic force and torque acting on a rigid cylinder of arbitrary size in a low viscosity fluid. *J Acoust Soc Am* **129,** 3490 (2011).

68. King, L. V. On the Acoustic Radiation Pressure on Spheres. *Proc. R. Soc. Math. Phys. Eng. Sci.* **147,** 212–240 (1934).

69. Gor'kov, L. P. On the Forces Acting on a Small Particle in an Acoustical Field in an Ideal Fluid. *Sov. Phys. Dokl.* **6,** 773 (1962).

70. Barmatz, M. Acoustic radiation potential on a sphere in plane, cylindrical, and spherical standing wave fields. *J Acoust Soc Am* **77,** 928 (1985).

71. BARRIOS, G. & RECHTMAN, R. Dynamics of an acoustically levitated particle using the lattice Boltzmann method. *J. Fluid Mech.* **596,** (2008).

72. Saito, M., Kitamura, N. & Terauchi, M. Ultrasonic manipulation of locomotive microorganisms and evaluation of their activity. *J. Appl. Phys.* **92,** 7581 (2002).

73. Haake, A. & Dual, J. Contactless micromanipulation of small particles by an ultrasound field excited by a vibrating body. *J Acoust Soc Am* **117,** 2752 (2005).

74. Chung, S. K. & Cho, S. K. 3-D manipulation of millimeter- and micro-sized objects using an acoustically excited oscillating bubble. *Microfluid Nanofluid* **6,** 261–265 (2008).

75. de Vries, A. H. B., Krenn, B. E., van Driel, R. & Kanger, J. S. Micro Magnetic Tweezers for Nanomanipulation Inside Live Cells. *Biophys. J.* **88,** 2137–2144 (2005).

76. Amblard, F., Yurke, B., Pargellis, A. & Leibler, S. A magnetic manipulator for studying local rheology and micromechanical properties of biological systems. *Rev. Sci. Instrum.* **67,** 818 (1996).

77. Fisher, J. K. *et al.* Thin-foil magnetic force system for high-numerical-aperture microscopy. *Rev. Sci. Instrum.* **77,** 023702 (2006).

78. Gosse, C. & Croquette, V. Magnetic Tweezers: Micromanipulation and Force Measurement at the Molecular Level. *Biophys. J.* **82,** 3314–3329 (2002).

79. Lee, H., Liu, Y., Westervelt, R. M. & Ham, D. IC/Microfluidic Hybrid System for Magnetic Manipulation of Biological Cells. *IEEE J. Solid-State Circuits* **41,** 1471–1480 (2006).

80. Liu, C., Lagae, L. & Borghs, G. Manipulation of magnetic particles on chip by magnetophoretic actuation and dielectrophoretic levitation. *Appl. Phys. Lett.* **90,** 184109 (2007).

81. Hagiwara, M. *et al.* On-chip magnetically actuated robot with ultrasonic vibration for single cell manipulations. *Lab Chip* **11,** 2049 (2011).

82. Lipfert, J., Wiggin, M., Kerssemakers, J. W. J., Pedaci, F. & Dekker, N. H. Freely orbiting magnetic tweezers to directly monitor changes in the twist of nucleic acids. *Nat Comms* **2,** 439 (2011).

83. Kummer, M. P. *et al.* OctoMag: An Electromagnetic System for 5-DOF Wireless Micromanipulation. *IEEE Trans. Robot.* **26,** 1006–1017 (2010).

84. Arcese, L., Fruchard, M. & Ferreira, A. Nonlinear modeling and robust controller-observer for a magnetic microrobot in a fluidic environment using MRI gradients. *2009 IEEERSJ Int. Conf. Intell. Robots Syst.* (2009). doi:10.1109/iros.2009.5354600

85. Arcese, L., Cherry, A., Fruchard, M. & Ferreira, A. Dynamic behavior investigation for trajectory control of a microrobot in blood vessels. *2010 IEEERSJ Int. Conf. Intell. Robots Syst.* (2010). doi:10.1109/iros.2010.5650895

86. Belharet, K., Folio, D. & Ferreira, A. MRI-based microrobotic system for the propulsion and navigation of ferromagnetic microcapsules. *Minim. Invasive Ther. Allied Technol.* **19,** 157–169 (2010).

Bibliography

87. Belharet, K., Folio, D. & Ferreira, A. Three-Dimensional Controlled Motion of a Microrobot using Magnetic Gradients. *Adv. Robot.* **25,** 1069–1083 (2011).

88. Probst, R. *et al.* Planar steering of a single ferrofluid drop by optimal minimum power dynamic feedback control of four electromagnets at a distance. *J. Magn. Magn. Mater.* **323,** 885–896 (2011).

89. Engel-Herbert, R. & Hesjedal, T. Calculation of the magnetic stray field of a uniaxial magnetic domain. *J. Appl. Phys.* **97,** 074504 (2005).

90. Domokos, C. & Hajagos, I. Computation and visualization of magnetic fields. in (2006). at <http://www.cescg.org/CESCG-2006/papers/Szeged-Hajagos-Imre.pdf>

91. Lee, H., Purdon, A. M. & Westervelt, R. M. Manipulation of biological cells using a microelectromagnet matrix. *Appl. Phys. Lett.* **85,** 1063 (2004).

92. Jabeen, R., Payne, D., Wiktorowicz, J., Mohammad, A. & Petersen, J. Capillary electrophoresis and the clinical laboratory. *Electrophoresis* **27,** 2413–2438 (2006).

93. Price, A. K. & Culbertson, C. T. Chemical analysis of single mammalian cells with microfluidics. *Anal. Chem.* **79,** 2614–2621 (2007).

94. Cohen, A. E. & Moerner, W. E. Method for trapping and manipulating nanoscale objects in solution. *Appl. Phys. Lett.* **86,** 093109 (2005).

95. Cohen, A. E. & Moerner, W. E. Controlling Brownian motion of single protein molecules and single fluorophores in aqueous buffer. *Opt. Express* **16,** 6941 (2008).

96. Fields, A. P. & Cohen, A. E. Electrokinetic trapping at the one nanometer limit. *Proc. Natl. Acad. Sci.* **108,** 8937–8942 (2011).

97. Voldman, J. Electrical Forces for Microscale Cell Manipulation. *Annu. Rev. Biomed. Eng.* **8,** 425–454 (2006).

98. Gao, J., Yin, X.-F. & Fang, Z.-L. Integration of single cell injection, cell lysis, separation and detection of intracellular constituents on a microfluidic chip. *Lab. Chip* **4,** 47–52 (2004).

99. Brown, R. B. & Audet, J. Current techniques for single-cell lysis. *J. R. Soc. Interface* **5,** S131–S138 (2008).

100. Ramsey, J. M., Jacobson, S. C., Culbertson, C. T. & Ramsey, R. S. in *Micro Total Analysis Systems 2000* (eds. Berg, A. van den, Olthuis, W. & Bergveld, P.) 213–216 (Springer Netherlands, 2000). at <http://link.springer.com/chapter/10.1007/978-94-017-2264-3_49>

101. Karimi, A., Yazdi, S. & Ardekani, A. M. Hydrodynamic mechanisms of cell and particle trapping in microfluidics. *Biomicrofluidics* **7,** (2013).

102. Tanyeri, M., Johnson-Chavarria, E. M. & Schroeder, C. M. Hydrodynamic trap for single particles and cells. *Appl. Phys. Lett.* **96,** 224101 (2010).

103. Curtis, M. D., Sheard, G. J. & Fouras, A. Feedback control system simulator for the control of biological cells in microfluidic cross slots and integrated microfluidic systems. *Lab Chip* **11,** 2343 (2011).

104. Tanyeri, M., Ranka, M., Sittipolkul, N. & Schroeder, C. M. A microfluidic-based hydrodynamic trap: design and implementation. *Lab Chip* **11,** 1786 (2011).

105. Hardt, S. & Schönfeld, F. Microfluidics: Fundamentals and Engineering Concepts. *Microfluid. Technol. Miniaturized Anal. Syst.* 1–58 (2007). doi:10.1007/978-0-387-68424-6_1

106. Sparreboom, W., van den Berg, A. & Eijkel, J. C. T. Transport in nanofluidic systems: a review of theory and applications. *New J Phys* **12,** 015004 (2010).

107. Ghosal, S. Fluid mechanics of electroosmotic flow and its effect on band broadening in capillary electrophoresis. *Electrophoresis* **25,** 214–228 (2004).

Bibliography

108. Behrens, S. H. & Grier, D. G. The charge of glass and silica surfaces. *J. Chem. Phys.* **115,** 6716–6721 (2001).

109. Wang, X., Cheng, C., Wang, S. & Liu, S. Electroosmotic pumps and their applications in microfluidic systems. *Microfluid. Nanofluidics* **6,** 145 (2009).

110. Fu, A. Y., Spence, C., Scherer, A., Arnold, F. H. & Quake, S. R. A microfabricated fluorescence-activated cell sorter. *Nat. Biotechnol.* **17,** 1109–1111 (1999).

111. Jones, T. B. Basic theory of dielectrophoresis and electrorotation. *IEEE Eng. Med. Biol. Mag.* **22,** 33–42 (2003).

112. Armani, M., Chaudhary, S., Probst, R. & Shapiro, B. Micro flow control particle tweezers. *Proc UTAS* 26–30 (2004).

113. Armani, M., Chaudhary, S., Probst, R. & Shapiro, B. Using feedback control and micro-fluidics to steer individual particles. *18th IEEE Int. Conf. Micro Electro Mech. Syst. 2005 MEMS 2005* (2005). doi:10.1109/memsys.2005.1454064

114. Armani, M. D., Chaudhary, S. V., Probst, R. & Shapiro, B. Using Feedback Control of Microflows to Independently Steer Multiple Particles. *J Microelectromech Syst* **15,** 945–956 (2006).

115. Ropp, C. *et al.* Nanoscale imaging and spontaneous emission control with a single nano-positioned quantum dot. *Nat. Commun.* **4,** 1447 (2013).

116. Probst, R., Cummins, Z., Ropp, C., Waks, E. & Shapiro, B. Flow Control of Small Objects on Chip: Manipulating Live Cells, Quantum Dots, and Nanowires. *IEEE Control Syst.* **32,** 26–53 (2012).

117. Ropp, C. *et al.* Manipulating Quantum Dots to Nanometer Precision by Control of Flow. *Nano Lett* **10,** 2525–2530 (2010).

118. Chaudhary, S. & Shapiro, B. Arbitrary steering of multiple particles independently in an electro-osmotically driven microfluidic system. *IEEE Trans. Control Syst. Technol.* **14,** 669–680 (2006).

119. Zhou, T., Liu, A.-L., He, F.-Y. & Xia, X.-H. Time-dependent starting profile of velocity upon application of external electrical potential in electroosmotic driven microchannels. *Colloids Surf. Physicochem. Eng. Asp.* **277,** 136–144 (2006).

120. Yan, D., Nguyen, N.-T., Yang, C. & Huang, X. Visualizing the transient electroosmotic flow and measuring the zeta potential of microchannels with a micro-PIV technique. *J. Chem. Phys.* **124,** 021103 (2006).

121. McDonald, J. C. *et al.* Fabrication of microfluidic systems in poly(dimethylsiloxane). *Electrophoresis* **21,** 27–40 (2000).

122. Park, J. W., Vahidi, B., Taylor, A. M., Rhee, S. W. & Jeon, N. L. Microfluidic culture platform for neuroscience research. *Nat. Protoc.* **1,** 2128–2136 (2006).

123. Tourovskaia, A., Figueroa-Masot, X. & Folch, A. Long-term microfluidic cultures of myotube microarrays for high-throughput focal stimulation. *Nat. Protoc.* **1,** 1092–1104 (2006).

124. Leclerc, E., Sakai, Y. & Fujii, T. Cell Culture in 3-Dimensional Microfluidic Structure of PDMS (polydimethylsiloxane). *Biomed. Microdevices* **5,** 109–114 (2003).

125. Walker, G. M., Ozers, M. S. & Beebe, D. J. Insect Cell Culture in Microfluidic Channels. *Biomed. Microdevices* **4,** 161–166 (2002).

126. Xia, Y. & Whitesides, G. M. Soft Lithography. *Annu. Rev. Mater. Sci.* **28,** 153–184 (1998).

127. Kalman, R. A New Approach to Linear Filtering and Prediction Problems. *Trans. ASME–Journal Basic Eng.* **82,** 35–45 (1960).

128. http://www.mathworks.com/matlabcentral/fileexchange/38302-kalman-filter-package.

129. Attaway, S. *Matlab: A Practical Introduction to Programming and Problem Solving*. (Butterworth-Heinemann, 2013).

Bibliography

130. Cass, S. & Diakopoulos, N. Top 10 Programming Languages. *IEEE Spectrum* (2014). at <http://spectrum.ieee.org/computing/software/top-10-programming-languages>

131. Chambers, A. F., Groom, A. C. & MacDonald, I. C. Metastasis: Dissemination and growth of cancer cells in metastatic sites. *Nat. Rev. Cancer* **2,** 563–572 (2002).

132. Li, G. *et al.* Accuracy of 3D volumetric image registration based on CT, MR and PET/CT phantom experiments. *J. Appl. Clin. Med. Phys.* **9,** (2008).

133. Naumov, G. N. *et al.* Ineffectiveness of Doxorubicin Treatment on Solitary Dormant Mammary Carcinoma Cells or Late-developing Metastases. *Breast Cancer Res. Treat.* **82,** 199–206 (2003).

134. Klein, C. A. *et al.* Genetic heterogeneity of single disseminated tumour cells in minimal residual cancer. *The Lancet* **360,** 683–689 (2002).

135. Riethdorf, S., Wikman, H. & Pantel, K. Review: Biological relevance of disseminated tumor cells in cancer patients. *Int. J. Cancer* **123,** 1991–2006 (2008).

136. Whipple, R. A. *et al.* Vimentin Filaments Support Extension of Tubulin-Based Microtentacles in Detached Breast Tumor Cells. *Cancer Res.* **68,** 5678–5688 (2008).

137. Balzer, E. M. *et al.* c-Src differentially regulates the functions of microtentacles and invadopodia. *Oncogene* **29,** 6402–6408 (2010).

138. Matrone, M. A. *et al.* Metastatic breast tumors express increased tau, which promotes microtentacle formation and the reattachment of detached breast tumor cells. *Oncogene* **29,** 3217–3227 (2010).

139. Matrone, M. A., Whipple, R. A., Balzer, E. M. & Martin, S. S. Microtentacles Tip the Balance of Cytoskeletal Forces in Circulating Tumor Cells. *Cancer Res.* **70,** 7737–7741 (2010).

140. Brangwynne, C. P. Microtubules can bear enhanced compressive loads in living cells because of lateral reinforcement. *J. Cell Biol.* **173,** 733–741 (2006).

141. Whipple, R. A., Cheung, A. M. & Martin, S. S. Detyrosinated microtubule protrusions in suspended mammary epithelial cells promote reattachment. *Exp. Cell Res.* **313,** 1326–1336 (2007).

142. Even-Ram, S. *et al.* Myosin IIA regulates cell motility and actomyosin–microtubule crosstalk. *Nat. Cell Biol.* **9,** 299–309 (2007).

143. Yoon, J. R. *et al.* Local anesthetics inhibit kinesin motility and microtentacle protrusions in human epithelial and breast tumor cells. *Breast Cancer Res. Treat.* **129,** 691–701 (2011).

144. Whipple, R. A. *et al.* Epithelial-to-Mesenchymal Transition Promotes Tubulin Detyrosination and Microtentacles that Enhance Endothelial Engagement. *Cancer Res.* **70,** 8127–8137 (2010).

145. Al-Mehdi, A. B. *et al.* Intravascular origin of metastasis from the proliferation of endothelium-attached tumor cells: a new model for metastasis. *Nat. Med.* **6,** 100–102 (2000).

146. Michler, P. *et al.* A Quantum Dot Single-Photon Turnstile Device. *Science* **290,** 2282–2285 (2000).

147. Han, M., Gao, X., Su, J. Z. & Nie, S. Quantum-dot-tagged microbeads for multiplexed optical coding of biomolecules. *Nat. Biotechnol.* **19,** 631–635 (2001).

148. Medintz, I. L., Uyeda, H. T., Goldman, E. R. & Mattoussi, H. Quantum dot bioconjugates for imaging, labelling and sensing. *Nat. Mater.* **4,** 435–446 (2005).

149. Chan, W. C. W. & Nie, S. Quantum Dot Bioconjugates for Ultrasensitive Nonisotopic Detection. *Science* **281,** 2016–2018 (1998).

150. Fafard, S. *et al.* Red-Emitting Semiconductor Quantum Dot Lasers. *Science* **274,** 1350–1353 (1996).

151. Kongkanand, A., Tvrdy, K., Takechi, K., Kuno, M. & Kamat, P. V. Quantum dot solar cells. Tuning photoresponse through size and shape control of CdSe-TiO2 architecture. *J. Am. Chem. Soc.* **130,** 4007–4015 (2008).

Bibliography

152. Barth, M., Kouba, J., Stingl, J., Löchel, B. & Benson, O. Modification of visible spontaneous emission with silicon nitride photonic crystal nanocavities. *Opt. Express* **15,** 17231 (2007).

153. Ramos, A., Morgan, H., Green, N. G. & Castellanos, A. Ac electrokinetics: a review of forces in microelectrode structures. *J Phys Appl Phys* **31,** 2338–2353 (1998).

154. Ropp, C. *et al.* Positioning and Immobilization of Individual Quantum Dots with Nanoscale Precision. *Nano Lett* **10,** 4673–4679 (2010).

155. Thompson, R. E., Larson, D. R. & Webb, W. W. Precise nanometer localization analysis for individual fluorescent probes. *Biophys. J.* **82,** 2775–2783 (2002).

156. Cui, Y. Functional Nanoscale Electronic Devices Assembled Using Silicon Nanowire Building Blocks. *Science* **291,** 851–853 (2001).

157. Engheta, N. Circuits with Light at Nanoscales: Optical Nanocircuits Inspired by Metamaterials. *Science* **317,** 1698–1702 (2007).

158. Wei, H. *et al.* Quantum Dot-Based Local Field Imaging Reveals Plasmon-Based Interferometric Logic in Silver Nanowire Networks. *Nano Lett.* **11,** 471–475 (2011).

159. Anker, J. N. *et al.* Biosensing with plasmonic nanosensors. *Nat. Mater.* **7,** 442–453 (2008).

160. Fan, J. A. *et al.* Self-Assembled Plasmonic Nanoparticle Clusters. *Science* **328,** 1135–1138 (2010).

161. Chang, D. E., Sørensen, A. S., Demler, E. A. & Lukin, M. D. A single-photon transistor using nanoscale surface plasmons. *Nat. Phys.* **3,** 807–812 (2007).

162. Dickson, R. M. & Lyon, L. A. Unidirectional Plasmon Propagation in Metallic Nanowires. *J. Phys. Chem. B* **104,** 6095–6098 (2000).

163. Akimov, A. V. *et al.* Generation of single optical plasmons in metallic nanowires coupled to quantum dots. *Nature* **450,** 402–406 (2007).

164. Knight, M. W. *et al.* Nanoparticle-Mediated Coupling of Light into a Nanowire. *Nano Lett.* **7,** 2346–2350 (2007).

165. Lee, S. Y. *et al.* Dispersion in the SERS Enhancement with Silver Nanocube Dimers. *ACS Nano* **4,** 5763–5772 (2010).

166. Jauffred, L., Richardson, A. C. & Oddershede, L. B. Three-Dimensional Optical Control of Individual Quantum Dots. *Nano Lett.* **8,** 3376–3380 (2008).

167. Yu, T., Cheong, F.-C. & Sow, C.-H. The manipulation and assembly of CuO nanorods with line optical tweezers. *Nanotechnology* **15,** 1732 (2004).

168. Dawood, F., Qin, S., Li, L., Lin, E. Y. & Fourkas, J. T. Simultaneous microscale optical manipulation, fabrication and immobilisation in aqueous media. *Chem. Sci.* **3,** 2449–2456 (2012).

169. Benson, O. Assembly of hybrid photonic architectures from nanophotonic constituents. *Nature* **480,** 193–199 (2011).

170. Sitti, M. & Hashimoto, H. Controlled pushing of nanoparticles: modeling and experiments. *IEEEASME Trans. Mechatron.* **5,** 199–211 (2000).

171. Chey, S. J., Huang, L. & Weaver, J. H. Manipulation and writing with Ag nanocrystals on Si(111)-7×7. *Appl. Phys. Lett.* **72,** 2698 (1998).

172. Cohen, A. E. & Moerner, W. E. Suppressing Brownian motion of individual biomolecules in solution. *Proc. Natl. Acad. Sci. U. S. A.* **103,** 4362–4365 (2006).

173. Mathai, P. P., Carmichael, P. T., Shapiro, B. A. & Liddle, J. A. Simultaneous positioning and orientation of single nano-wires using flow control. *RSC Adv* **3,** 2677 (2013).

174. Kumar, R. & Raghavan, S. R. Thermothickening in Solutions of Telechelic Associating Polymers and Cyclodextrins. *Langmuir* **26,** 56–62 (2010).

Bibliography

175. Kumar, R., Kalur, G. C., Ziserman, L., Danino, D. & Raghavan, S. R. Wormlike Micelles of a C22-Tailed Zwitterionic Betaine Surfactant: From Viscoelastic Solutions to Elastic Gels. *Langmuir* **23,** 12849–12856 (2007).

176. Kojima, K., Ito, M., Morishita, H. & Hayashi, N. A Novel Water-Soluble Photoinitiator for the Acrylic Photopolymerization Type Resist System. *Chem. Mater.* **10,** 3429–3433 (1998).

177. Sun, Y., Yin, Y., Mayers, B. T., Herricks, T. & Xia, Y. Uniform Silver Nanowires Synthesis by Reducing AgNO $_3$ with Ethylene Glycol in the Presence of Seeds and Poly(Vinyl Pyrrolidone). *Chem. Mater.* **14,** 4736–4745 (2002).

178. Friese, M. E. J., Nieminen, T. A., Heckenberg, N. R. & Rubinsztein-Dunlop, H. Optical alignment and spinning of laser-trapped microscopic particles. *Nature* **394,** 348–350 (1998).

179. Sacconi, L. *et al.* Three-dimensional magneto-optic trap for micro-object manipulation. *Opt. Lett.* **26,** 1359–1361 (2001).

180. Ditlbacher, H. *et al.* Silver Nanowires as Surface Plasmon Resonators. *Phys. Rev. Lett.* **95,** (2005).

181. Chang, D. E., Sørensen, A. S., Hemmer, P. R. & Lukin, M. D. Quantum Optics with Surface Plasmons. *Phys. Rev. Lett.* **97,** (2006).

182. Anger, P., Bharadwaj, P. & Novotny, L. Enhancement and Quenching of Single-Molecule Fluorescence. *Phys. Rev. Lett.* **96,** (2006).

183. Curto, A. G. *et al.* Unidirectional Emission of a Quantum Dot Coupled to a Nanoantenna. *Science* **329,** 930–933 (2010).

184. Nahata, A., Linke, R. A., Ishi, T. & Ohashi, K. Enhanced nonlinear optical conversion from a periodically nanostructured metal film. *Opt. Lett.* **28,** 423 (2003).

185. Kim, S. *et al.* High-harmonic generation by resonant plasmon field enhancement. *Nature* **453,** 757–760 (2008).

186. Nie, S. Probing Single Molecules and Single Nanoparticles by Surface-Enhanced Raman Scattering. *Science* **275,** 1102–1106 (1997).

187. Haes, A. J. & Van Duyne, R. P. A Nanoscale Optical Biosensor: Sensitivity and Selectivity of an Approach Based on the Localized Surface Plasmon Resonance Spectroscopy of Triangular Silver Nanoparticles. *J. Am. Chem. Soc.* **124,** 10596–10604 (2002).

188. Drezet, A., Cuche, A. & Huant, S. Near-field microscopy with a single-photon point-like emitter: Resolution versus the aperture tip? *Opt. Commun.* **284,** 1444–1450 (2011).

189. Bozhevolnyi, S. I. & Vohnsen, B. Near-field optics with uncoated fiber tips: light confinement and spatial resolution. *J. Opt. Soc. Am. B* **14,** 1656 (1997).

190. Hecht, B. *et al.* Scanning near-field optical microscopy with aperture probes: Fundamentals and applications. *J. Chem. Phys.* **112,** 7761 (2000).

191. Inouye, Y. & Kawata, S. Near-field scanning optical microscope with a metallic probe tip. *Opt. Lett.* **19,** 159 (1994).

192. Zenhausern, F., O'Boyle, M. P. & Wickramasinghe, H. K. Apertureless near-field optical microscope. *Appl. Phys. Lett.* **65,** 1623 (1994).

193. Dorfmüller, J. *et al.* Fabry-Pérot Resonances in One-Dimensional Plasmonic Nanostructures. *Nano Lett.* **9,** 2372–2377 (2009).

194. Schnell, M., Garcia-Etxarri, A., Alkorta, J., Aizpurua, J. & Hillenbrand, R. Phase-Resolved Mapping of the Near-Field Vector and Polarization State in Nanoscale Antenna Gaps. *Nano Lett.* **10,** 3524–3528 (2010).

195. Imura, K. & Okamoto, H. Reciprocity in scanning near-field optical microscopy: illumination and collection modes of transmission measurements. *Opt. Lett.* **31,** 1474 (2006).

196. Yao, H., Li, Z. & Gong, Q. Coupling-induced excitation of a forbidden surface plasmon mode of a gold nanorod. *Sci. China Ser. G Phys. Mech. Astron.* **52,** 1129–1138 (2009).

197. Nelayah, J. *et al.* Mapping surface plasmons on a single metallic nanoparticle. *Nat. Phys.* **3,** 348–353 (2007).

198. Vesseur, E. J. R., de Waele, R., Kuttge, M. & Polman, A. Direct Observation of Plasmonic Modes in Au Nanowires Using High-Resolution Cathodoluminescence Spectroscopy. *Nano Lett.* **7,** 2843–2846 (2007).

199. Frimmer, M., Coenen, T. & Koenderink, A. F. Signature of a Fano Resonance in a Plasmonic Metamolecule's Local Density of Optical States. *Phys. Rev. Lett.* **108,** (2012).

200. Frimmer, M., Chen, Y. & Koenderink, A. F. Scanning Emitter Lifetime Imaging Microscopy for Spontaneous Emission Control. *Phys. Rev. Lett.* **107,** (2011).

201. Michaelis, null, Hettich, null, Mlynek, null & Sandoghdar, null. Optical microscopy using a single-molecule light source. *Nature* **405,** 325–328 (2000).

202. Cuche, A. *et al.* Near-field optical microscopy with a nanodiamond-based single-photon tip. *Opt. Express* **17,** 19969 (2009).

203. Shubeita, G. T. *et al.* Scanning near-field optical microscopy using semiconductor nanocrystals as a local fluorescence and fluorescence resonance energy transfer source. *J. Microsc.* **210,** 274–278 (2003).

204. Huck, A., Kumar, S., Shakoor, A. & Andersen, U. L. Controlled Coupling of a Single Nitrogen-Vacancy Center to a Silver Nanowire. *Phys. Rev. Lett.* **106,** (2011).

205. Schell, A. W. *et al.* Single defect centers in diamond nanocrystals as quantum probes for plasmonic nanostructures. *Opt. Express* **19,** 7914 (2011).

206. Geiselmann, M. *et al.* Three-dimensional optical manipulation of a single electron spin. *Nat. Nanotechnol.* **8,** 175–179 (2013).

207. Cang, H. *et al.* Probing the electromagnetic field of a 15-nanometre hotspot by single molecule imaging. *Nature* **469,** 385–388 (2011).

208. Bruchez Jr., M. Semiconductor Nanocrystals as Fluorescent Biological Labels. *Science* **281,** 2013–2016 (1998).

209. Brokmann, X. *et al.* Colloidal CdSe/ZnS quantum dots as single-photon sources. *New J. Phys.* **6,** 99–99 (2004).

210. Sonnefraud, Y. *et al.* Near-field optical imaging with a CdSe single nanocrystal-based active tip. *Opt. Express* **14,** 10596 (2006).

211. Farahani, J. N., Pohl, D. W., Eisler, H.-J. & Hecht, B. Single Quantum Dot Coupled to a Scanning Optical Antenna: A Tunable Superemitter. *Phys. Rev. Lett.* **95,** (2005).

212. Hohenester, U. & Trugler, A. Interaction of Single Molecules With Metallic Nanoparticles. *IEEE J. Sel. Top. Quantum Electron.* **14,** 1430–1440 (2008).

213. Empedocles, S. A., Neuhauser, R. & Bawendi, M. G. Three-dimensional orientation measurements of symmetric single chromophores using polarization microscopy. *Nature* **399,** 126–130 (1999).

214. Chicanne, C. *et al.* Imaging the Local Density of States of Optical Corrals. *Phys. Rev. Lett.* **88,** (2002).

215. Shimizu, K. *et al.* Blinking statistics in single semiconductor nanocrystal quantum dots. *Phys. Rev. B* **63,** (2001).

216. Balanis, C. A. *Advanced engineering electromagnetics*. (John Wiley & Sons, 2012).

217. Gia-Wei Shu *et al.* Photoluminescence of colloidal CdSe/ZnS quantum dots under oxygen atmosphere. *IEEE Trans. Nanotechnol.* **4,** 632–636 (2005).

Bibliography

218. van Sark, W. G. J. H. M. *et al.* Photooxidation and Photobleaching of Single CdSe/ZnS Quantum Dots Probed by Room-Temperature Time-Resolved Spectroscopy. *J. Phys. Chem. B* **105,** 8281–8284 (2001).

219. van Sark, W. G. J. H. M., Frederix, P. L. T. M., Bol, A. A., Gerritsen, H. C. & Meijerink, A. Blueing, Bleaching, and Blinking of Single CdSe/ZnS Quantum Dots. *ChemPhysChem* **3,** 871–879 (2002).

220. Milonni, P. W. *Lasers*. (Wiley, 1988).

221. Kurtsiefer, C., Mayer, S., Zarda, P. & Weinfurter, H. Stable Solid-State Source of Single Photons. *Phys. Rev. Lett.* **85,** 290–293 (2000).

222. Early, K. T., Sudeep, P. K., Emrick, T. & Barnes, M. D. Polarization-Driven Stark Shifts in Quantum Dot Luminescence from Single CdSe/oligo-PPV Nanoparticles. *Nano Lett.* **10,** 1754–1758 (2010).

223. Cohen, A. E. Control of Nanoparticles with Arbitrary Two-Dimensional Force Fields. *Phys. Rev. Lett.* **94,** 118102 (2005).

224. Barz, D. P. J. & Ehrhard, P. Model and verification of electrokinetic flow and transport in a micro-electrophoresis device. *Lab. Chip* **5,** 949–958 (2005).

225. Santiago, J. G. Electroosmotic Flows in Microchannels with Finite Inertial and Pressure Forces. *Anal. Chem.* **73,** 2353–2365 (2001).

226. Laser, D. J. & Santiago, J. G. A review of micropumps. *J Micromech Microeng* **14,** R35–R64 (2004).

227. Rosensweig, R. E. *Ferrohydrodynamics*. (Courier Dover Publications, 1997).

228. Mathai, P. P., Berglund, A. J., Alexander Liddle, J. & Shapiro, B. A. Simultaneous positioning and orientation of a single nano-object by flow control: theory and simulations. *New J Phys* **13,** 013027 (2011).

229. King, J. Microfluidic Device for the Electrokinetic Manipulation of Single Molecules. *Masters Theses* (2009). at <http://trace.tennessee.edu/utk_gradthes/41>

230. Davis, L. *et al.* Maximum-likelihood position sensing and actively controlled electrokinetic transport for single-molecule trapping. in **6862,** 68620P–68620P–10 (2008).

231. Probst, R. & Shapiro, B. Three-dimensional electrokinetic tweezing: device design, modeling, and control algorithms. *J. Micromechanics Microengineering* **21,** 027004 (2011).

232. Willert, C. E. & Gharib, M. Three-dimensional particle imaging with a single camera. *Exp. Fluids* **12,** 353–358 (1992).

233. Gharib, M., Pereira, F., Dabiri, D., Hove, J. R. & Modarress, D. Quantitative Flow Visualization: Toward a Comprehensive Flow Diagnostic Tool. *Integr. Comp. Biol.* **42,** 964–970 (2002).

234. Kajitani, L. & Dabiri, D. A full three-dimensional characterization of defocusing digital particle image velocimetry. *Meas. Sci. Technol.* **16,** 790 (2005).

235. Yoon, S. Y. & Kim, K. C. 3D particle position and 3D velocity field measurement in a microvolume via the defocusing concept. *Meas. Sci. Technol.* **17,** 2897 (2006).

236. Ropp, C. *et al.* Fabrication of nanoassemblies using flow control. *Nano Lett.* **13,** 3936–3941 (2013).